Design and Modeling of Carbon Nanotube-Based Compliant Mechanisms

by

Christopher M. DiBiasio

Sc.B., Mechanical Engineering (2005)

Massachusetts Institute of Technology

Submitted to the Department of Mechanical Engineering
in Partial Fulfillment of the Requirements for the Degree of
Master of Science in Mechanical Engineering

at the

Massachusetts Institute of Technology

February 2007

Signature of Author……
Department of Mechanical Engineering
January 16, 2007

Certified by……
Martin L. Culpepper
Rockwell International Associate Professor of Mechanical Engineering
Thesis Supervisor

Accepted by……..……
Lallit Anand
Professor of Mechanical Engineering
Graduate Officer

Design and Modeling of Carbon Nanotube-Based
Compliant Mechanisms

by

Christopher M. DiBiasio

Submitted to the Department of Mechanical Engineering
on January 16, 2007 in Partial Fulfillment of the
Requirements for the Degree of Master of Science in
Mechanical Engineering

ABSTRACT

The objective of this research is to generate the knowledge required to adapt macro- and micro-scale compliant mechanism theory to design carbon nanotube-based nano-scale compliant mechanisms. Molecular simulations of a nano-scale parallel guiding mechanism uncovered three regions of behavior. Region I is governed by the bulk deformation of the carbon nanotubes. Region II is characterized by hinge–like flexing of four "kinks" that occur due to buckling of the carbon nanotube walls. Region III, an intermediate region, exhibits direction dependant behavior. We report on the ability of a conventional compliant mechanism modeling approach, the pseudo–rigid–body model, to predict the region I behavior of a nano-scale parallel guiding mechanism that uses single–walled (5,5) carbon nanotubes as the flexural elements. Van der Waals forces were found to affect the kinematic and elastomechanic behavior of the nano-scale parallel guiding mechanism. A modified value of the pseudo–rigid–body model stiffness coefficient is presented to capture the affect of van der Waals interactions within (5,5) nanotubes during region I operation. Molecular simulation of region I behaviors match the modified pseudo–rigid–body model predictions of (1) kinematic behavior with less than 7.3 % error and (2) elastomechanic behavior with less than 8 % error. Although region I is of the most interest because of its well-defined and stable nature, region II motion is also investigated to provide a basis for establishing future work in this region.

Thesis Supervisor: Martin L. Culpepper
Title: Rockwell International Associate Professor of Mechanical Engineering

ACKNOWLEDGEMENTS

I would like to thank my thesis advisor Martin Culpepper for the guidance he provided me as I conducted the research that would eventually lead to this thesis. He has provided me with advice that has not only made me more adept at research and engineering, but has also helped me to develop professionally. I look forward to continue working with him and learning from him as I pursue my doctorate.

I would also like to thank my colleagues in the Precision Compliant Systems Laboratory. Their advice on conducting research and the stresses of graduate life has helped me maintain balance in my life as a graduate student. I would especially like to thank Amos Winter and Robert Panas for their contributions in creating the initial models used in the simulations that were included in this thesis.

I also need to thank my family and friends for all of their support over the last year and a half. Without the emotional support they have given me, I do not know if it would have been possible to have completed this work. I also need to thank my mother and father who, after supporting me through my undergraduate program, continue to provide me financial and emotional support. The successes I have achieved in my life I owe in large part to them.

Finally, I must thank those who financially supported my graduate research. I would first like to thank former MIT President Charles Vest and his wife Rebecca for providing me with a fellowship during my first year in graduate school. Having a fellowship enabled me to define a research path that I was genuinely interested in, not just a project that was financially supported. Lastly, I would like to thank Rockwell International and the Karl Chang Innovation Fund at MIT for supporting the last six months of my research.

Table of Contents

List of Figures

List of Tables

Chapter 1

Introduction

The objective of this research is to generate the knowledge required to adapt macro- and micro-scale compliant mechanism theory to design carbon nanotube-based nano-scale compliant mechanisms. Compliant mechanisms are systems of rigid and flexible elements that use the bending deformation of the compliant members to guide smooth and continuous motion of rigid components [1]. Carbon nanotube-based nano-scale compliant mechanisms are important because they may provide the means to produce nano-scale devices while avoiding (1) the size limitations imposed by current nano-fabrication techniques and (2) the mechanical property limitations that are possessed by nano-scale materials. The realization of carbon nanotube-based compliant mechanisms would allow scientists and engineers to design smaller (100 times smaller than current micro-scale devices) and faster (over 1000 times faster than current micro-scale devices) compliant mechanisms for devices. The design and fabrication of compliant mechanisms at the macro- and micro-scale have been practiced for decades, however, the incorporation of the most rudimentary flexures within nano-scale mechanical systems is a recent development [2]. There are two major roadblocks to using macro- and micro-scale compliant mechanism research at the nano-scale: 1) material limitations and 2) fabrication limitations. Conventional nano-scale fabrication methods are compatible with a limited set of materials. The mechanical properties of these materials impose a limit on the elastic deflections of nano-scale flexures that is approximately 20% of the flexure's characteristic length. Conventional nano-fabrication process capabilities limit the size and accuracy of features on the order of a few tens of nanometers, and this level of uncertainty would mean that a match between model and measured performance could only be obtained using parts measuring hundreds of nanometers. In light of these limitations a new approach for engineering nano-scale flexure-based devices will be needed.

Carbon nanotubes are single molecules that possess high strength (failure stress ~100 GPa [3]) and large failure strains (~40% [4]) in comparison to conventional engineering materials. These properties make them attractive for use in nano-scale compliant mechanisms. The majority of current research has focused on characterizing, understanding, and modeling the physical properties of carbon nanotubes. Little work has been done understand how to incorporate carbon nanotubes into simple nano-scale mechanical elements that are deterministically engineered to meet a set of design specifications. As a result, no one has determined if/how conventional compliant mechanism theory may be adapted so that carbon nanotube-based nano-scale compliant mechanisms may engineered. These devices could be driven at speeds 1000 times faster than their micro-scale counterparts. This is because the natural frequency of a device scales with the inverse of the square-root of its mass. It is clear that the behavior of a carbon nanotube-based compliant mechanism will need to be investigated and subsequently modeled before design synthesis and fabrication research becomes feasible.

1.1 Importance

Over the last twenty years, research has been conducted to move macro-scale devices and technologies to the micro-scale. Micro-electro-mechanical systems (MEMS) are now used in consumer products ranging from automobiles (airbag accelerometers) to cellular phones (microphones), and even home theater systems (micro-mirrors in digital light processing (DLP®) televisions). For scientists and engineers, the introduction of MEMS technology into fields such as communications (fiber optics positioning) has allowed for the development of state-of-the-art systems that perform tasks that were impractical or impossible at the macro-scale. As engineers have started to master the art of MEMS design and fabrication, their focus has shifted towards the next level: nanometer-level devices.

1.1.1 Need for Nano-scale Devices

While the benefits of making electronic components smaller is clear (less power consumption and higher computation density), the role of nano-electro-mechanical systems (NEMS) is not well-defined. In order to understand the need for NEMS it is important to look at the benefits of miniaturizing a mechanical system:

1. **High Speed:** The natural frequency of a device scales with the inverse of the square root of the system mass. This smaller mass, therefore, leads to less inertial forces which corresponds to higher system natural frequencies. This allows the device to be driven at faster device driving frequencies. For instance, a 10x10x10 nm^3 mass may be driven 1000 times faster than a 1 μm^3 mass of the same material, assuming each mass is attached to a spring of similar stiffness.
2. **Scale Matching:** It is difficult to manipulate objects on the nano-scale using MEMS devices as the system scales are mismatched, typically over three orders of magnitude difference. When system components are the same order of magnitude in size as the item to be manipulated, it is in general easier to accomplish those tasks. When scale mismatches occur in a system a de-amplification or amplification mechanism must be introduced. In order to attenuate a displacement input a compliant member must be introduced in the load path. Since the system natural frequency scales with the square root of the load path stiffness, adding a compliant spring in series with the applied load has an adverse affect on the system stiffness.
3. **Smaller Footprint:** A smaller device footprint leads to device integration in systems where space and/or weight is a premium. This smaller size will drive innovation in many different areas such as sensors, actuators, and manipulators.

While the preceding list is not all-inclusive, it is important to keep these benefits in mind when evaluating the need for NEMS devices. The remainder of this section will discuss each of the preceding benefits in more detail.

The enhancement of system speed is perhaps the most important benefit of operating at the nano-scale. Many nano-scale probing and imaging technologies are fundamentally limited in their operational speed due to the natural frequencies of their components. A good candidate for

the introduction of a NEMS based module would be, for instance, an atomic force microscope (AFM). Figure 1.1 depicts the basic operating principles of an AFM in the "tapping" mode.

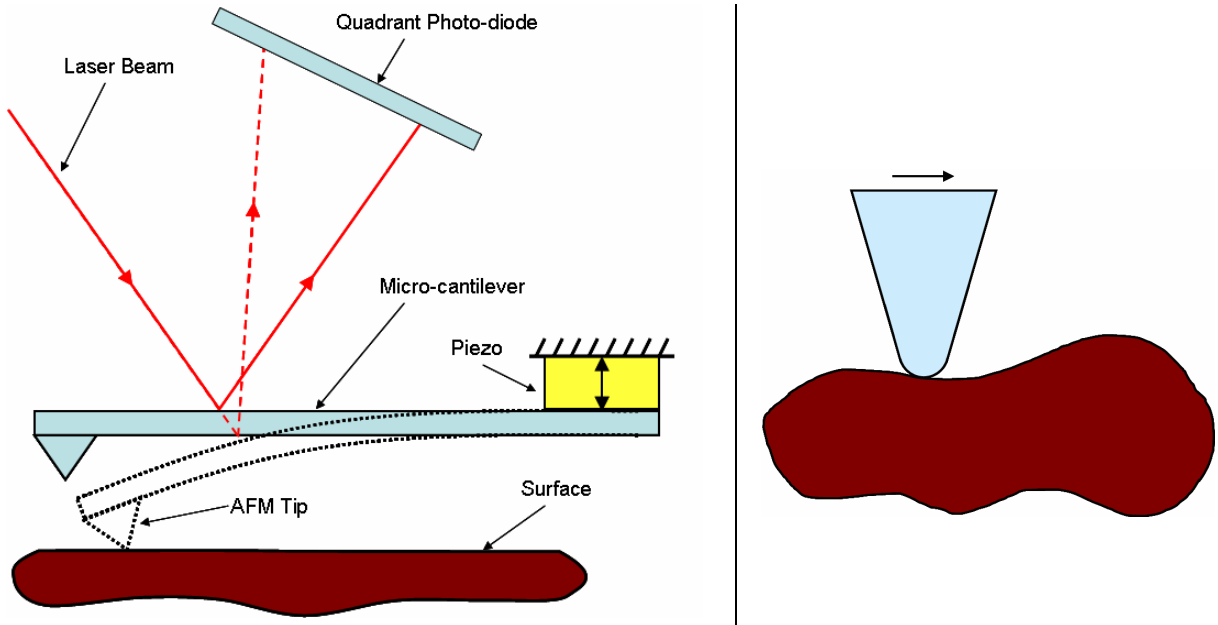

Figure 1.1: Schematic of AFM operation (a) and a close-up of an AFM tip on substrate (b).

During operation, a laser beam aimed at the back of a silicon cantilever reflects onto a quadrant photo-detector, and the deflection of the laser on the photo-detector allows for measurement of the surface height. By raster scanning the surface in a pixel-by-pixel fashion, a surface profile may be generated for the sample, as shown in Fig 1.1(b). CNT-based mechanisms could replace micro-scale cantilevers and enable increased speeds that could for instance make video rate AFM's possible.

Another advantage of nano-scale devices is that they minimize the scale mismatch problem inherent when using macro- and micro-scale devices to perform nano-scale tasks. De-amplification is necessary for most micro- or macro-scale actuators because their displacement and force outputs are at least three orders of magnitude larger than the intended nano-scale output. The most common method of attenuating force and displacement outputs from an actuator is to use a flexure, as will be discussed in section 1.1.2. In order to attenuate an actuator displacement input, the flexure must be extremely compliant. This means the effective spring constant for the compliant member is small. This de-amplification may achieve the static needs of the system, but the system dynamics are adversely impacted as a result. Since system natural frequency scales with the square root of the system's effective spring constant, adding a

compliant flexure lowers the overall system natural frequency. This increases the system's sensitivity to low frequency vibrations that are commonly present in the environment surrounding the system. These low frequency vibrations may easily introduce nanometers to microns worth of displacement into the system, which could greatly reduce the performance of the system. These inherent problems of scale mismatch could be averted by using nano-scale devices to perform nano-scale tasks.

Nano-scale devices could have a large impact in the fields of biology, chemistry, physics, and nano-fluidics. A nano-scale device capable of grasping individual molecules could allow mechanical manipulation of proteins, giving biologists and chemists new tools for studying and synthesizing proteins [5]. The ability to grasp individual DNA strands and "cut" them would allow for advanced faster genomic sequencing, which could lead to greater advances in genetic testing and therapy [5, 6]. Also, a nano-scale device could be used to probe individual organelles in cells, allowing biologists to be able to more quickly understand and model cell function as well as create new cell therapies [7]. Using a nano-scale manipulator, physicists would also be able to manipulate quantum dots more easily and effectively, allowing for rapid advances in fields such as quantum computing [8]. Engineers working in the field of nano-fluidics have promised compact biological and chemical sensors, "lab-on-a-chip" products, and even artificial cells and organelles [9]. In order to build these fluidic systems, however, there needs to be a nano-scale equivalent of a fluid pump and a binary on/off valve [10].

It is also important to realize the impact of the small nano-scale device footprint on information density. NEMS based transistors, relays, and nonvolatile memories have the ability to contribute to the electronics industry [11]. They would allow smaller chips that consume less power and have more computational capacity to be produced, which would greatly impact the role of computing in everyday life. Communications would also see an impact from nano-scale devices by way of denser fiber optic interconnects. Nano-scale devices could serve as optic alignment stages as well as mirror positioning stages.

1.1.2 Role of Compliant Mechanisms in Nano-electro-mechanical Systems

It is important to examine how MEMS devices are constructed when discussing how a NEMS device might be embodied. Most MEMS devices consist of 1) an actuator, 2) bearings, 3) moving member, 4) a support structure, and 5) a metrology system. Research has been

conducted on the design and fabrication of actuators and metrology systems for nano-scale applications, but little work has been done on miniaturizing the necessary bearings and support structure. This is unfortunate, as the preferred embodiment of bearings at the MEMS level are flexures, and little is known about how they will be embodied or how they will perform at the nanometer level.

Compliant mechanisms (CM) are mechanical devices in which one or more components are deformed elastically in order to guide motion. Figure 1.2 shows a compliant parallel-guiding mechanism, which consists of a rigid coupler and grounding bar as well as two compliant members, in an undeformed (shaded) and deformed state.

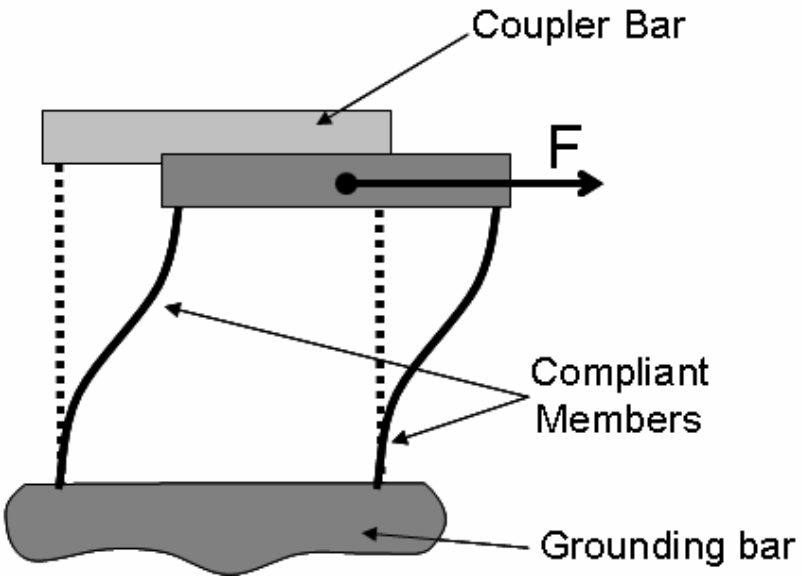

Figure 1.2: A compliant parallel-guiding mechanism.

The advantages of using a CM as the support structure and bearing for the coupler bar are that CMs 1) do not require assembly, 2) experience little subject to hysteresis due to friction during operation, 3) are subject to little energy dissipation during operation, 4) are inherently deterministic in nature, and 5) may be cycled many times without performance loss provided the loading level produces stresses less than the critical failure stress of the material.

As will be discussed in section 1.1.3, most nanofabrication processes are 2½ dimensional processes. As a result, most MEMS devices consist of planar features whose thickness is defined by the silicon device layer thickness. Figure 1.3 shows a picture of a six axis positioning stage by Chen and Culpepper [12].

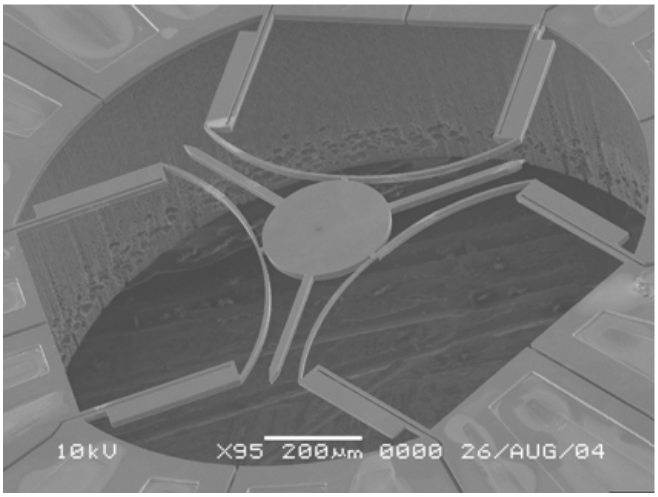

Figure 1.3: A micro-scale six-axis compliant positioning stage by Chen and Culpepper[1].

It consists of a central positioning stage connected to flexure beams which are further connected to thermal actuators. The manipulator has a 10 µm maximum range. The topology formed by the CM based device conforms to the requirements of 2½ dimensional fabrication, as the entire device consists of a planar geometry. Using CMs in MEMS devices eliminates the need for micro-scale assembly, which is difficult due to the scales of the parts involved in the assembly. As part sizes become sub-micron in size, forces due to surface tension and electrostatic interaction make small part alignment and manipulation nearly impossible. Using a standard scaling law for CMs, the ratio of elastic modulus to yield strength of the material [3,13], a carbon nanotube based six-axis positioner would have almost three times the range of the positioner made by Chen and Culpepper [12].

Perhaps the most important benefit in using CMs for bearings and the support structure in MEMS devices is the deterministic nature of the flexural components. Deterministic devices have a single output for any input, and furthermore, these outputs are usually easily mapped. As flexures do not experience significant friction, stiction, or slip during their operation, three problems inherent in motion guidance components held together by pin joints or bolts, this removes a source of hysteresis from the system. Furthermore, the primary mode of energy storage during the deflection of the flexure is through the stretching of atomic bonds. As such, there is little energy loss while cycling a flexure blade under load. A CMs deterministic nature is not affected by manufacturing error as an improperly manufactured flexure will still give one

[1] Figure 1.3 reproduced with permission from Professor Martin Culpepper.

output for a single input. The change in stiffness resulting from manufacturing error will require that the CM be calibrated.

1.1.3 Fabrication Challenges at the Nanometer Level

Ideally one would like to take the knowledge gained from MEMS research and apply design and fabrication rules to a NEMS device. Unfortunately the predominant method of MEMS fabrication, projection lithography [14], is not an option in the fabrication of a nano-scale device. The diffraction limit of lithography sets the resolution for fabricated geometries. Equation 1.1 shows the relationship of minimum feature size, w_{min}, to the radiation wavelength, λ, and numerical aperture, NA [14].

$$w_{min} = \frac{1}{2}\left(\frac{\lambda}{2NA}\right) \tag{1.1}$$

Currently the state-of-the-art in projection lithography is an ArF laser with a wavelength of 193 nm and a lens system utilizing immersion lithography with a numerical aperture of 0.9. Accordingly, the minimum feature size under ideal conditions is approximately 50 nm, a far cry from the nanometers of resolution desired for nano-scale CMs. The next semiconductor industry target for projection lithography is the 32 nm node, and it is unknown at this time whether or not projection lithography will meet the resolution demands for this next node. Development of radiation sources with finer wavelengths is ongoing, but progress has been slow. Advances in immersion lithography have made slight improvements in system numerical aperture, but not enough to produces a useful impact on minimum feature resolution. If nano-scale devices are to be built with flexural components, an alternative fabrication method is needed.

Electron-beam lithography (EBL) [14] could prove to be a viable alternative fabrication method for nano-scale features. The advantage of EBL is that device features of 5-10 nm are possible. However, because of the pixel-by-pixel nature of the process, writing times for an exposure are slow. To expose 50% of 4 nm^2 pixels requiring 100 electrons of exposure in a 1 cm^2 area, even the best EBL machines would take approximately three days to complete the pattern. If nano-scale devices are to be produced massively in parallel, another fabrication technique will need to be utilized.

Nano-imprint lithography (also referred to as soft lithography) [15] is another alternative for fabrication at the nano-scale. Hua et al have shown that polymer molds replicating carbon nanotubes with diameters on the order of a few nanometers can create features in silicon with

nanometer resolution [16]. Unfortunately, soft lithography is mainly used as a method of replicating an existing feature. This makes it impractical for fabrication of nano-scale compliant mechanisms.

1.1.4 Performance Limitations Due to Material Properties

Even if a fabrication method existed that could create nanometer features, there are performance limitations that stem from the physical properties of the principal material used in MEMS devices, bulk silicon. The most relevant bulk mechanical properties for CM design are presented in Table 1.1 for single crystal silicon [13]. For a silicon cantilever beam 10 μm thick, 50 μm wide, and 100 μm long, failure in the beam would occur at 3.68 μm axial extension or 24.5 μm lateral tip deflection. Since silicon is a brittle material and does not plastically deform, it is common practice to introduce a safety factor in practical device designs in order to avoid possible beam fracture. This safety factor decreases the total elastic beam bending deflection in the flexure.

Table 1.1: Bulk mechanical properties of silicon.

Elastic Modulus	190 GPa
Failure Strength	7 GPa
Density	2300 kg/m^3

1.1.5 Carbon Nanotubes as a Nano-scale Flexure Material

Carbon nanotubes (CNTs) were first discovered by Iijima in 1991 [3]. They are single molecules of carbon that take the form of tubes with diameters on the order of nanometers. Due to their exceptional mechanical properties, CNTs show promise to be a useful material to incorporate into NEMS devices . It has been shown that CNTs may undergo elastic strain in excess of 40% [4], which is larger than any materials currently used in MEMS devices. Furthermore, CNTs are grown from catalyst particles whose size roughly dictates the diameter of the CNT, which means that fine feature sizes may be attained without the use of lithography. If CNTs could be incorporated as the flexural components of nano-scale compliant mechanisms (nCMs), it may be possible to realize nano-scale devices with greater range and smaller feature sizes than their silicon counterparts.

1.2 Overview of Prior Art

The majority of research has been conducted via simulation, and the majority of physical prototypes that have been produced are one degree-of-freedom mechanisms with simple topologies and functions. Almost all of the realized devices operate in the CNT small-deformation regime while the majority of the simulation work has been carried out on the more complicated large-deformation devices and designs that exploit the relative sliding and rotation of multi-walled CNTs.

1.2.1 Small-Deformation Devices

The first class of CNT-based mechanisms rely on the stretching of atomic bonds in torsion as well as bending to produce small one degree-of-freedom motion, i.e. deflections less than 10% of the flexure's characteristic length. In one of the first demonstrations of using CNTs as a compliant mechanical element, nano-scale tweezers have been demonstrated as an effective means of grasping and manipulating nano-scale particles [17-19]. Figure 1.4(a) shows the profile of the tweezers, which consist of a split electrode with CNT bundles attached at the tip.

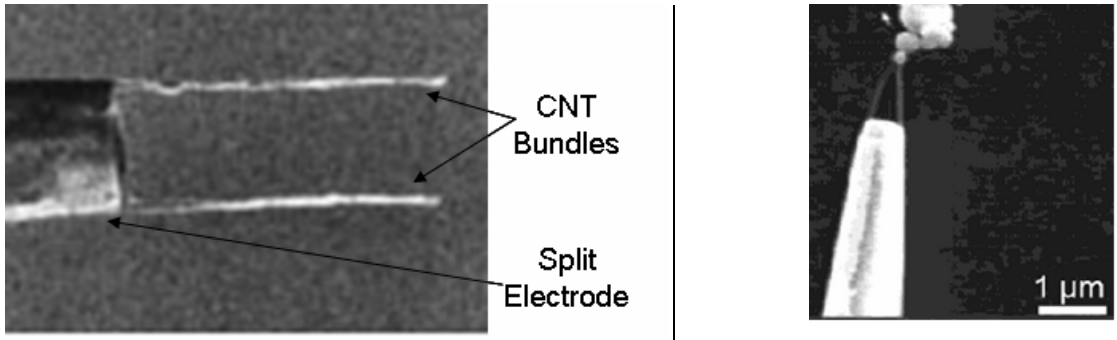

Figure 1.4: Close-up of CNT-based nanotweezers[2] (a) and nanotweezers in operation[3] (b).

When a voltage difference is applied at the split electrode, the electrostatic force produced by the ~10 V potential difference forces the CNT bundles, isolated on different electrodes, to bend towards each other. This small-scale deformation allows for the grasping (as shown in Fig. 1.4(b)), manipulation, and release of particles of 100 nm or less.

---

[2] Figure 1.4(a) reproduced with permission from P. Kim and C. Lieber. Science **286** (5447), 2149 (1999). Copyright 2007 by the American Association for the Advancement of Science.

[3] Figure 1.4(b) reproduced with permission from S. Akita and Y. Nakayama. Jap. J. App. Phys. **41** (6b), 4242 (2002). Copyright 2007 by the Institute of Pure and Applied Physics.

Electrostatic attraction has also been proposed as a method for actuating CNT-based mechanical relays [20], non-volatile memory [21], and transistors [22] at the nanoscale. The relay in Fig. 1.5(a) uses a voltage differential applied by the gate electrode (G) to deflect the CNT into contact with the drain electrode (D), thus completing an electrical circuit with the source (S) and drain electrodes. Mechanical tests showed a 9 nN load deflected the 1.8 μm long CNT 80 nm laterally. The device had a resonance frequency of 0.1 GHz, though the authors claim that smaller nanotubes could be used in future applications to allow for higher natural frequencies.

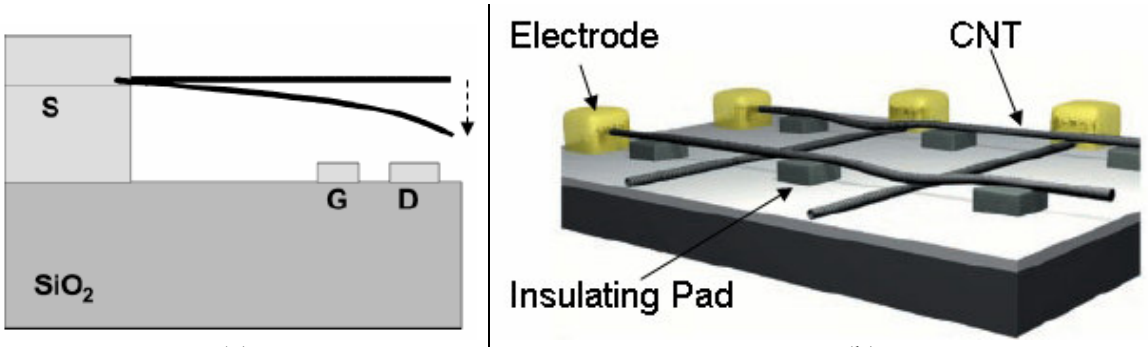

(a) (b)

Figure 1.5: Schematic of a CNT-based relay[4] (a) and CNT-based memory[5] (b).

Figure 1.5(b) shows a schematic of non-volatile CNT-based memory. The memory consists of a grid of CNTs that are perpendicular to one another. Electrodes at the end of each CNT allow for the application of a differential potetial. By applying these voltage differences to different CNT pairs, the overlayed CNTs may be brought into contact with those that are laying under it. Once in contact, van der Waals attractive forces hold the two CNTs in contact even without the presence of the potential difference, forming a non-volatile "ON" state. Simulation results indicate that this device could be operated at speeds greater than 100 GHz. The CNT-based transistor shown in Fig. 1.6(a) uses uses the lateral bending of three vertical MWCNTs to create electrical contacts. The outermost CNTs have opposite potentials applied to them. When the

[4] Figure 1.5(a) reproduced with permission from S.W. Lee, D.S. Lee, R.E. Morjan, S.H. Jhang, M. Sveningsson, O.A. Nerushev, Y.W. Park, and E.E.B. Campbell. Nano Lett. **4** (10), 2027 (2004). Copyright 2007 by the American Chemical Society.

[5] Figure 1.5(b) reproduced with permission from T. Rueckes, K. Kim, E. Joselevich, G.Y. Tseng, C. Cheung, and C.M. Lieber. Science **289** (5476), 94 (2000). Copyright 2007 by the American Association for the Advancement of Science.

central CNT has a potential applied to it, it feels an attractive electrostatic force to one of the outer CNTs. The outer CNT that the central CNT contacts depends on the sign of the potential applied to the central CNT. The attractive force caused by the 22.4 V potential difference induced deformation leading contact between the central and outer CNTs (1.4 μm in length), thereby making an electrical connection, as shown in Fig. 1.6(b).

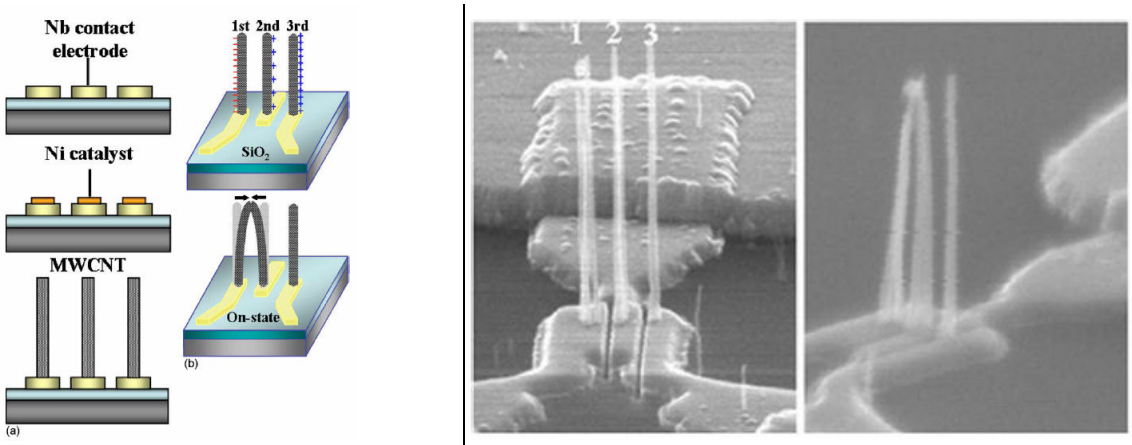

(a) (b)

Figure 1.6: Schematic of a CNT-based transistor (a) and its physical realization[6] (b).

1.2.2 Large-Deformation Devices

The second class of CNT-based devices are capable of deflections that are greater than 10% of their characteristic length and/or exhibit buckling phenomenon during operation. In one of the first demonstrations of a large motion CNT bearing, the torsional deflection of a CNT has been used to form a large rotation bearing [23-24] for a nano-scale pendulum. As shown in Fig. 1.7(a), the pendulum is suspended from a CNT which lays across two anchor pads, as seen in Fig. 1.7(b). The bond between the CNT and an anchor is detailed in Fig. 1.7(c). The authors in [23] report that the pendulum is supported by a total of forty carbon-carbon (C-C) bonds via the 1.5 nm diameter CNT. Using an external electric field for actuation, the pendulum is capable of 180^{o} of reversible rotation. The CNT bearing possess a spring constant of 2.86 nN·nm/rad and a resonance frequency of 0.1 MHz.

---

[6] Figure 1.6 reproduced with permission from J. E. Jang, S. N. Cha, Y. Choi, Gehan A. J. Amaratunga, D. J. Kang, D. G. Hasko, J. E. Jung, and J. M. Kim, Appl. Phys. Lett. **87**, 163114 (2005). Copyright 2007 by the American Institute of Physics.

(a) (b) (c)

Figure 1.7: Schematic of the rotational CNT bearing (a), an SEM photo of the realized device (b), and a close-up of the CNT anchor[7] (c).

It has been shown that a CNT may buckle if subjected to an axially compressive load. Since a buckled CNT undergoes a change in electrical properties it has been proposed [25] to use this phenomenon to produce a switch at the nano-scale. The authors have simulated the performance of this device and found that a 1% compressive strain will cause the device to buckle as shown in Fig. 1.8 and reside in the "ON" state. At 1.29% tensile strain the CNT was found to revert to its undeformed state. The authors have found that this buckling event is a bistable event for certain diameters of CNTs.

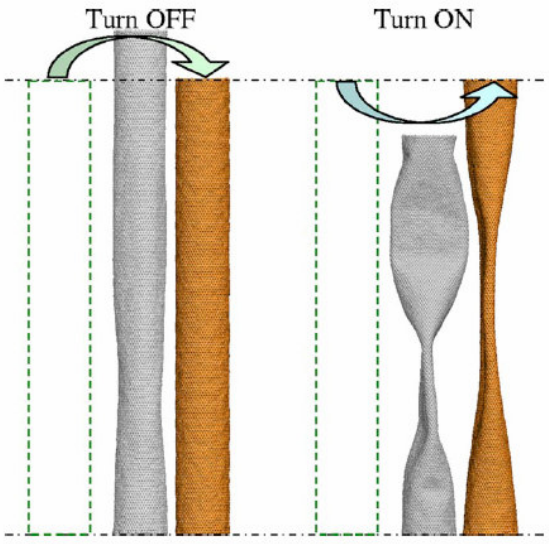

Figure 1.8: Theoretical operation of an axially bistable CNT switch[8].

---

[7] Figure 1.7 reproduced with permission from J.C. Meyer, M. Paillet, and S. Roth. Science **309** (5740), 1539 (2005). Copyright 2007 by the American Association for the Advancement of Science.

[8] Figure 1.8 reproduced with permission from T. Chang, J. Hou, and X. Guo, Appl. Phys. Lett. **88**, 211906 (2006). Copyright 2007 by the American Institute of Physics.

1.2.3 Relative Rotation/Sliding Devices

The third class of CNT-based mechanisms exploit the nested tube structure of multi-walled CNTs in order to make rotary and sliding bearings at the nano-scale. Rotary bearings [26-28] seem to be of most interest, as a technique has been developed for trimming the outer shell of a multi-walled CNT in order to free it from its anchor, allowing relative motion between the inner and outer shells of the CNT. The idea of a CNT-based motor, as shown in Fig. 1.9(a), may be realized [28] by actuating a rotor that rests on the outer shell of a multi-walled nanotube (~ 50 nm in diameter). When the rotor is actuated by the stator, the rotor causes the walls of the CNT to rotate relative to each other, forming a low-friction sliding contact bearing that allows the rotor a full 360 degree rotation, as shown in Fig 1.9(b).

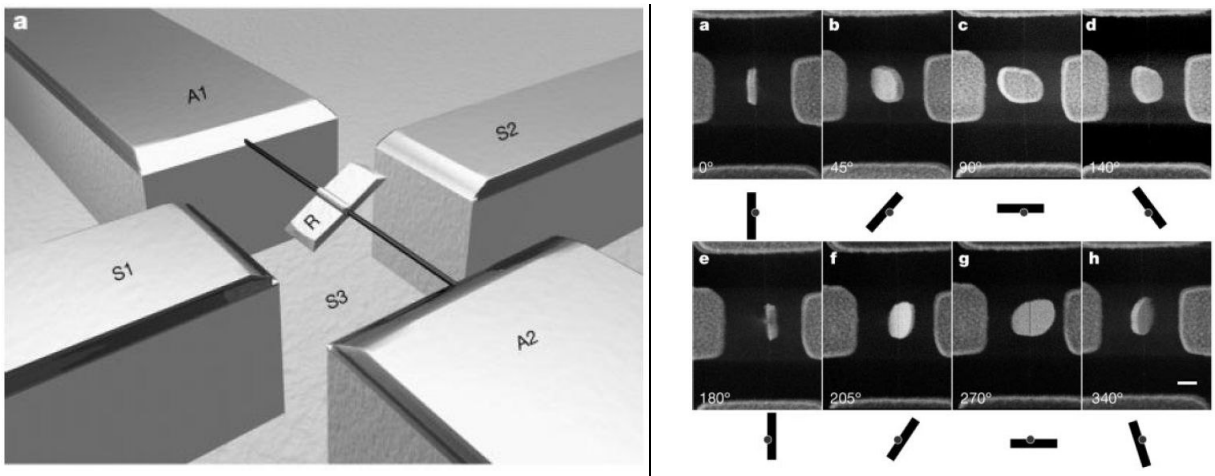

(a) (b)

Figure 1.9: Schematic of a CNT-based motor (a) and pictures of the rotor in motion (b)[9].

Research has also been conducted on using multi-walled CNTs to produce axial sliding bearings [29]. Figure 1.10(a) shows the axial sliding bearing concept. A multi-walled "bamboo" type CNT is anchored to a substrate at one end, while the other end is partially cleaved off, exposing an inner bundle of walls. The inner core of the CNT is then brought into contact with the target object, which sticks to the inner core via van der Waals forces. This target object is now supported by the bearing formed by the inner core sliding within the outer shell of the multi-walled CNT, as shown in Fig. 1.10(b).

---

[9] Figure 1.9 reproduced by permission from Macmillian Publishers Ltd: W. Han, A.M. Fennimore, T.D. Yuzvinksly, M.S. Fuhrer, J. Cumings, and A. Zettl. Nature **424** (6947), 408 (2003). Copyright 2007 by Macmillion Publishers Ltd.

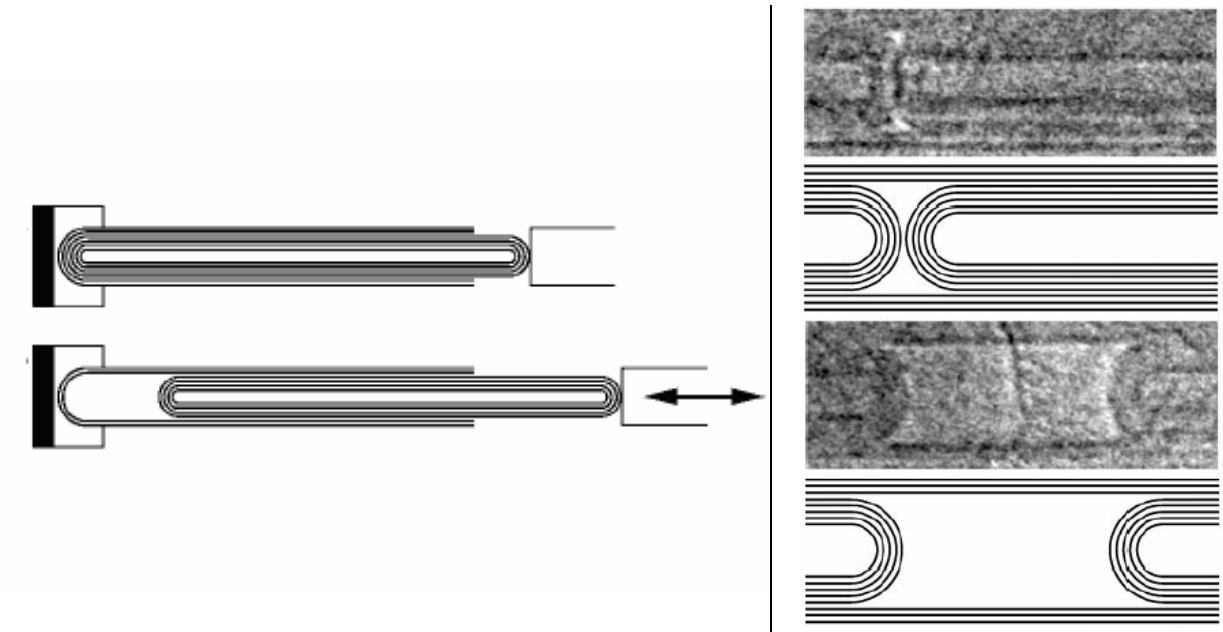

(a) (b)

Figure 1.10: Schematic of a CNT axial bearing (a) and pictures of the realized device (b)[10].

The major research to date for relative rotation/sliding devices has focused on (1) determining the energy required to initiate and maintain relative motion between walls of the CNT and to (2) model the energy that is dissipated within these devices. The simulated [29,30] and measured [31] "friction" surface stresses appear to be low enough (0.85 MPa) so that "wear", i.e. removal of the carbon atoms from the CNT structure, appears unlikely at room temperature.

1.2.4 Relevance of Prior Art to Carbon Nanotube-based Flexures

While the prior art has succeeded in creating a functional torsional bearing, a functional linear bearing has not been realized. Furthermore, the prior art has not yet been able to utilize multiple CNTs to create a true compliant system. The lack of simulated and fabricated large deformation compliant mechanisms with CNT-based flexural components means that nano-scale devices cannot be constructed using knowledge learned from macro- and micro-scale device research.

---

[10] Figure 1.10 reproduced by permission from J. Cumings, and A. Zettl, Science **289** (5479), 602 (2000).. Copyright 2007 by the American Association for the Advancement of Science.

1.3 Scope

There is a need to investigate the behavior of, and subsequently model the performance of, CNT-based flexures before a CNT-based nCM may be realized. While the benefits of, and need for, nCMs have been established, the knowledge generated from current research on devices with CNT-based components is inadequate for understanding and predicting the behavior of CNT-based flexures. CNT-based CMs are fundamentally different than macro-scale CMs because they are subject to nano-scale phenomenon such as van der Waals interactions and possess fundamentally different material properties.

1.3.1 Fundamental Issues

In, the following needs to be understood in order for CNTs to be usable as a flexural element in a nCM:

1. The kinematics of a CNT-based flexural element.
2. The relationship between the applied force and deformation of the CNT-based flexural element, i.e. the elastomechanics.
3. The actuation requirements, force and stroke, must be compatible with NEMS actuators.
4. If macro-scale CM design theory may be adapted and then applied to a CNT-based nCM.
5. If macro-scale CM design theory is unable to describe the behavior of CNT-based nCMs, is it possible to adapt it in order to capture nano-scale behaviors?

If satisfactory answers to all five questions may be found, then one may proceed in the design and fabrication of a CNT-based nCM.

While preliminary testing of CNTs via tensile testing and nano-indentation shows promise for their use as flexural members, this is not definitive proof. One needs to focus on the kinematic and elastomechanic behavior of a CNT-based flexural element In order to determine whether or not CNTs are good candidates for acting as the flexural members of a nCM. The kinematic and elastomechanic behavior of a nCM must be compared with that of a macro-scale CM. Since nano-scale forces such as van der Waals interactions become more dominant than many macro-scale body forces phenomena such as gravity at the level of CNTs, it is possible for

nCMs to act differently than macro-scale CMs. Furthermore, the range and loading characteristics must be looked at versus current state of the art nano-scale actuators to determine if a CNT-based nCM will be compatible with current actuation technologies.

If CNTs appear to be reasonable candidates for incorporation into nCMs, it will become necessary to predict their performance before device fabrication occurs. It is well known that the continuum descriptions of a material breaks down at ~10 nm, forcing one to make modifications to many basic engineering equations at this level. Since many precision engineers who design CMs are well-versed in analysis methods such as the psuedo-rigid-body model, it seems natural to adapt macro-scale CM design tools to suit the needs of describing nano-scale flexural elements. The fundamental differences in CNT mechanical behavior and macro-scale material behavior prevents us from knowing *a priori* if the pseudo-rigid-body model is capable of analyzing CNT-based nCMs.

1.3.2 Parallel Guiding Mechanism Case Study

In order to answer the above questions a ubiquitous element of macro- and micro-scale CMs, a four-bar parallel guiding mechanism (PGM), will serve as a case study. PGMs are one degree-of-freedom CMs that consist of two flexural members and two rigid members, as shown in Fig. 1.2 in section 1.1.2. When a load is applied parallel to the coupler bar, the coupler bar trajectory is an arcuate path. Over small linear deflections the lateral deflection is negligible and the device operates such that the coupler bar appears to translate only in a direction parallel to the grounding bar. Figure 1.11 shows an exploded view of a one degree-of-freedom linear motion stage where the central stage is actuated by two comb drives. When PGMs a and b are combined in series, as shown in set 1, it is possible to move the central stage along a linear path. Note that by having sets 1 and 2 operate in parallel the out of plane deflection error of the stage is minimized. The use of compliant PGMs in precision and high–cycle mechanical systems predates 1989 [32] for micro–scale devices and 1937 [33] for macro–scale devices.

A PGM is a basic building block of many macro- and micro-scale compliant systems. The investigation of the kinematic and elastomechanic performance of a nano-scale PGM will lead to the design and fabrication of more complicated systems that incorporate the PGM as a basic element. In order to understand how a nano-scale PGM will behave, molecular mechanics

and molecular dynamics simulations will need to be carried out on a model of a CNT-based PGM [34,35].

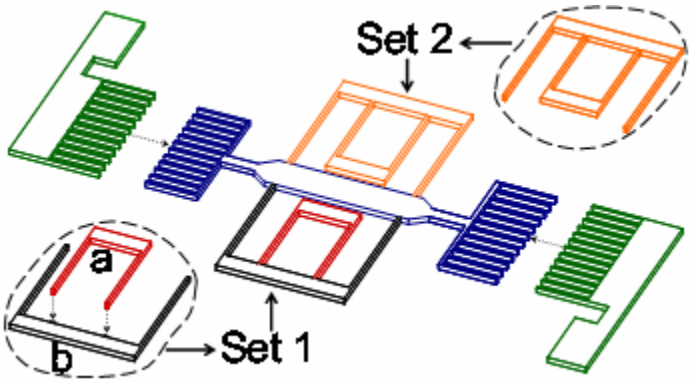

Figure 1.11: A one degree-of-freedom linear motion stage.

The results of these simulations will make it possible to evaluate the pseudo-rigid-body model as a tool for analyzing nCMs.

1.3.3 Thesis Outline

This thesis focuses on understanding and modeling the performance of a nCM with CNT-based flexural components via the case study of a nano-scale PGM. Chapter 1 introduces the problem of replicating macro- and micro-scale device performance at the nano-scale while at the same time establishing a need for nCMs. Chapter 2 focuses on the structural and mechanical properties of CNTs relevant to the design of CMs. Chapter 3 introduces molecular modeling from a mechanical engineering perspective. Chapter 3 also introduces the psuedo-rigid-body model to familiarize the reader with a conventional CM design modeling approach. Chapter 4 presents the model of the nano-scale PGM used for the molecular mechanics and dynamics simulations. Chapter 4 also presents the kinematic and elastomechanic results of the simulations carried out on the model of the nano-scale PGM. Chapter 5 compares and contrasts the psuedo-rigid-body model of the CNT-based nano-scale PGM with the molecular modeling results presenting in Chapter 4. Chapter 5 also presents optimizations to the psuedo-rigid-body parameters in order to more accurately predict the kinematic and elastomechanic behavior of a nano-scale PGM. Chapter 6 summarizes the contributions of the thesis research and provides a discussion of the future work that may be pursued as a result of the contributions of this thesis.

Chapter 2

Carbon Nanotubes

Since the discovery of CNTs by Iijima in 1991 [3], research from many different science and engineering disciplines has focused on trying to understand the structure, mechanical properties, electrical properties, growth mechanisms, and ways to characterize CNTs. In order to fully realize the potential of CNT-based mechanisms it is important to understand the unique structural and mechanical properties of CNTs. This chapter will condense more than a decades worth of research into a few pages with the most relevant material for designing CNT-based nCMs.

2.1 Structure of Carbon Nanotubes

CNTs are three-dimensional carbon molecules that are a member of the fullerene structural carbon family. To understand the structure of a CNT it is necessary to discuss the structure of graphene. Graphene, a single plane of graphite, exists as a planar sheet of carbon atoms whose lattice consists of hexagonal graphene unit cells, as shown in Fig. 2.1. The hexagonal structure means that each carbon atom is bonded aromatically to its neighboring atoms via sp^2 hybridized bonds. The spacing between the graphene unit cells, a_{guc}, is 0.246 nm [36], which corresponds to an equilibrium C-C bond length, $a_{c\text{-}c}$, of 0.142 nm, less than the C-C bond length found in diamond of 0.154 nm [36]. This sp^2 bond configuration produces some of the strongest materials found in nature. Each carbon atom is bonded to three other carbon atoms via σ bonds with 120^o of spacing. The carbon atom's fourth valence shell electron forms a delocalized π bond which is oriented perpendicular to the plane of carbon-carbon σ bonding. This bond configuration leads to a lattice energy of 7.4 eV per atom [37], which is 37% higher than the lattice energy of diamond, 5.4 eV per atom [38].

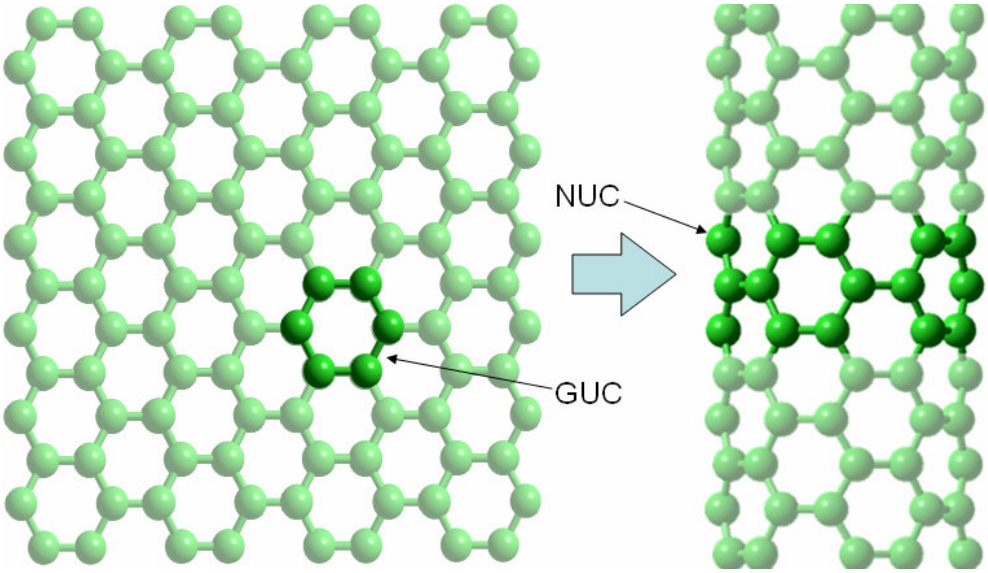

Figure 2.1: Graphene sheet to CNT analogy.

A CNT may be thought of as a sheet of graphene rolled along a chiral vector, $\vec{C}$, as shown in Fig. 2.1. The chiral vector is a linear combination of two base vectors, $\vec{a}_1$ and $\vec{a}_2$, which are oriented 60° from each other, as shown in Fig. 2.2. The chiral vector is defined using the chiral indicies (n,m) and the relation presented in Eq. 2.1.

$$\vec{C} = n\vec{a}_1 + m\vec{a}_2 \tag{2.1}$$

The chiral vector also defines the diameter, d_{cnt}, of a carbon nanotube, as shown in Eq. 2.2.

$$d_{cnt} = a_{guc}\frac{\sqrt{n^2 + nm + m^2}}{\pi} \tag{2.2}$$

The energy per atom required to roll a graphene sheet into a CNT, U_r, is inversely proportional to the square of the CNT diameter [36], as shown in Eq. 2.3.

$$U_r = \frac{\sqrt{3}E_g\, t_g^3\, a_{guc}^2}{24 d_{cnt}^2} \tag{2.3}$$

For this formulation the elastic modulus of graphene, E_g, is 1.06 TPa [36] and the thickness of the graphene sheet, t_g, is 0.34 nm [36]. The wrapping angle, θ_c, that the chiral vector makes with basis vector $\vec{a}_1$ is found using the relation shown in Eq. 2.4.

$$\theta_c = \tan^{-1}\left(\frac{\sqrt{3}m}{m + 2n}\right) \tag{2.4}$$

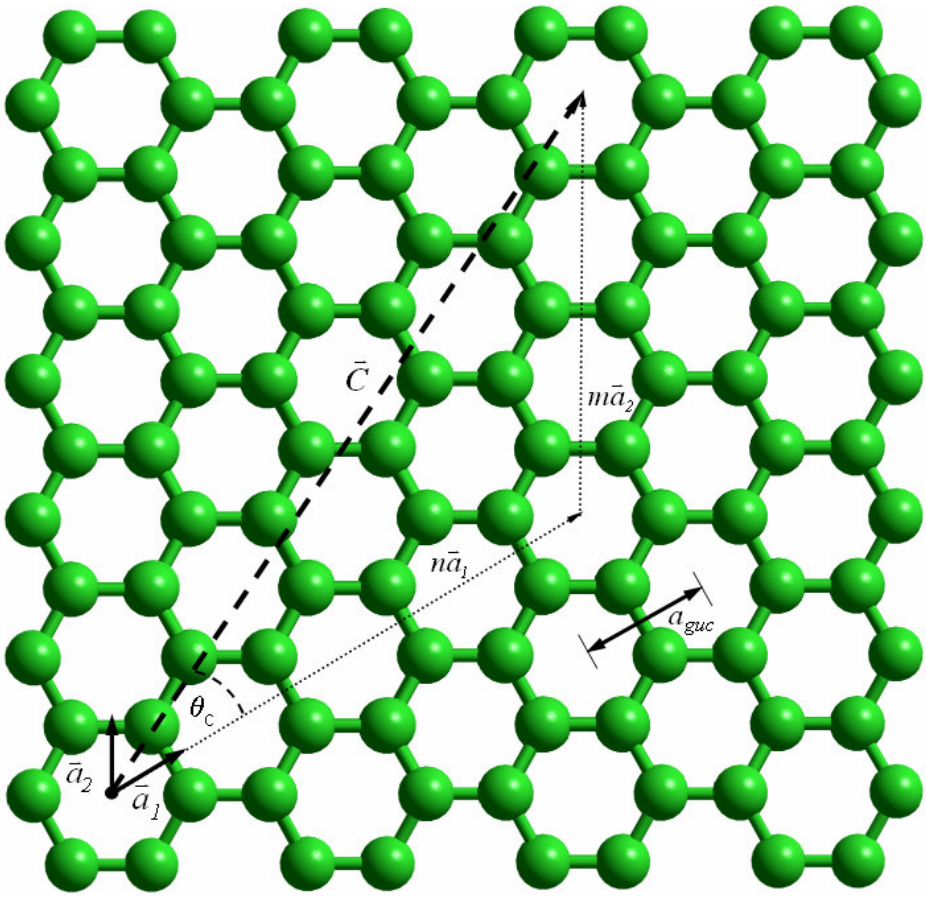

Figure 2.2: Chiral vector definition on a graphene sheet.

The chiral indices also have a large effect on the electrical properties of CNTs. The difference of the indicies of CNTs that behave like conductors, referred to as a "metallic" tubes, are always an integer, q, multiple of three, as shown in Eq. 2.5.

$$3\boldsymbol{q} = |\boldsymbol{n} - \boldsymbol{m}| \qquad \text{where } \boldsymbol{q} = 0, 1, 2, \ldots \tag{2.5}$$

Any other index pair indicates the tube is semiconducting with an energy bandgap, U_{gap}, that is proportional to a hopping parameter, ζ, (usually 2.5-3.2 eV) as is shown in Eq. 2.6 [11].

$$U_{gap} = a_{guc}\frac{\zeta}{d_{cnt}} \tag{2.6}$$

Finally, the chiral indicies lead to three types of nanotubes: 1) zig-zag (Fig. 2.3(a)), 2) armchair (Fig. 2.3(b)), and 3) chiral. Zig-zag CNTs have $m = 0$, leading to a wrapping angle of 0^o and diameters that are directly proportional to n. Armchair nanotubes have a repeated index ($m = n$), leading to diameters proportional to $\sqrt{3}n$ and wrapping angles of 30^o. This bounds the third class of CNTs, which includes all the other combinations of indicies, to have wrapping angles between 0^o and 30^o.

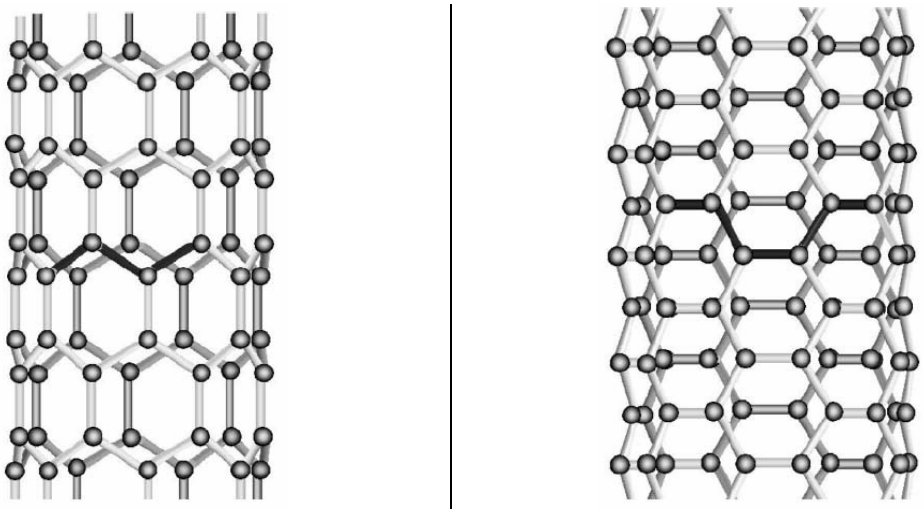

(a) (b)

Figure 2.3: Zig-zag (a) and armchair (b) carbon nanotube chiralities[1].

Once a chiral vector is defined, it becomes necessary to introduce the idea of a nanotube unit cell. The nanotube unit cell, shown in Fig 2.1, is a single cylindrical building block of a CNT. A CNT is formed by stacking unit cells on top of one another, thus making the length of a CNT, L_{cnt}, an integer multiple of the nanotube unit cell height, T_{nuc}. The nanotube unit cell height depends solely on the indicies of the CNT, as shown in Eq. 2.7.

$$T_{nuc} = a_{guc}\frac{\sqrt{3\left(n^2+nm+m^2\right)}}{d_R} \tag{2.7}$$

The variable in the denominator of Eq. 2.7, d_R, is itself a function of the greatest common divisor (gcd) of m and n and its definition is given in Eq. 2.8.

$$d_R = \gcd(2m+n,\ 2n+m) \tag{2.8}$$

One may also find the number of graphene unit cells, N_{guc}, per nanotube unit cell using the relation shown in Eq. 2.9.

$$N_{guc} = \frac{2\left(n^2+nm+m^2\right)}{d_R} \tag{2.9}$$

Since each graphene unit cell is defined by two carbon atoms, the total number of atoms per nanotube unit cell is $2N_{guc}$.

It is important to distinguish between single-walled carbon nanotubes (SWCNTs) and multi-walled carbon nanotubes (MWCNTs). MWCNTs consist of multiple SWCNTs that are

[1] Figure 2.3 reproduced by permission from Elsevier: C. Li and T.W. Chou. Int. J. Sol. and Structures **40** (10), 2487 (2003). Copyright 2007 by Elsevier.

coaxially nested. Each wall of the MWCNT may have a different chirality, though these chiralities are usually complementary matched in order to minimize the non-bonded energy between the walls of the MWCNT. The walls are usually spaced 0.341 nm apart, which is the interlayer spacing of graphene layers in graphite [36], though Kiang et. al has found that the wall separation is inversely proportional to the number of layers in the MWCNT and directly proportional to the curvature [40]. The nested structure of a MWCNT allows it to reach diameters of up to 100 nm, while SWCNTs are usually limited to 5 nm or less. Furthermore, the non-bonded interactions between the walls of the MWCNT lead to changes in their mechanical properties, in many cases making them approach that of graphite. This is because graphite is structurally similar to a deck of cards, i.e. it is a stack of graphene sheets.

The two most common ways to destroy the structure of a CNT under load is via bond breaking or defect formation. In order to break an atomic bond the C-C bond length must be stretched to 0.177 nm [41], corresponding to 25% bond strain. It is also possible for a CNT wall to develop defects caused by bond rotations, which is the more common type of CNT failure. This type of failure occurs when four clustered hexagonal graphitic unit cells recombine to form two pentagons and two heptagons, as shown in Fig. 2.4, and is known as a Stone-Wales deformation.

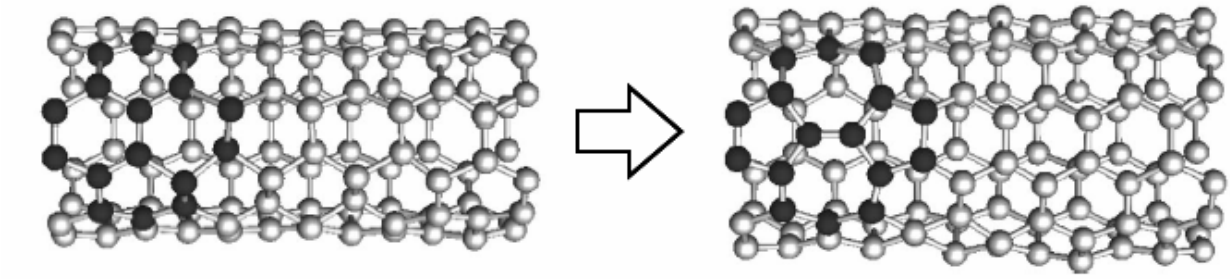

Figure 2.4: Stone-Wales defect in a SWCNT [2].

In simulations of a SWCNT in axial tension, Nardelli, Yakobson, and Bernholc found that reversible defects occur at 5% extension [42]. The Stone-Wales deformation is a method of relieving strain energy in the wall of the CNT. Nardelli found that at 10% strain the presence of a defect lowered the strain energy of the SWCNT by 1.77 eV when compared with the defect-free configuration at the same loading level [42]. This is because the heptagons are capable of

[2] Figure 2.4 reproduced with permission from M.B. Nardelli, B.I. Yakobson, and J. Bernholc. Phys. Rev. B **57** (8), R4277 (1998). Copyright 2007 by the American Physical Society.

straining the same amount as a hexagon without making each individual C-C bond as long as they would be in the hexagon. Nardelli also provided simulated results for the activation energy of a defect, which decreases as the SWCNT is loaded. The results of the study are presented in Fig. 2.5.

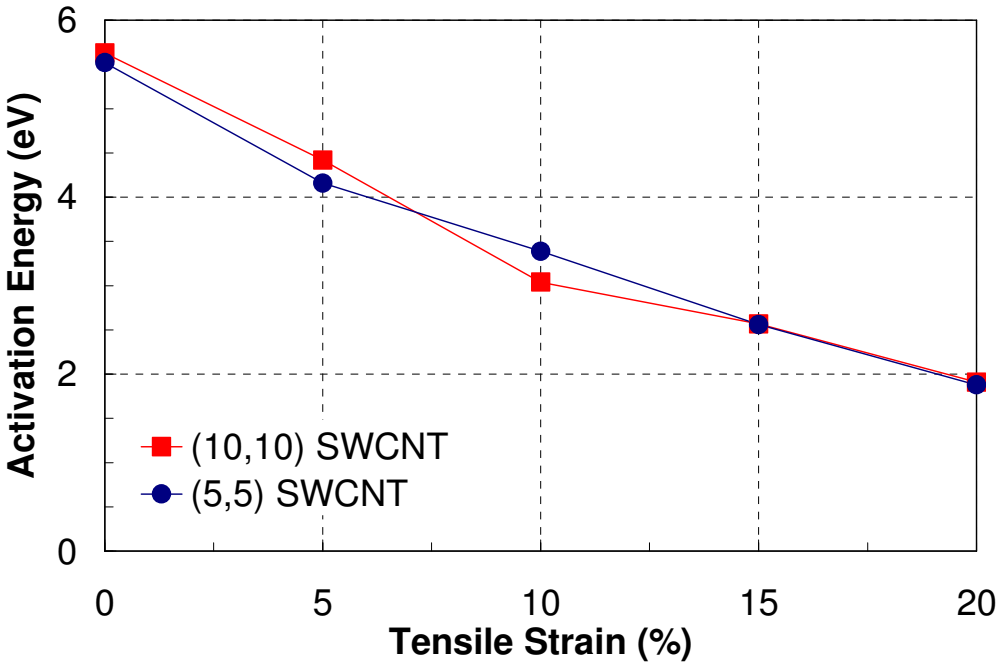

Figure 2.5: Activation energy for a Stone-Wales defect in a SWCNT.

It is important to note that while these Stone-Wales deformations may be reversible under ideal conditions, it is possible for them to serve as nucleation sites for plastic deformation (i.e. dislocations) in the wall of the SWCNT.

2.2 Physical Properties of Carbon Nanotubes

As discussed in section 2.1, the aromatic carbon bonds present in the nanotube are stronger than the sp^3 bonds present in diamond, which is why CNTs possess such unique mechanical properties. The atomic structure of a CNT also leads to interesting kinematic and elastomechanic phenomenon such as buckling and bi-stable geometries. This section will focus on the mechanical properties associated with axial, bending, and torsional deformations.

2.2.1 Continuum Definitions of Mechanical Properties at the Nano-scale

Before any discussion of mechanical properties of CNTs may begin, it is important to note the problems associated with using continuum descriptions of macro-scale mechanical properties at the nano-scale. All macro- and micro-scale continuum relations assume that a cross-sectional area or moment of inertia may be provided for the structure. Since a CNT is really a planar structure only one atom in thickness, it becomes difficult to prescribe a continuum thickness to the structure. In the sections to follow we will see that some authors choose to define the thickness of a CNT, t_{cnt}, as the equilibrium van der Waals spacing between graphene sheets while others choose to make the thickness of the CNT equal to the diameter of a carbon atom. To further complicate matters, some authors define the cross-sectional area of a carbon nanotube to be a solid rod, while others model it as a hollow cylinder. Harik has proven by geometric similitude that a SWCNT may be considered a thin-walled cylindrical shell, a thick-walled cylindrical shell, or a solid rod based on five unique ratios [43]. The inability to define a thickness of a CNT also leads to trouble with establishing its mass in a macro-scale sense. While the bulk density of CNTs is known to be 2020 kg/m^3 [44], defining the mass of an individual CNT is best done by adding the mass of each individual atom in the structure rather than defining a local density and volume. In order to alleviate this confusion, whenever an elastic modulus is quoted the diameter of the CNT as well as the assumed thickness will also be provided. Another value that will be quoted will be the product $E \cdot t_{cnt}$, which may be thought of as an in-plane stretching stiffness for a CNT cross-section for the CNT cross-section. We will see in the next section that this product will be important for comparing data from different published studies.

2.2.2 Properties of Axial Deformation

Due to the sp^2 structure of the carbon nanotube, the σ bonds in plane tend to make the CNT quite stiff in the axial direction, while compliant in the tangential direction. Much simulation and experimental work has been conducted in order to predict the elastic modulus, E, Poisson's ratio, ν, and failure strength, σ_f, and failure strain, ε_f, for axially loaded CNTs. It will become important to distinguish between axial elongation and compression because the elastomechanic behaviors exhibited in both are quite different. Table 2.1 details the simulated and experimental results found in the literature for the elastic properties of CNTs in tension.

From the published literature, the elastic modulus for a SWCNT has an average value of 1.32 TPa. In contrast the MWCNT elastic modulus seems to approach that of graphite with its approximate value of 1 TPa.

Table 2.1: Elastic properties of CNTs in axial extension.

Test Type	Tube Type	Chirality	d_{cnt} (nm)	L_{cnt} (nm)	t_{cnt} (nm)	E (TPa)	ν	$E \cdot t_{cnt}$ (nN/nm)	Ref.
Simulation	SWCNT	(9,0)	0.71	N/A	0.34	1	N/A	340	[39]
Simulation	SWCNT	(10,10)	1.36	N/A	0.34	1.24	N/A	422	[45]
Simulation	SWCNT	(25,0)	1.96	N/A	0.129	1.44	N/A	186	[46]
Simulation	SWCNT	(10,10)	1.36	2.48	0.0894	3.86	0.149	345	[47]
Simulation	SWCNT	(10,10)	1.36	N/A	0.34	0.973	0.28	331	[48]
Simulation	SWCNT	N/A	1.12	N/A	0.286	1.024	0.16	293	[49]
Simulation	SWCNT	(10,10)	1.36	N/A	0.34	0.8	0.14	272	[50]
Simulation	MWCNT	N/A	4	N/A	0.34	1	N/A	N/A	[50]
Experiment	SWCNT	N/A	1	5	0.154	0.950	N/A	146	[51]
Experiment	SWCNT	N/A	1.36	N/A	0.34	1	N/A	340	[52]
Experiment	MWCNT	N/A	30	N/A	0.34	0.95	N/A	N/A	[53]

It is because of the variation in the assumed wall thickness (from 0.34 nm to 0.068 nm) that the elastic modulus of a SWCNT cannot be considered a constant. A better constant for a SWCNT is the product $E \cdot t_{cnt}$, whose constant value may be considered to be 297 nN/nm with a standard deviation of 85 nN/nm. The Poisson's ratio for a SWCNT in axial tension has an average value of 0.18.

Simulated and experimental work has also been conducted to find the approximate failure strength and strain for CNTs in tension. The results of this published research is presented in Table 2.2. The simulated failure stress for a SWCNT is approximately 88 GPa assuming a wall thickness of 0.34 nm, while the simulated failure strain, ε_f, varies wildly from study to study. However, there are considerable differences between the experimental and simulated results for the values of SWCNT failure. The average experimental failure stress for a SWCNT is 27 GPa, 70% lower than the simulated results. The experimental failure strain also varies wildly from test to test. This difference between experimental and simulated work could be due to the

presence of defects, which are nearly impossible to detect during these experiments, as well as imperfect sample loading such as a failure to put the CNT in pure tension.

Table 2.2: Failure properties of CNTs in axial extension.

Test Type	Tube Type	Chirality	d_{cnt} (nm)	L_{cnt} (nm)	t_{cnt} (nm)	σ_f (GPa)	ε_f	Ref.
Simulation	SWCNT	(30,30)	4.07	N/A	0.334	88	0.443	[3]
Simulation	SWCNT	(6,6)	0.81	N/A	0.34	87.2	0.073	[41]
Simulation	SWCNT	(10,0)	0.78	N/A	N/A	N/A	0.16	[54]
Simulation	SWCNT	(5,5)	0.68	N/A	N/A	N/A	0.24	[54]
Experiment	SWCNT	N/A	1	5	0.154	25	0.30	[51]
Experiment	SWCNT	N/A	1.36	N/A	0.34	30	0.053	[52]
Experiment	MWCNT	N/A	30	N/A	0.34	2.9	0.12	[53]

Another explanation is provided in [41], where the authors have found that the critical failure stress and strain is directly proportional to the rate of strain. Since most of the experimental work in the literature has not provided the rate of strain, it may not be appropriate to use these experimental results for comparison to the simulated tension tests.

Less published research is available on the behavior of CNTs in compression. Table 2.3 shows the simulated and experimental results for axial compression of a CNT. The simulated results for a SWCNT show that the product $E \cdot t_{cnt}$ is within the standard deviation of the results from the axial tension experiments. Furthermore, the simulated Poisson's ratio for a SWCNT has a value similar to the one found for axial tension.

Table 2.3: Elastic properties of CNTs in axial compression.

Test Type	Tube Type	Chirality	d_{cnt} (nm)	L_{cnt} (nm)	t_{cnt} (nm)	E (TPa)	ν	$E \cdot t_{cnt}$ (nN/nm)	Ref
Simulation	SWCNT	(7,7)	0.95	6	0.066	5.5	0.19	363	[55]
Experiment	SWCNT	N/A	1.4	N/A	N/A	3	N/A	N/A	[56]
Experiment	MWCNT	N/A	10-20	N/A	N/A	2.44	N/A	N/A	[56]

The main difference between axial compression and tension is that it in compression a CNT is subject to buckling at a critical buckling strain, ε_c. A visual depiction of compressive buckling is shown in Fig. 1.8. Researchers have simulated the buckling of SWCNTs with much success. Their results are presented in Table 2.4. From the above table it is easily shown that the

critical buckling strain is highly dependant on nanotube diameter, as one would expect from macro-scale beam theory.

Table 2.4: Failure properties of CNTs in axial compression.

Test Type	Tube Type	Chirality	d_{cnt} (nm)	L_{cnt} (nm)	t_{cnt} (nm)	ε_c	Ref
Simulation	SWCNT	(55,0)	4.31	38	0.068	0.0101	[25]
Simulation	SWCNT	(7,7)	0.95	6	0.066	0.05	[55]
Simulation	SWCNT	(8,0)	0.63	4.3	0.0894	0.13	[57]

A relationship for the critical buckling strain to SWCNT diameter for tubes with an aspect ratio L_{cnt}/d_{cnt} less than ten is presented in Eq. 2.10 [55].

$$\varepsilon_c = \frac{(0.077 \text{ nm})}{d_{cnt}} \quad \text{for } \frac{L_{cnt}}{d_{cnt}} \le 10 \tag{2.10}$$

For SWCNTs with greater aspect ratios one should use the formulation [55] presented in Eq. 2.11.

$$\varepsilon_c = \frac{1}{2}\frac{\pi^2 d_{cnt}^2}{L_{cnt}^2} \quad \text{for } \frac{L_{cnt}}{d_{cnt}} \ge 10 \tag{2.11}$$

For small diameter SWCNTs, Liew et. al [57] have related the critical buckling load to the classical Euler beam buckling formulations, as shown in Eq. 2.12. The moment of inertia, I, is considered to be that of a solid rod and E is taken to be 1.28 TPa.

$$P_c = \frac{4\pi EI}{L^2} \quad \text{for } d_{cnt} \le 1.03 \text{ nm} \tag{2.12}$$

It has also been shown [25] that the buckling of an SWCNT is bistable if the CNT is 2-6 nm in diameter. If the tube is any larger than 6 nm, the van der Waals forces dominate the buckled geometry, and the buckling event is not reversible. It was shown that a 38 nm long (55,0) SWCNT would need 1.01% compressive strain to buckle, and 1.29% tensile strain to revert back to an unbuckled geometry [25].

2.2.3 Properties of Bending Deformation

CNTs undergoing bending deformation represent the largest range of elastic motion that is offered in nature. Since this large range of motion depends on the geometric nonlinearity of the CNT in large-angle bending, it is necessary to separate the discussion of SWCNTs and MWCNTs. Table 2.5 summarizes the experimental and simulated mechanical properties of SWCNTs found in the literature. When the wall thickness is taken to be approximately 0.08 nm, the elastic modulus is approximately 4.9 GPa. The product $E \cdot t_{cnt}$ is again found to be a constant

equal to 382 nN/nm with a standard deviation of 41 nN/nm. This is a higher value than previously determined in the tension/compression studies, and a t-test between the two data sets confirms that this difference is statistically significant with 98% confidence. This result suggests that SWCNTs experiencing combined loading may possess an elastic modulus that is a combination of the stretching and bending moduli.

Table 2.5: Elastic properties of SWCNTs in bending.

Test Type	Tube Type	Chirality	d_{cnt} (nm)	L_{cnt} (nm)	t_{cnt} (nm)	E (TPa)	ν	$E \cdot t_{cnt}$ (nN/nm)	Ref
Simulation	SWCNT	(5,5)	0.68	N/A	0.074	5.1	0.24	377	[58]
Simulation	SWCNT	N/A	N/A	N/A	0.075	4.7	0.34	353	[59]
Simulation	SWCNT	(13,0)	1.02	8	0.075	4.84	0.19	363	[60]
Experiment	SWCNT	N/A	3.1	605	0.34	1.2	N/A	408	[61]
Experiment	SWCNT	N/A	5	N/A	N/A	1.2	N/A	N/A	[62]
Experiment	SWCNT	N/A	1.5	36.8	0.34	1.33	N/A	452	[63]
Experiment	SWCNT	N/A	1.4	N/A	0.34	1	N/A	340	[64]
Experiment	SWCNT	N/A	3	1040	0.34	1.31	N/A	445	[65]

The difference in the stretching and bending moduli is attributed to the method of bond deformation in the CNT. During axial loading, bonds tend to be stretched while in a bent CNT the bonds tend to rotate relative to each other to minimize energy in the structure. This is possible because in bending the cross-section of a CNT deforms from a circle into an oval, while in an axial loaded CNT the cross-section remains constant.

It is important to note that at a critical angle the SWCNT transitions from distributed beam bending to localized bending creating a kink in the CNT. This kink that forms during tube buckling allows the large motion bending that is seen in simulated and experimental SWCNT tests, as shown in Fig. 2.6. Pantano, Parks, and Boyce found that the large-angle bending was reversible until the SWCNT diameter exceeded 6 nm [60], at which point the van der Waals forces dominated the elasticity of the atomic lattice and the SWCNT would not come unkinked. For smaller diameter SWCNTs it has been shown that the bending angle may approach 110^{o} and the SWCNT will revert back to its original undeformed state [66].

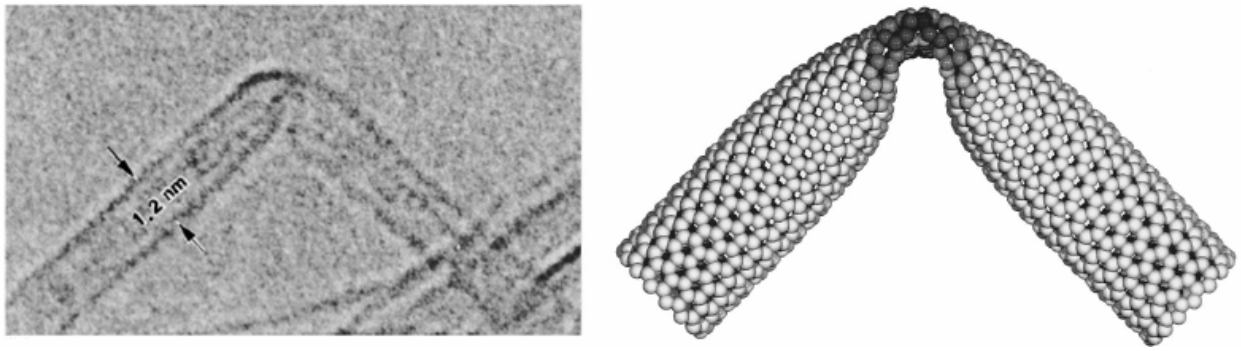

Figure 2.6: Localized buckling during SWCNT bending[3].

A relationship between tube diameter and the critical local curvature, K_c, has been found [55] and is shown in Eq. 2.13.

$$K_c = \frac{0.155 \text{ nm}}{d_{cnt}^2} \tag{2.13}$$

Wong, Sheehan, and Lieber have tested a MWCNT in bending by probing it with an AFM tip and found that a 32.9 nm MWCNT had an elastic modulus of 1.26 TPa [67]. This is a lower modulus of elasticity than found in SWCNTs, suggesting that as the number of walls grows, the properties of an MWCNT approach that of graphite, whose elastic modulus is 1.06 TPa [48]. A relationship between the number of walls, N, in the MWCNT and the resulting elastic modulus, E_N, has been found [59] and is shown in Eq. 2.14.

$$E_N = \frac{N}{N - 1 + \frac{t_{cnt}}{d_{cnt}}} \frac{t_{cnt}}{d_{cnt}} E_{swcnt} \tag{2.14}$$

It should be noted that the authors have chosen $E_{swcnt} = 4.7$ TPa and $t_{cnt} = 0.075$ nm.

The large-scale bending deformations of MWCNTs do not at all resemble those of SWCNTs. In an SWCNT a kink occurs because the cross-section suffers from a large geometric nonlinearity as the walls collapse from an undistorted circular cross-section. The van der Waals interactions between the walls of the MWCNT add a significant resistance to cross-sectional collapse. As a result of the nested wall van der Waals interactions, a MWCNT does not form a localized kink, but instead, a wave-like distortion [68] along the inside edge of the CNT, as shown in Fig. 2.7.

[3] Figure 2.6 reproduced with permission from Sumio Iijima, Charles Brabec, Amitesh Maiti, and Jerzy Bernholc, Journal of Chemical Physics, 104, 2089 (1996). Copyright 2007 American Institute of Physics.

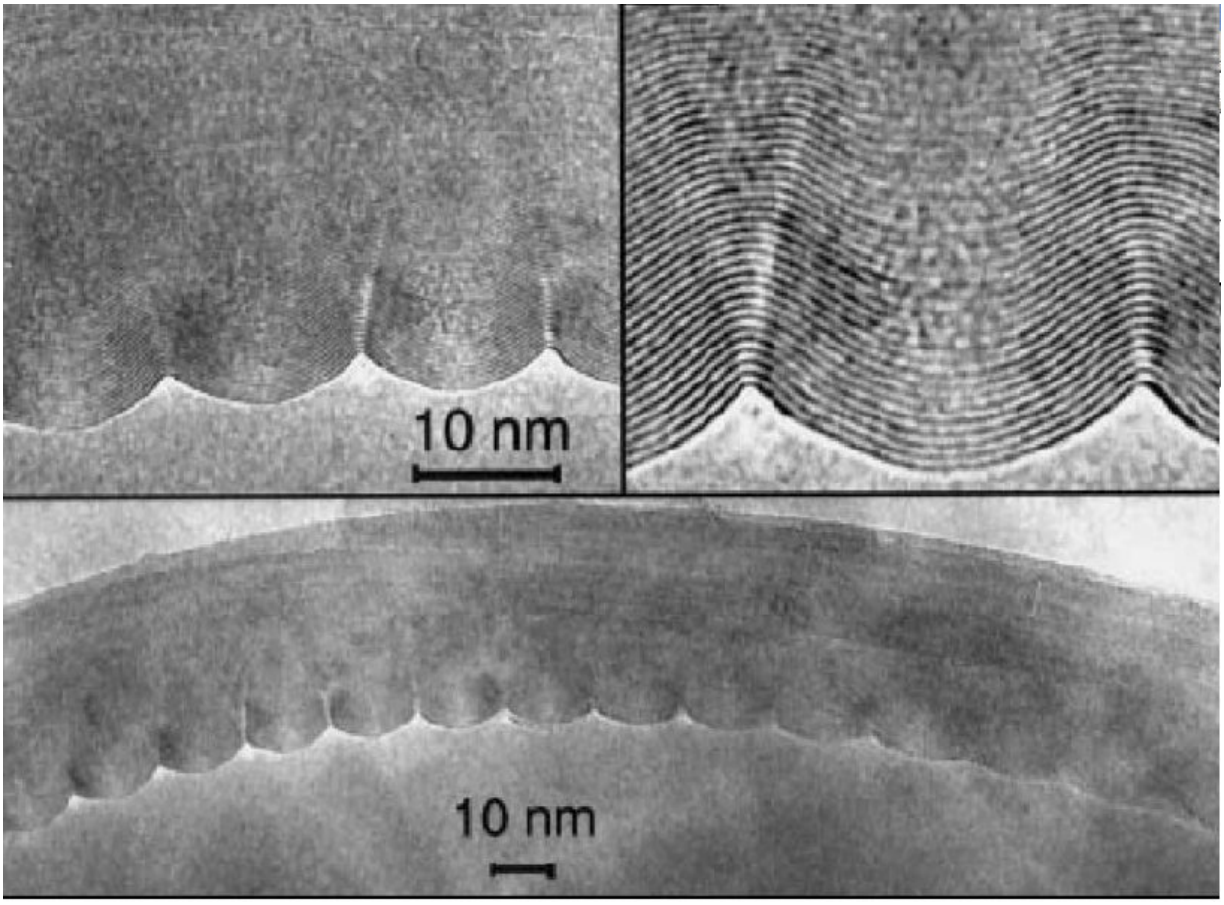

Figure 2.7: MWCNT wave-like distortion during bending[4].

2.2.4 Properties of Torsional Deformation

CNTs may also be used as torsional compliant members. Table 2.6 summarizes the simulated and experimental work found in the literature regarding torsional properties of CNTs. The literature seems to show a shear modulus, G, that is less than 1 TPa. Again we defined a product $G \cdot t_{cnt}$ in order to standardize a value of shear modulus with respect to the wall thickness. The average of this product $G \cdot t_{cnt}$ was found to be 149 nN/nm with a standard deviation of 22 nN/nm for the simulated data. Lu and Zhang found the torsional failure stress to be 46.7 GPa and the failure strain to be 0.34 for a (30,12) SWCNT [4].

[4] Reprinted Figure 2.7 with permission from P. Poncharal, Z.L. Wang, D. Ugarte, W.A. de Heer. Science **283** (5407), 1513 (1999).. Copyright 2007 by the American Physical Society.

Table 2.6: Elastic properties of SWCNTs in torsion.

Test Type	Tube Type	Chirality	d_{cnt} (nm)	L_{cnt} (nm)	t_{cnt} (nm)	G (GPa)	$G \cdot t_{cnt}$ (nN/nm)	Ref
Simulation	SWCNT	(9,0)	0.71	N/A	0.34	370	126	[39]
Simulation	SWCNT	(25,0)	1.96	N/A	0.68	270	184	[46]
Simulation	SWCNT	(10,10)	1.36	2.48	0.0894	1680	150	[47]
Simulation	SWCNT	(10,10)	1.36	N/A	0.34	450	153	[48]
Simulation	SWCNT	N/A	1.12	N/A	0.286	470	134	[49]
Experiment	SWCNT	N/A	4.5	N/A	0.34	6.5	2	[64]

It is also possible for a SWCNT in torsion to buckle. The first mode of failure resembles a flat shoelace that has been twisted multiple times. In this failure configuration the walls of the MWCNT collapse onto each other. A relation between the length and diameter of a SWCNT to its torsional failure angle, ϕ_c, has been found [55] and is shown in Eq. 2.15.

$$\phi_c = \frac{(0.055\ \text{nm}^{3/2})L_{cnt}}{d_{cnt}^{2/5}} \quad \text{for } \frac{L_{cnt}}{d_{cnt}^{5/2}} \le 136 \tag{2.15}$$

For larger tube aspect ratios, [55] has provided another critical failure angle that is shown in Eq. 2.16.

$$\phi_c = 2(1+\nu)\pi \quad \text{for } \frac{L_{cnt}}{d_{cnt}^{5/2}} \ge 136 \tag{2.16}$$

The Poisson's ratio chosen for this formulation is 0.19, leading to a constant torsional buckling angle of 7.48 rad or 428°.

The elastic torsional deformation of MWCNTs is not that different from that of SWCNTs. If the torsional load is applied to only one wall of the MWCNT, than the surrounding walls produce a small resistive force due to van der Waals attraction [29-31] which may be combined with the analysis from the studies on a SWCNT to find an equivalent torsional stiffness for the MWCNT. Otherwise, if every wall of the MWCNT is moved at the same angular rate, than the MWCNT may be modeled for small deformations as a group of coaxial SWCNTs in parallel.

2.2.5 Affect of Chirality on Mechanical Properties

To this point little attention has been paid to the affect of chirality on CNT mechanical properties. There is good reason for this as Lu has found that the tensile modulus of elasticity was insensitive to tube diameter and chirality [48]. In contrast, Chang, Geng, and Guo found a

relation between chirality and elastic modulus, however, they found that chirality effects only were significant for SWCNTs with diameters less than 0.5 nm [69]. Mori et al. used *ab initio* simulations to come to a similar result as Lu, however, they found that the failure tensile strain is highly dependant on chirality [70]. This makes physical sense because a zig-zag tube will have some of its bonds oriented parallel to the axis of the tube (see Fig, 2.3(a)), meaning that any axial strain on the tube is exactly the axial strain on those bonds. An armchair tube has no bonds aligned with the tube axis, meaning the atomic structure tends to attenuate tube axial strain for each individual bond, allowing the armchair tube to be stretched further than the zig-zag tube before failure.

Chapter 3

Modeling Nano-scale Compliant Mechanisms

In order to be able to design a nCM with CNT-based flexural components it is necessary to develop models for their kinematic and elastomechanic behavior. Unfortunately, traditional continuum mechanics based macro-scale modeling tools such as FEA are incapable of capturing nano-scale phenomena such as van der Waals forces in their predictions of CNT deformation. Thus, it is necessary to use molecular simulation to predict the behavior of CNT-based flexures. This chapter will offer a brief introduction to molecular simulation with an emphasis on molecular mechanics and dynamics, which will be used to simulate a CNT-based PGM in Chapter 4. This chapter than ends with a discussion of the psuedo-rigid-body model, which is one of the primary tools used by precision engineers for modeling large-scale deformations of compliant mechanisms.

3.1 Molecular Simulation

At the macro and micro-scales the tool most often used by engineers is finite element analysis (FEA). In FEA, a structure is represented by a series of volumetric elements and the location of the nodes of these elements is tracked during the deformation of the structure according to macroscopic material laws and constitutive relations. Traditional FEA approaches are inadequate for describing the deformation that occurs in a CNT undergoing strain. As the CNT is deformed, the atoms become more closely packed, producing a van der Waals atomic interaction that is not captured by FEA software. FEA software would require the designer to pick an equivalent Young's Modulus, E, and moment of inertia, I, for the CNT. As shown in Chapter 2, a standardized value of these properties has not been agreed upon in the literature. As a result of these shortcomings in FEA, it is necessary to use a different modeling approach such

as molecular simulation in order to simulate the deformation of a CNT four-bar compliant mechanism.

3.1.1 *Ab Initio* Simulation

Ab initio (Latin for "from first principles") methods are the most comprehensive and accurate ways to simulate the dynamics of an atomic system. This particular type of molecular simulation uses quantum physics to fully describe the behavior of matter at the molecular level by using a linear combination of parameters that refer to a basis set of electron orbitals of each atom in the system. The fundamental energy conservation law at the quantum level is given by the Schrodinger equation. Shown in Eq. 3.1, the time-independent Schrodinger equation, a simplification of the more general Schrodinger equation, relates the wavefunction of the particle, ψ, Planck's constant, h, and the mass of the particle, m, to the energy, E, and the potential energy of the particle, Π.

$$\frac{-h^2}{2m}\frac{\partial^2\Psi}{\partial x^2} + \Pi\Psi = \Phi\Psi \tag{3.1}$$

The wavefunction contains information about the position and distribution of the electron cloud for an atom. It may also be interpreted as a way of determining the probability of finding the particle at a particular spatial coordinate at a particular time. In the time invariant case, Φ is the total energy of the particle, while Π is the potential applied to the particle. The first term on the left-hand side of Eq. 3.1 is physically interpreted as the kinetic energy of the particle.

In theory a*b initio* calculations may be used to solve any quantum system, however, the equations are so complex that when used in practice the method must incorporate many assumptions in order to allow the system to have a solution. The first approximation made in an *ab initio* simulation is that the motions of an electron for an individual atom may be decoupled from the motions of the nucleus of that atom. This assumption, the Born-Oppenheimer approximation, allows the Schrodinger equation to be applied to each electron of every atom in the system. This approximation allows a particular solution to be found for the electron potential energy contained in the system.

After this calculation is performed, the potential energy associated with the locations of every nucleus in the system is found. The wavefunction for the particular system topology is then calculated, and a unique total energy for the system is found. By iteratively moving the location of each nuclei in small increments the total system energy is minimized, thus producing

the final system configuration. In practice this iterative solution is accomplished by implementing a method such as Hartee-Fock, local density approximation (LDA), or the tight-binding approximation (TB). All of these methods are extremely computationally expensive, often taking weeks to months to complete. In order to gain useful data over the course of a few weeks, system sizes must not exceed more than a few hundred atoms. This limits the possible use of *ab initio* methods not useful for modeling of CNT-based devices, as a design engineer may go through several design iterations in order to optimize the performance of an nCM and does not usually have months to complete the design.

3.1.2 Space Frame Simulation

It is possible to envision a SWCNT as a collection of pivots (atoms) and trusses (atomic bonds). In the mechanical engineering community this type of modeling is known as a space frame. In it the atomic bonds of the SWCNT become replaced with truss elements that are connected to atoms that act as pin joints, allowing relative rotation of each truss member. Each truss has an axial, bending, and torsional stiffness, referred to respectively as k_{axial}, $k_{bending}$, and $k_{torsional}$, as well as a bond cross-sectional area, A_{bond}, moment of inertia, I_{bond}, and polar moment of inertia, J_{bond}. The values for each of these parameters seem to have been agreed upon in the literature and are presented in Table 3.1.

Table 3.1: Elastic properties of the space frame.

A_{bond} (Å^2)	I_{bond} (Å^4)	J_{bond} (Å^4)	k_{axial} (kcal/mol· Å^2)	$k_{bending}$ (kcal/mol· rad^2)	$k_{torsion}$ (kcal/mol· rad^2)	Ref
1.688	0.277	0.453	938	126	40	[39,46,49]

Based on these three fundamental stiffnesses a local elemental stiffness matrix, $\mathbf{k_e}$, is then be defined for the elemental truss with end nodes *i* and *j*. The elemental stiffness matrix links the six degrees of freedom of each node (three translational and three rotational) to the corresponding forces and moments on each node. Each individual truss elemental stiffness matrix is then assembled into a global stiffness matrix, which links all of the global displacements to all of the global forces. The solution of such an equation is well known in linear algebra provided that a correct number of boundary conditions have been placed on space frame. Once solved, the space frame model will tell the location of each atom in the deformed CNT in response to the imposed boundary conditions.

The simplicity of the space frame model allows for easy visualization of the deformation of a CNT. Furthermore, the space frame allows the affects of chirality on elastomechanic behavior to enter into the simulation. The method does, however, have some shortcomings due to its simple treatment of bonded interactions. Since a bond cannot "bend" as a truss would in the macro-scale material sense, space frame models tend to underestimate the energy resulting from bond angle deformation. The space frame also does not easily allow for non-bonded interactions such as van der Waals. While some models have alleviated this problem by adding trusses between neighboring non-bonded atoms, it should be noted that defining a stiffness for this class of truss is not trivial because the van der Waals interaction stiffness is highly nonlinear with respect to atomic separation. Finally, the linear spring approximations of each atomic bond are valid only for small-deformations, as the bond stiffness is non-linear at large strains.

3.1.3 Finite Element Simulation

Effort has been given to modeling CNTs as cylindrical shells that are then simulated via the finite element method (FEM). In FEM, the cylindrical shell is discretized into a number of small elements, forming a solid mesh. Once the boundary conditions are applied to the model, the nodes of each element are tracked in response to system loading. This type of simulation therefore provides dynamic and static information about a system with solution times that tend to be shorter than those of *ab initio* methods.

While this type of simulation method is accurate for describing the elastomechanic behavior of macro-scale materials, FEM proves to be challenging to apply to nano-scale materials such as CNTs. One of the biggest problems is that FEM requires a thickness of the CNT wall to be set. As discussed in Chapter 2, this choice is not a trivial matter and there is no agreed upon value in the literature. Also, while the literature has shown that it is possible to obtain accurate results compared with molecular dynamics simulation [60], the FEM is incapable of capturing the affect of chirality on CNT deformation. This is because the FEM completely neglects the atomic structure of the CNT, instead applying bulk mechanical properties to the wall of the tube. Furthermore, it is unknown at this time if FEM is applicable for SWCNTs less than 0.5 nm in diameter, as the thickness of the shell approaches the same order of magnitude as the radius of the CNT, thus invalidating the shell approximation of the CNT.

3.1.4 Molecular Mechanics and Dynamics Simulations

Molecular mechanics (MM) and dynamics (MD) models represent the CNT as a collection of balls (atoms) and springs (atomic bonds). Each atom has a mass associated with it as well as a number of potential energies associated with bonded and non-bonded interactions to its neighboring atoms. The sum of all of these potential energies for every atom in the system are combined to represent the total system energy, U_{total}, which is then minimized by changing the length and orientation of each individual bond in response to system loading and boundary conditions. The relationship between the applied potential, $\prod$, and the mass, m, and position, r, of each atom is expressed with a form of the Cauchy momentum equation, as shown in Eq. 3.2.

$$m\frac{d^2r}{dt^2} = -\nabla\Pi \tag{3.2}$$

In a MM simulation the mass of the system is neglected, meaning the gradient of the potential must be equal to zero. The locations of the atoms within the wall of the CNT are prescribed a displacement pattern, and then Eq. 3.2 is solved. The system continues to be solved iteratively until all the atoms in the system have been moved into a configuration which minimizes the system's total energy with respect to the prescribed boundary conditions. MD simulations are solved in a similar manner except that the velocities of each atom must be accounted for during each iteration and contribute to the overall system energy minimization.

The application of MM and MD models to a system represents one of the most accurate ways to describe an atomic system short of using *ab initio* methods. These methods are also capable of handling simulations involving large numbers of atoms, allowing more complicated systems to be modeled than *ab initio* methods. The MM and MD models incorporate the affect of chirality on CNT deformation because information about the starting orientation of the atoms is not lost as in FEM. MM and MD simulations the best candidates for simulating the performance of CNTs as flexural elements in a nCM because of their ability to accurately simulate complex dynamic systems in a relatively short period of time when compared with *ab initio* simulation.

The backbone of any MM/MD software package is a force field, which prescribes the fundamental constants as well as the functional forms of the potential for every possible type of atomic interaction as well as every possible atom type. The molecular modeling program used in the simulations presented in Chapter 4, HyperChem®, utilizes the MM+ force field which is an

extension of the popular MM2™ force field [71,72]. As shown in Eq. 3.3, the total system energy is a summation of energy contributions from different atomic interactions, where the subscripts refer to the contributions due to bond stretching (axial deformation), in-plane bond deformation (in-plane bending), out-of-plane bond deformation (out-of-plane bending), dihedral bond deformation (axial bond rotation), van der Waals interaction, and Coulombic interaction.

$$U_{total} = \sum U_{strech} + \sum U_{in-plane} + \sum U_{stretch-bend} + \sum U_{out-of-plane} + \sum U_{dihedral} + \sum U_{vdW} + \sum U_{Coulombic} \quad (3.3)$$

The equations for each term in Eq. 3.3 and the corresponding parameters for aromatic C-C bonds will be presented in the remainder of this section.

The energy due to bond stretching, $U_{stretch}$, for two atoms separated by a distance l is based on Hooke's Law and includes a bond stiffness, k_s, and bond rest length, l_o, as shown in Eq. 3.4.

$$U_{stretch} = \frac{1}{2} k_s (l - l_o)^2 (1 + CS(l - l_o)) \quad (3.4)$$

The stiffness coefficient for bond stretching, k_s, has a value of 580.20 kcal/mol·Å^2, and the bond rest length, l_o, is 1.42 Å. The constant *CS* is a scaling factor for the quadratic force correction factor and has a value of -2.

The potential energy contribution from in-plane and out-of-plane bond bending, U_{bend}, is found in a similar manner as above by substituting an equilibrium bond angle and bond bending stiffness for their Cartesian counterparts. The final expression, shown in Eq. 3.5, also includes a sextic bending term that is controlled by a scaling factor, SF, equal to 7x10^{-8}.

$$U_{bend} = \frac{1}{2} k_b (\theta - \theta_o)^2 \left(1 + SF(\theta - \theta_o)^4\right) \quad (3.5)$$

For in-plane bond bending the bending stiffness coefficient, k_b, is equal to 0.01885 kcal/mol·deg^2 and the equilibrium bond angle, θ_o, is 120^o. For out-of-plane deformations the bond stiffness coefficient, k_b, is equal to 0.00219 kcal/mol·deg^2 and the equilibrium bond angle, θ_o, is 0^o.

In order to more accurately simulate the atomic system MM and MD methods routinely employ a term that represents the coupling effect between bond bending and bond stretching. The MM+ field includes this coupling in the total system energy via the use of a Urey-Bradley type stretch-bend term. The stretch-bend energy correction, $U_{stretch\text{-}bend}$, is calculated using the relationship shown in Eq. 3.6.

$$U_{stretch-bend} = k_{sb}(\theta - \theta_o)\left[(r - r_o)_{bond\,1} + (r - r_o)_{bond\,2}\right] \quad (3.6)$$

Unfortunately, the values for these constants used in the simulations to be presented in Chapter 4 are proprietary and are not readily accessible to be listed here.

The potential energy due to the dihedral terms, $U_{dihedral}$, is represented by a truncated Fourier series. The final expression, shown in Eq. 3.7, relates a dihedral force constant, V_i (i is the Fourier order), to the dihedral angle, ϕ, which is the relative rotation of the two atoms about the axis of the bond.

$$U_{dihedral} = \frac{V_1}{2}(1+\cos\phi)+\frac{V_2}{2}(1-\cos 2\phi) \tag{3.7}$$

The constant V_1 has a value of -0.930 kcal/mol and the constant V_2 has a value of 4.8 kcal/mol.

Van der Waals potentials are calculated using a hybrid version of the Lennard-Jones 6-12 function combined with an exponential decay function as presented in Eq. 3.8. The potential, U_{vdW}, measures the amount of non-bonded energy between two atoms separated by a distance r. The function itself is shaped by two constants that define the depth of the potential energy well, ξ, and the equilibrium distance between the two non-bonded atoms, r_o.

$$U_{vdW} = \xi\left[2.9\times10^5 e^{-12.5\left(\frac{r}{r_o}\right)} - 2.25\left(\frac{r_o}{r}\right)^6\right] \tag{3.8}$$

The potential well depth, ξ, has a value of 0.044 kcal/mol while the equilibrium distance, r_o, is 3.88 Å. It should be noted that a convention has been adopted such that a positive potential energy corresponds to a repulsive force (denoted by a negative sign) between two atoms.

Unfortunately, the non-bonded potential must undergo a change in definition when r is less than 1.17 Å. At this point the attractive r^{-6} term begins to dominate the repulsive exp(-r) term and the function becomes invalid. The MM+ force field thus imposes a new definition, as shown in Eq. 3.9, for the potential that uses the same constants as in Eq. 3.8 with an added scaling term to enforce continuity of the function at r = 1.17 Å.

$$U_{vdW} = 336.176\,\xi\left(\frac{r_o}{r}\right)^2 \qquad \text{for } r \le 1.17\text{Å} \tag{3.9}$$

As larger CNTs are used in the MM/MD simulations it is necessary to impose a distance cutoff on the non-bonded interactions in order to save computation time. The first type of cutoff that may be imposed is known as a shifting function, which imposes a piecewise function on the non-bonded potential. For distances greater than the cutoff distance, r_{outer}, U_{vdW} has a value of zero. For distances less than r_{outer}, the value of the potential function, U^*_{vdW} , is a product of a shifting function and the value of U_{vdW} from Eq. 3.8, as shown in Eq. 3.8.

$$U^*_{vdW} = U_{vdW}\left(1-2\frac{r^2}{r^2_{outer}}+\frac{r^4}{r^4_{outer}}\right) \qquad \text{for } r \le r_{outer} \tag{3.10}$$

The shifting function is not an ideal cutoff as it alters the value of the non-bonded potential function at distances near the equilibrium point r_o. A more accurate way to impose the cutoff condition is to use a switching function, which redefines the potential function of Eq. 3.8 only for distances between a prescribed r_{inner} and r_{outer}. Beyond r_{outer} the potential function is defined as zero, and before r_{inner} the potential function is the same as in Eq. 3.8. The redefined potential, U^*_{vdW}, is presented in Eq. 3.9.

$$U^*_{vdW} = U_{vdW} \frac{\left(r^2_{outer} - r^2\right)^2 \left(r^2_{outer} + 2r^2 - 3r^2_{inner}\right)}{\left(r^2_{outer} - r^2_{inner}\right)^3} \qquad \text{for } r_{inner} \le r \le r_{outer} \tag{3.11}$$

All simulations conducted in this thesis utilize the switching function to impose a cutoff on the van der Waals interactions.

Finally, the MM+ force field does not recognize a significant dipole moment from a carbon atom in the aromatic configuration. Therefore, the energy contribution from Coulombic interaction is negligible and is not included in the simulations of CNT deformations. It is also important to note that for MD calculations the simulation package considers the mass of a carbon atom to be 12 a.m.u. or 1.993×10^{-26} kg.

3.2 Psuedo-rigid-body Model for Compliant Mechanisms

As mentioned in section 3.1.4, MM and MD simulations are quite computationally expensive. In Chapter 4 we will learn it took nearly a month simulate the elastomechanic response of a single mechanism via MM simulation. As a result of the costly solution time required by the MM/MD model of a CNT-based flexure, it is obvious that a designer will not able to obtain useful kinematic and elastomechanic information about a flexure topology without investing months of computation time. Compounding this problem is the fact that a designer of compliant mechanisms often goes through dozens of concepts before choosing the final device topology, and once this decision is made, often device optimization will take several iterations. Therefore, this process could translate into months of development using MM/MD methods even though similar device topologies that would take only days to evaluate at the macro-scale. One way to get around the MM/MD modeling bottleneck would be to use current compliant mechanism modeling techniques to describe CNT-based flexures.

The psuedo-rigid-body model (PRBM) is a method for predicting the kinematic and elastomechanic behavior of CMs. The PRBM creates an equivalent rigid-link assembly for a

prescribed flexure topology. The main advantage of this type of modeling approach is that it allows well-known analysis methods for linkage assemblies to be used for predicting the behavior of CMs. In Fig. 3.1, a PGM containing two flexural elements and two rigid bars has been replaced with four rigid links connected via four pin joints. To simulate the stiffness of the flexural elements a torsional spring with stiffness K_{spring} is placed at each pin joint.

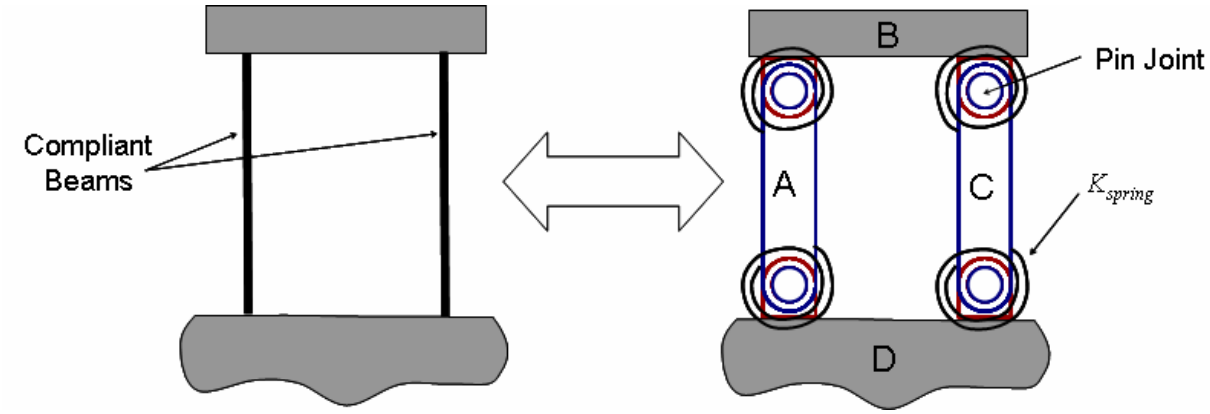

Figure 3.1: Four-bar flexure and its PRBM representation.

The kinematics of the rigid-body mechanism with rigid bars A, B, C, and D are governed by a vector loop equation as shown in Eq. 3.12 (note that $\hat{i}$, $\hat{j}$, and $\hat{k}$ are the principle directions of the global coordinate system).

$$\vec{A}+\vec{B}+\vec{C}+\vec{D}=0\hat{i}+0\hat{j}+0\hat{k} \tag{3.12}$$

The energy of the mechanism is then represented by the principle of virtual work as shown in Eq. 3.13.

$$\Sigma\int \vec{F}_{applied}\bullet d\vec{r}=\Sigma\int \vec{T}_{spring}\bullet d\theta_{spring}+\Sigma\int \vec{F}_{external}\bullet d\vec{r} \tag{3.13}$$

This above expression balances the applied work to actuate the CM with the internal work due to the deformation of the flexural components and external work due to boundary conditions on the CM.

With the governing equations for the kinematic and elastomechanic behavior of an arbitrary rigid-body topology laid out, it is time to look at how one would transform a CM into its rigid-body representation. Howell [1] has worked on modeling individual flexural components with different boundary conditions in order to make the PRBM accurately predict the response of a given flexure topology. Since the flexure to be studied in Chapter 4 is a specialized type of CM, a PGM, the remainder of this section will focus on the application of the PRBM to this particular topology. For more details on how to transform the flexural components

of other topologies the reader is encouraged to read Chapter 5 of Howell's textbook on compliant mechanisms [1].

The main building block of a PGM is two parallel flexural components that have a guided end condition imposed on one end, while the other end is grounded. As shown in Fig. 3.2 the fixed-guided compliant beam is replaced with a rigid bar connected to two pivots. The length of the rigid bar is found by multiplying a characteristic radius factor, γ, by the original length of the flexure, L. This means that the location of each pivot is located at a distance of $\frac{1}{2}(1-\gamma)L$ from each end of the flexural element, as shown in Fig. 3.2.

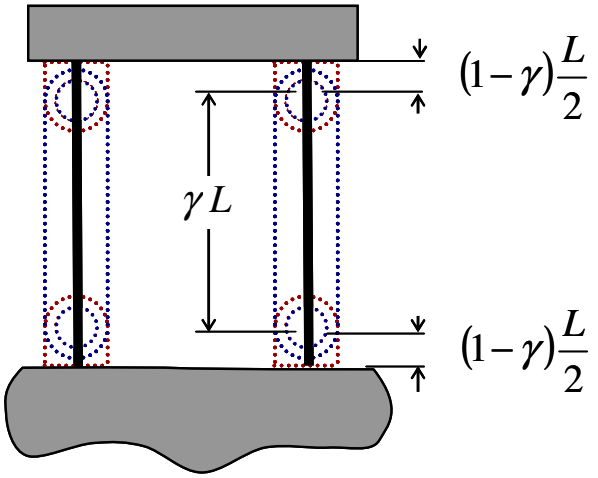

Figure 3.2: Placement of pivots according to characteristic radius factor.

Howell has shown that the value for the characteristic radius factor is a constant equal to 0.8517 for a rigid bar rotation of up to 64.3^{o} [1].

The value of the torsional spring constant is determined by the material and geometric properties of the flexure blade as well as a stiffness coefficient, K_{θ}, and the characteristic radius factor, as shown in Eq. 3.14.

$$K_{spring} = 2\frac{\gamma}{L}K_{\theta}EI \tag{3.14}$$

In Eq. 3.14 E represents the elastic modulus of the flexure blade while I represents the flexure's bending moment of inertia. We will see in Chapter 5 that care must be taken when prescribing values for E and I. The stiffness coefficient has only a weak dependence on material properties and loading condition, and therefore Howell suggests that it be taken as a constant with a value of 2.63 rad^{-1} for a cantilever beam with a guided end condition. It is important to note that the stiffness coefficient only impacts the elastomechanics of the CM in the PRBM. On the other hand, the characteristic radius factor is responsible for establishing the geometric location of the

pivots as well as determining the magnitude of the torsional spring constant, and it therefore appears in the kinematic and elastomechanic descriptions of the CM.

With the kinematic and elastomechanic scaling parameters defined, it now becomes necessary to solve Eq. 3.12 and Eq. 3.13 in order to model the PGM as a function of applied load and coupler bar translation. Figure 3.3 shows a diagram of the PRBM representation of a PGM. The diagram contains all the relevant parameters needed to describe the motion of the compliant PGM during its deformation. The pin joints are labeled 1 through 4 in a clockwise manner starting from the bottom left corner of the mechanism. The origin of the global coordinate system is located at pin 1. Each pin joint is allowed to exert a torque, denoted T_i (i is the index representing the specific pin joint), on the structure via torsional springs as described above. The length of each bar is designated as a length r_i, where the subscript i refers to the appropriate bar labeled in Fig. 3.1 (1=A, 2=B, etc.).

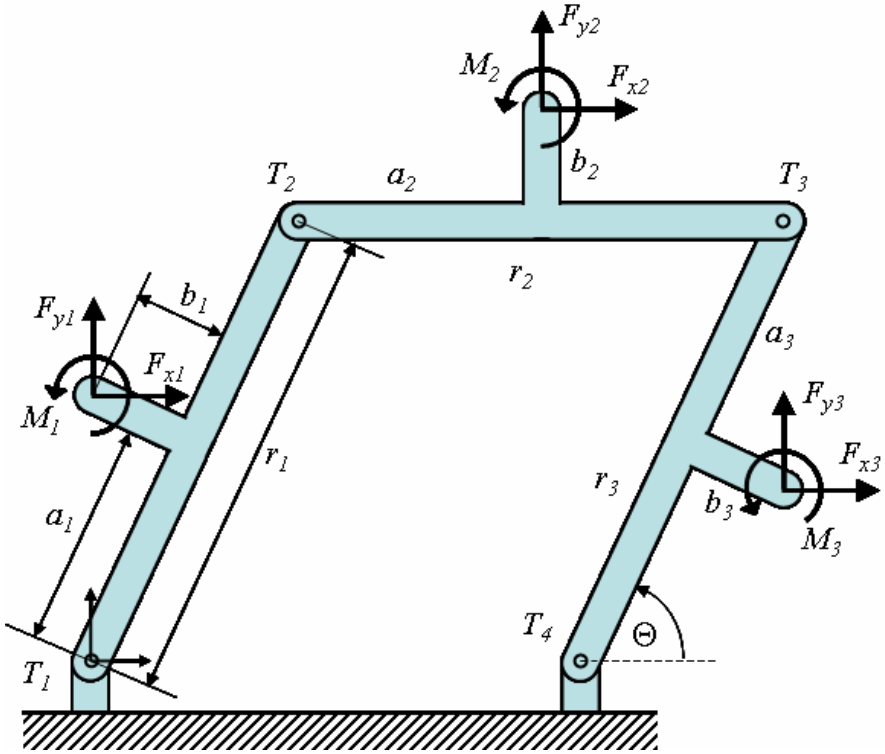

Figure 3.3: Geometry parameters that define the PRBM representation of a PGM[1].

[1] Figure 3.3 with permission from L.L. Howell Compliant Mechanisms, © 2007 Wiley Interscience. Reprinted with permission from John H. Wiley and Sons, Inc.

Forces applied to each bar in the x and y directions are denoted F_{xi} and F_{yi} respectively, while moments on each bar are denoted by M_i. These loads may be placed on each bar at a distance a_i along each bar as well as a distance b_i perpendicular to each bar. The angle that bars A and C make with the horizontal is denoted by Θ (measured in radians). For a generalized model of a PGM [73] it is possible to rewrite Eq. 3.12 using the parameters listed above. For a PGM that lies in the x-y plane the coordinates of any point P on the coupler bar (originally located at (x_o, y_o) measured with respect to the global coordinate system) in the deformed PGM configuration, denoted by (x_P, y_P), is found by using Eq. 3.15 and Eq. 3.16.

$$x_P = \gamma L \cos\Theta + x_0 \tag{3.15}$$

$$y_P = \gamma L(\sin\Theta - 1) + y_0 \tag{3.16}$$

It should be noted that Eq. 3.15 and Eq. 3.16 express the position of a point in the compliant PGM, not its rigid-body representation.

It is also possible to rewrite Eq. 3.13 using the same parameters shown in Fig. 3.3, as shown in Eq. 3.17 [1].

$$\begin{aligned}&\left[F_{x1}b_1 + F_{y1}a_1 + F_{x3}b_3 + F_{y3}a_3 + r_1\left(F_{y2} + F_{y3}\right)\right]\cos\Theta \\ &\quad -\left[F_{x1}a_1 + F_{y1}b_1 + F_{x3}a_3 + F_{y3}b_3 + r_1\left(F_{x2} + F_{x3}\right)\right]\sin\Theta + M_1 + M_3 + T_1 + T_2 + T_3 + T_4 = 0\end{aligned} \tag{3.17}$$

Each pin joint torque is defined by the spring constant from Eq. 3.14 and a reference angle Θ_o as defined using Eq. 3.18 [1].

$$T_i = -K_{spring}\left(\Theta - \Theta_o\right) \tag{3.18}$$

For the special case when the PGM is loaded only by two horizontal forces located at each end of the coupler bar, Eq. 3.17 may be rewritten as shown in Eq. 3.19. Note that in Eq. 3.19 the undeformed PGM reference angle has been assumed to be 90^o.

$$\left(F_{x1} + F_{x3}\right)\gamma L\sin\Theta = 2K_{spring}\left(\pi - 2\Theta\right) \tag{3.19}$$

When an equal horizontal load of magnitude $\frac{1}{2}F$ is applied to each end of the coupler bar, Eq. 3.19 may be rewritten as shown in Eq. 3.20.

$$F = \frac{2K_{spring}\left(\pi - 2\Theta\right)}{\gamma L\sin\Theta} \tag{3.20}$$

In Eq. 3.20 F, the total load applied to the coupler bar, is related to the single degree of freedom in the system, Θ. Chapter 4 will use the non-linear function in Eq. 3.20 to link the applied force to the deformation of the compliant PGM.

The PRBM model begins to kinematically and elastomechanically deviate from FEA results of CMs by more than 10% when the deflections become large, i.e. approximately greater

than 50^{o} rigid beam bending [1]. The reason for this deviation is traced back to geometric and material non-linearity at high device strain. Howell has dealt with this by making the PRBM constants functions of the deflection of the CM [1]. As a result of the reported success of the PRBM for quickly and accurately predicting small and large-strain behavior in PGMs [73] the PRBM will be applied to a CNT-based nPGM in Chapter 5. We will see that the most important part of the process will be determining the values of the two PRBM parameters, K_θ and γ, as the PRBM is sensitive to these kinematic (γ) and elastomechanic (K_θ and γ) parameters.

Chapter 4

Parallel Guiding Mechanism Simulation

As discussed in Chapter 1, compliant PGMs are a ubiquitous component in many macro- and micro-scale precision devices. If a CNT-based nPGM could be constructed then it would be possible to construct numerous types of complex nCMs, allowing some of the most useful nano-scale devices to finally be realized. Chapter 3 discussed the need to simulate the kinematic and elastomechanic performance of a CNT-based nPGM through MM and MD methods. This chapter will discuss the model used in these simulations as well as present the kinematic and elastomechanic results obtained from the studies.

4.1 Molecular Model Used in the Simulations

Two types of modeling approaches were used in simulating the CNT-based nPGM: MM and MD methods. Fortunately, the same molecular model of a nPGM may be used for both studies. The model, shown in Fig. 4.1, consists of two defect-free SWCNTs that are oriented vertically and parallel to each other. Note the global coordinate system is located at the center of the base of the left-most SWCNT, with the *y*-axis located on the axis of the SWCNT and the *x*-axis pointing towards the right-most SWCNT. The SWCNTs are of (5,5) orientation and are 9 nm tall. Note that this height includes a cap that is placed at the end of the SWCNT. The cap is an artifact of the initial geometry optimization of each SWCNT as the presence of the cap tends to speed up the time required to geometrically optimize a defect-free (5,5) SWCNT. The SWCNTs are spaced 7.64 nm apart from each other, thus establishing a length for the coupler bar. The bottom row of atoms in each SWCNT is grounded translationally and rotationally. This boundary condition assumes that the SWCNTs are perfectly grounded to their substrate. This is an idealized assumption because real substrate bonds will have some stiffness associated

with them, it provides a baseline for future study on the affect of substrate-CNT interface stiffness on the performance of a nCM.

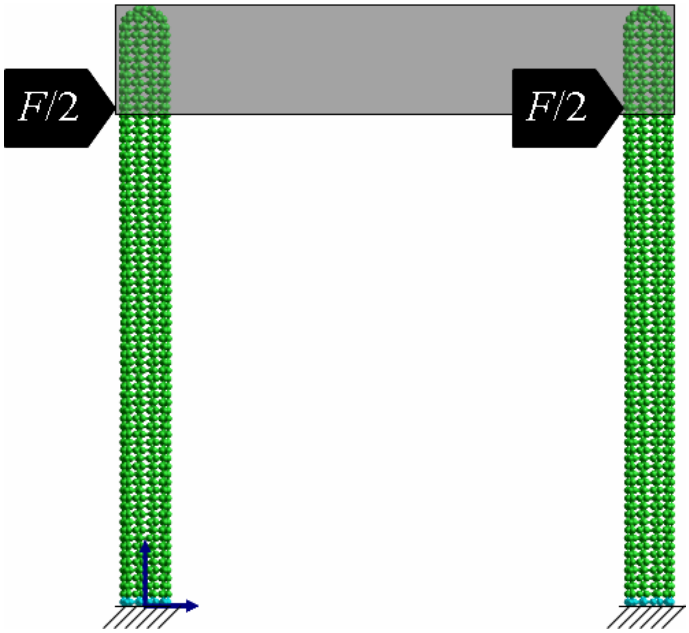

Figure 4.1: MM/MD model of CNT-based nPGM.

The top of each SWCNT has a set of distance constraints imposed on it in order to simulate the presence of a coupler bar, shown as a transparent rectangle in Fig. 4.1. It should be noted that the coupler bar is considered to be infinitely rigid, again an idealized assumption, so as to serve as a baseline study for the performance of a CNT-based nPGM.

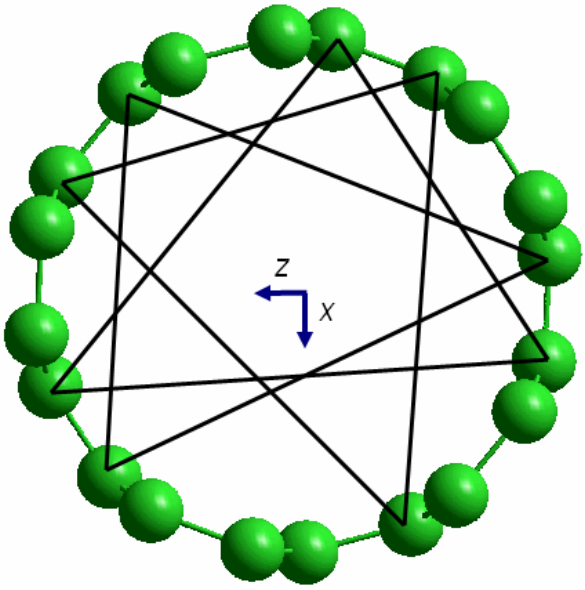

Figure 4.2: Constraints placed on the SWCNT cross-section.

The first set of distance constraints is applied to a cross-section of atoms in each nanotube located 8.61 nm from the base of the nanotube and keeps the end of the SWCNT from collapsing immediately upon loading. Figure 4.2 shows the pattern of distance constraints applied to the cross-section. The dark lines connecting pairs of atoms represent a distance constraint that cannot change length. This boundary condition on each cross-section serves two purposes: 1) it assumes that the top of each SWCNT is bonded in such a way that the cross-section of the bonded portion cannot be deformed and 2) it establishes the length of the compliant members of the nPGM as 7.64 nm.

The final sets of distance constraints are used to form the coupler bar. The ideal constraint we would like to impose is that the tops of each SWCNT move in unison. The way this is done is to enforce three types of distance constraints from one tube to the other. Figure 4.3 shows the distance constraints (types A, B, and C) placed on the MM/MD model.

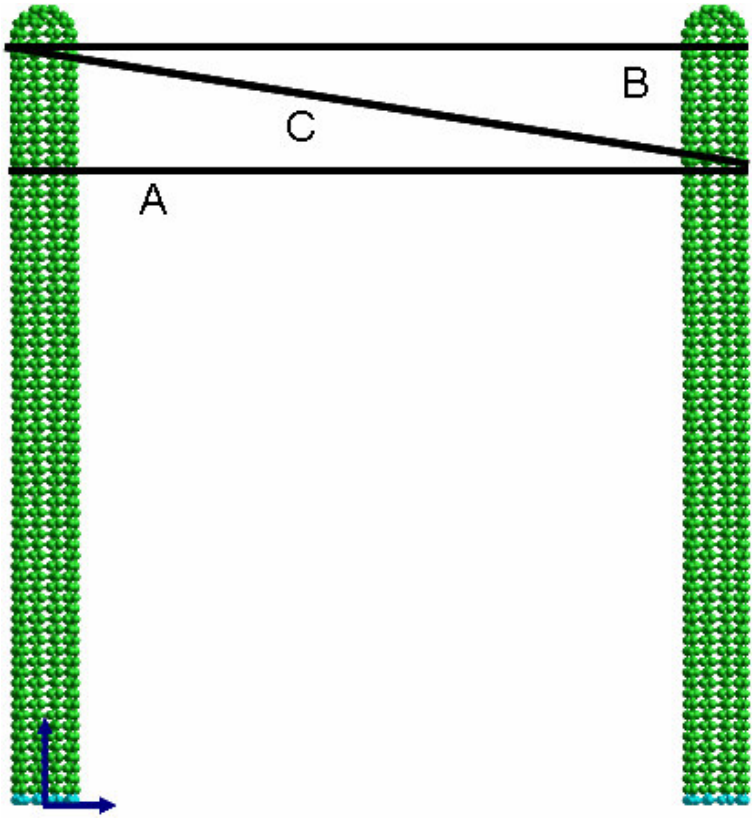

Figure 4.3: Constraints placed on the SWCNT to form the coupler bar.

Type A constraints occur on the cross-section of atoms located at 7.64 nm from the base of the SWCNT. They connect each atom in the left SWCNT to its corresponding atom on the right SWCNT, i.e. the atom at the 12 o'clock position on the left CNT is connected to the atom at the

12 o'clock position on the right CNT, via a distance constraint that cannot change length. Type B constraints are exactly the same as type A constraints except they occur at the cross-section of atoms located 8.61 nm from the bottom of each CNT. Finally, type C constraints are used to stop relative motion between the type A and B constraints. They connect the atoms used in the type B constraints on the left SWCNT with the atoms used in the type A constraints on the right SWCNT with a distance constraint that cannot change length. The pairing of atoms is done in a similar fashion as in the previous constraints, with the 12 o'clock atom in the 8.61 nm high cross-section of the left SWCNT being constrained to the 12 o'clock atom in the 7.64 nm high cross-section of the right SWCNT. It should be noted that each cross-section includes 10 atoms (as shown in Fig. 4.2), meaning that type A, B, and C constraints each have 10 individual pairs of constraints.

While each capped SWCNT contains 750 atoms the distance constraints imposed on the capped end of each CNT to simulate the presence of a coupler bar effectively shorten the length of the SWCNT. The final nPGM model assumes the length of the SWCNT to be 7.64 nm and includes only 640 atoms per tube. Table 4.1 lists the important model parameters for the simulated nPGM.

Table 4.1: Parameters that define the nPGM model.

Flexure Length (L)	7.64 nm
Coupler Bar Length	7.64 nm
Nominal tube diameter (d_{cnt})	0.678 nm
Atoms per tube	640 atoms
SWCNT Chirality	(5,5)

A load of magnitude *½F* was prescribed to each CNT via a spring tether as shown in Fig. 4.1. Spring tethers place a bond, which is defined via a linear spring constant k_{tether}, between a point in space, located at (x_o,y_o,z_o), and an individual atom, located at (x,y,z). By prescribing the tether spring constant a potential is added to the system as shown in Eq. 4.1.

$$U_{tether} = k_{tether}\left[(x-x_o)^2+(y-y_o)^2+(z-z_o)^2\right] \tag{4.1}$$

The force exerted by a tether, $\vec{F}_{tether}$, on an individual atom is calculated in the Hyperchem® environment as shown in Eq. 4.2.

$$\vec{F}_{tether} = 2k_{tether}[(x-x_o)+(y-y_o)+(z-z_o)] \tag{4.2}$$

Each carbon atom in the cross-section located a distance 7.64 nm from the bottom of the SWCNT was prescribed a tether. This means each SWCNT has a force prescribed on ten atoms located at the base of the coupler bar, which is 7.64 nm from the base of the SWCNT. Each SWCNT was given an individual tether point: the left SWCNT was tethered to a point in space located at (764 nm, 0 , 0) while the right SWCNT was tethered to a point located at (771.64 nm, 0, 0). It is important to mention that there is a parasitic error induced by tethering the atoms to points in space at a height y_o = 0. However, in the worst case this parasitic vertical force accounts for a maximum of 1% of the total applied force. As the simulation continues, the coupler bar will translate downward, thereby minimizing the parasitic vertical error force. Since the maximum parasitic force of 1% of the total applied force occurs at the beginning of the simulation, i.e. when the load is small, and only gets smaller as the load is increased, we will therefore assume that the applied tether force is purely horizontal. Note that during the simulations each tethered atom was prescribed the same value of k_{tether}.

The equations and relevant parameters for each of the terms that contribute to the total MM/MD system energy are presented in section 3.1.4. MM simulations were carried out statically, meaning that the load was first incrementally increased by increasing the value of k_{tether} for each tethered atom by the same amount and then the model's total energy was minimized. Once a maximum load was applied, the load was then incrementally decreased in a similar manner until the nPGM was brought back to a no-load configuration. Each force increment was energy minimized using the Polak-Ribiere conjugate gradient algorithm until the total RMS energy gradient was less than 1 cal/Å·mol (0.07 pN). A switching function was imposed on the van der Waals function between 1 and 1.4 nm of atomic separation. These static MM simulations typically took five days to minimize per force increment. MD simulations of the nPGM were carried out over 240 ps using step increments of 1 fs. Note that the convergence criterion used for the MD energy gradient was the same as in the MM simulations, 1 cal/Å·mol.

The MM/MD simulations were set to run at a constant temperature that is infinitesimally larger than 0°K with a bath relaxation constant of 0.1 ps. While this simulated temperature does not mimic realistic operating conditions, it is necessary to do this in order to establish a baseline of performance for the nPGM as a room temperature study would induce too many thermal vibration modes into the structure and thus hide the basic operating behavior of the nPGM.

While the energy of the vibrations in the free-standing CNTs is known to increase linearly with temperature [74], some work has been done to determine the quantify the amplitude of vibration. Chen and Gao performed simulations on a free-standing (5,5) SWCNT with 1040 atoms and found that at 800 K, the lateral displacement of the nanotube was on the order of 0.2 nm, which is 30% of the diameter of the CNT, while the axial contraction of the tube was 0.04 nm, which is 0.3% of the axial length [75]. For further information on CNT vibrational modes one should consult the textbook written by Reich, Thomsen, and Maultzsch [74].

4.2 Simulation Results

The MM/MD simulations carried out on the CNT-based nPGM were meant to capture kinematic and elastomechanic behavior. This is important because no simulation found in the literature has attempted to capture the behavior of a SWCNT with a guided end condition, let alone the response of a nPGM. These simulation results are therefore the first of their kind, revealing information about the behavior of SWCNTs under a fundamentally different type of loading scenario than previously reported in the literature. These results represent the foundation for new research into the behavior of CNT-based nCMs.

4.2.1 Simulated Kinematics

It is unknown whether or not SWCNT-based nCMs will behave like their macro- and micro-scale counterparts. It is thus important to look at the kinematics and elastomechanics separately for the nPGM described in section 4.1 in order to understand if CNT-based nPGMs act like their macro- and micro-scale counterparts. The simulations reveal a mechanism that possesses three regions of behavior defined by the presence of buckling events. Figure 4.4 shows two of the three main regions of behavior. In region I deformation, no buckling events are present and each SWCNT appears to emulate the deformation pattern one would expect for a macro-scale beam in bending subject to a guided end condition. In region II deformation, each SWCNT has developed two kinks as a result of buckling events. As we will see in the following sections the behavior of region II is quite different from that of region I. The third region of behavior is a transition region which exists between region I and region II.

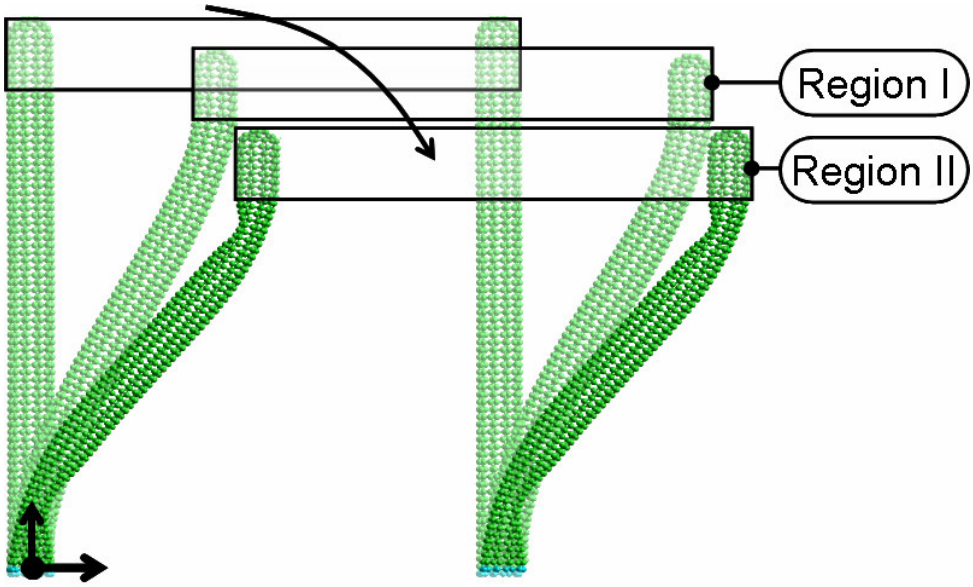

Figure 4.4: Coupler bar centroid translation.

In this region, buckling events in each SWCNT begin to occur, leading to the formation of kinks in each SWCNT in the order shown in Fig. 4.5. Note that during unloading the kinks revert back to their undeformed cross-sections in the reverse order in which they were formed.

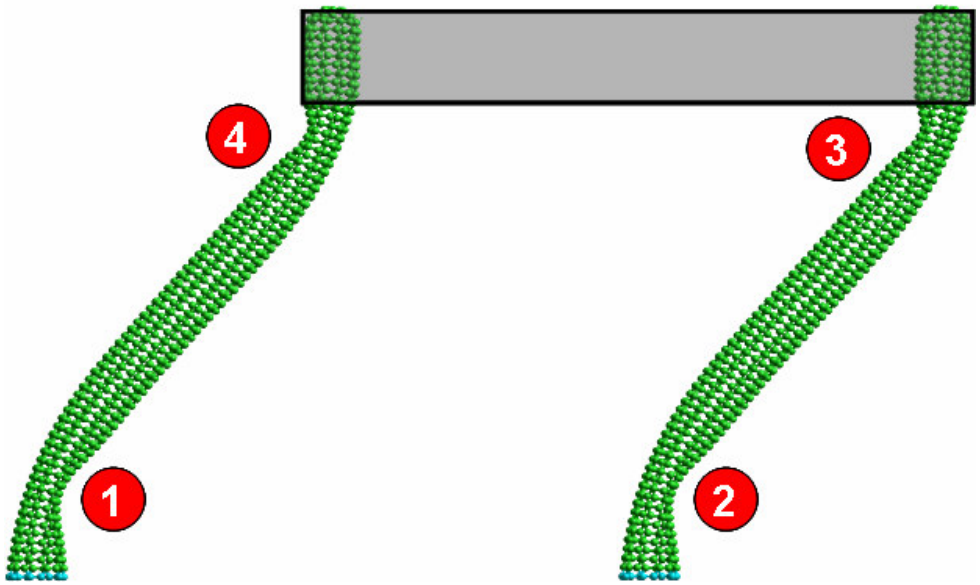

Figure 4.5: Order of kink formation in the transition region.

Figure 4.6 shows a plot of the translation of the coupler bar centroid with coordinates x_c and y_c measured relative to the original location of the centroid (3.82 nm, 7.64 nm) in the undeformed nPGM configuration. This translational data is included in Appendix A. The unshaded circles represent the path of the coupler centroid as the load is incrementally increased.

During region I behavior the centroid follows the path from A to B. When the load is infinitesimally increased from point B the first two kinks develop and the device snaps through 0.77 nm to point C, marking the beginning of the transition region. The transition region ends at point D with the development of the fourth kink, thus marking the beginning of region II behavior. The nPGM is further loaded to point E. The shaded circles represent the path of the centroid during incremental unloading. As the model is incrementally unloaded from point E the centroid appears to trace the same path formed by the loading simulations. However, instead of entering the transition region at point D as in the forward loading, the transition instead happens at a lower device stroke (4.20 nm instead of 4.70 nm). Further complicating matters is that the mechanism does not transition to region I from point C to point B as in the loading case, but rather from point F to point G.

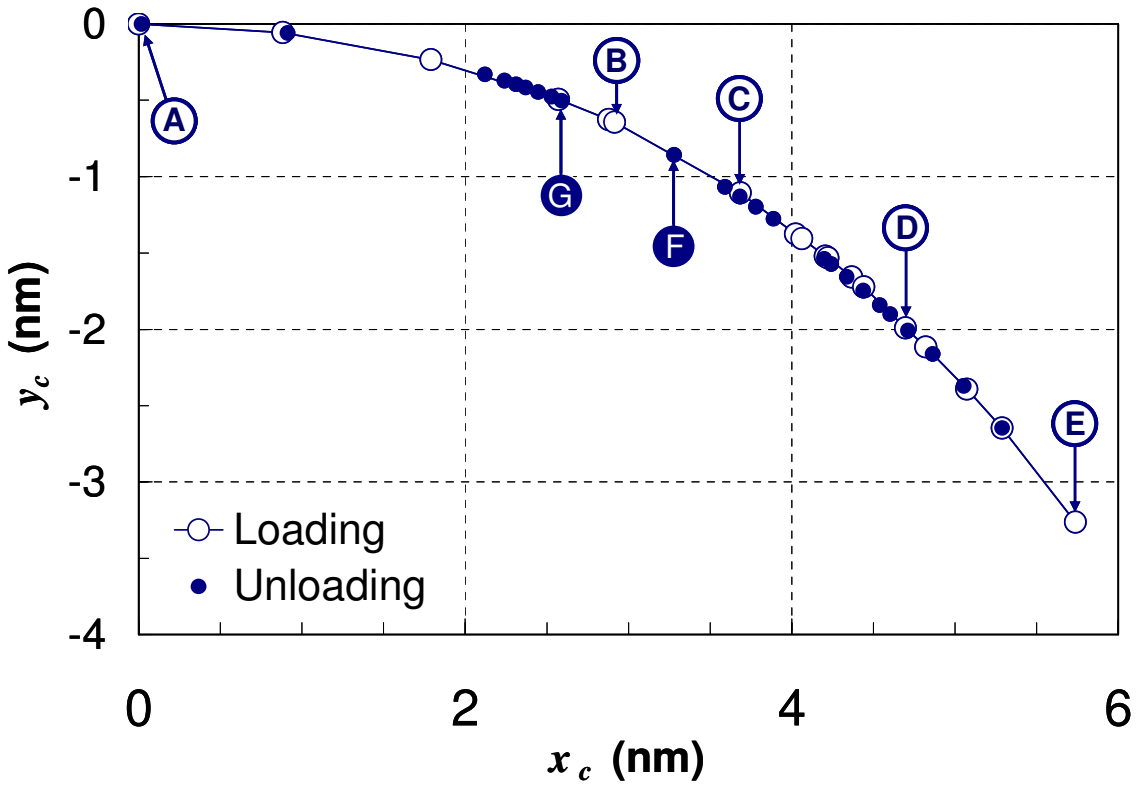

Figure 4.6: Coupler bar centroid translation.

Ultimately the unloaded device comes back to its original state at point A, indicating the nPGM was elastic over this entire loading range. There is an error of 0.01 nm between the loading and unloading simulations due to bond rotation in the caps of the SWCNT. These results indicate

that the nPGM's behavior is direction-dependant, a phenomenon not normally found, or desired, in macro-scale CMs. Table 4.2 lists the centroid locations for each of the points of interest.

It is interesting to note that even in the presence of four separate buckling events the coupler bar appears to follow a continuous path over its 5.74 nm stroke, which is 75% of the length of the device. However, some of these states would be unattainable with a force based actuator, as the buckling events make the coupler bar snap-through certain regions in the centroid trajectory. This seems to indicate that a displacement based actuator would be necessary to actuate the device, or that the device should only be operated in region I. The kinematic trajectory of the coupler bar is an arcuate path due to the parasitic vertical motion of the coupler bar which resembles that of macro-scale CMs. The parasitic error is less than 10% of the device height throughout region I. At point E the curvature is less than 0.76 nm, which is the critical curvature for defect generation given by [60], and the longest bond is 0.16 nm, well below bond failure criterion quoted in [41].

Table 4.2: Coupler bar locations at points of interest during loading/unloading of the nPGM.

Point	x_c (nm)	y_c (nm)
A	0.00	0.00
B	2.92	-0.64
C	3.69	-1.11
D	4.70	-1.99
E	5.74	-3.26
F	3.28	-0.86
G	2.59	-0.50

It is well known in the CM community that a PGM will have a parasitic rotational error, θ_p, associated with the coupler bar if it is not actuated at the center of stiffness [76,77]. Figure 4.7 shows the parasitic error in the coupler bar as a function of the x-displacement of the coupler bar centroid. The rotation data for the nPGM is provided in Appendix A. We see that the coupler bar rotation never gets larger than 4^o for the entire stroke of the device. Small angle approximations may be used to show that the rotation discontinuities would produce a worst–case jump in x and y positions of 0.3 pm and 16.7 pm respectively for the coupler bar centroid.

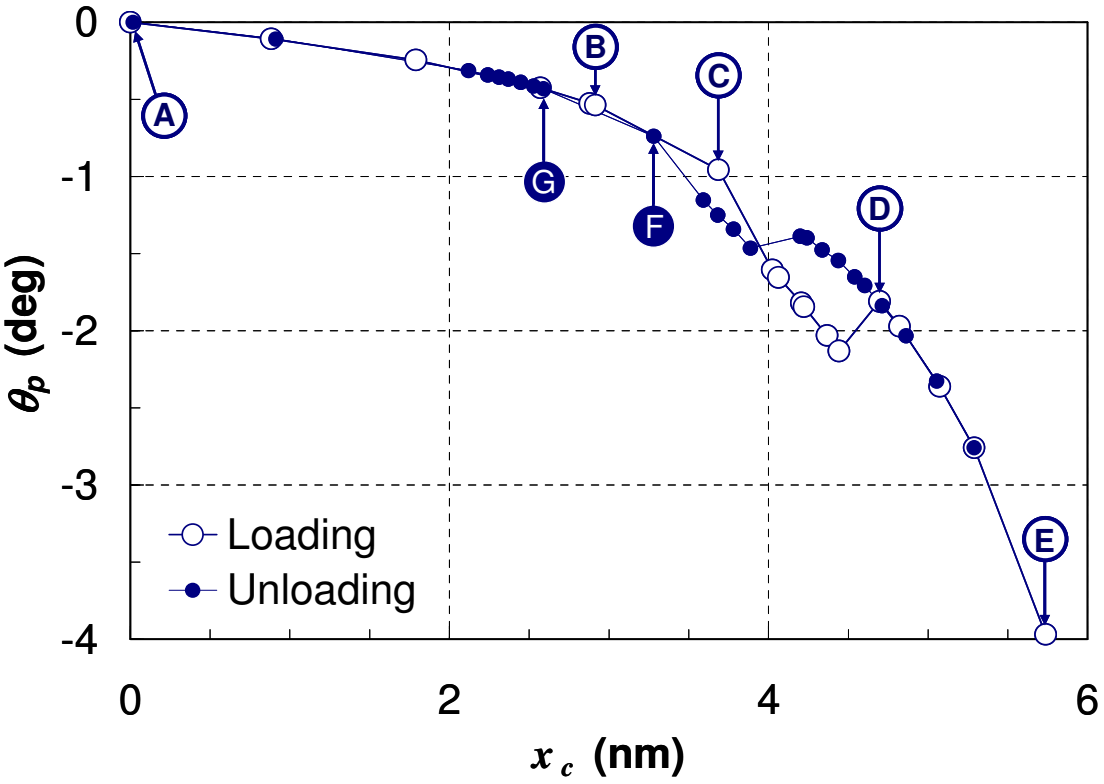

Figure 4.7: Parasitic rotation of the coupler bar.

4.2.2 Simulated Elastomechanics

It is also important to look not only at the kinematic response of the nPGM but also the force-displacement relationship of the mechanism. Figure 4.8 shows a plot of the total applied load, F, which is a sum of the two horizontal applied loads on the coupler bar, as a function of the horizontal coupler bar centroid translation. The force-displacement response data is located in Appendix B. Immediately one sees that the force required to actuate the nPGM to its maximum stroke is less than 10 nN. This force is on the same order of magnitude of the forces found to bend CNTs in [20]. The unshaded circles again represent the path of the coupler bar centroid as the load is incrementally increased. From point A to point B, which represents region I behavior, the nPGM acts like a linear spring with a spring constant of 1.23 nN/nm. The maximum error in region I due to this approximation is 3.9% at x_c = 1.79 nm. When the load is incrementally increased from point B the coupler bar snaps through (as indicated by the dotted line) to point C. The snap through is brought on by the development of kinks 1 and 2 in the nPGM. MM simulations cannot tell us if these kinks develop at the same time or separately.

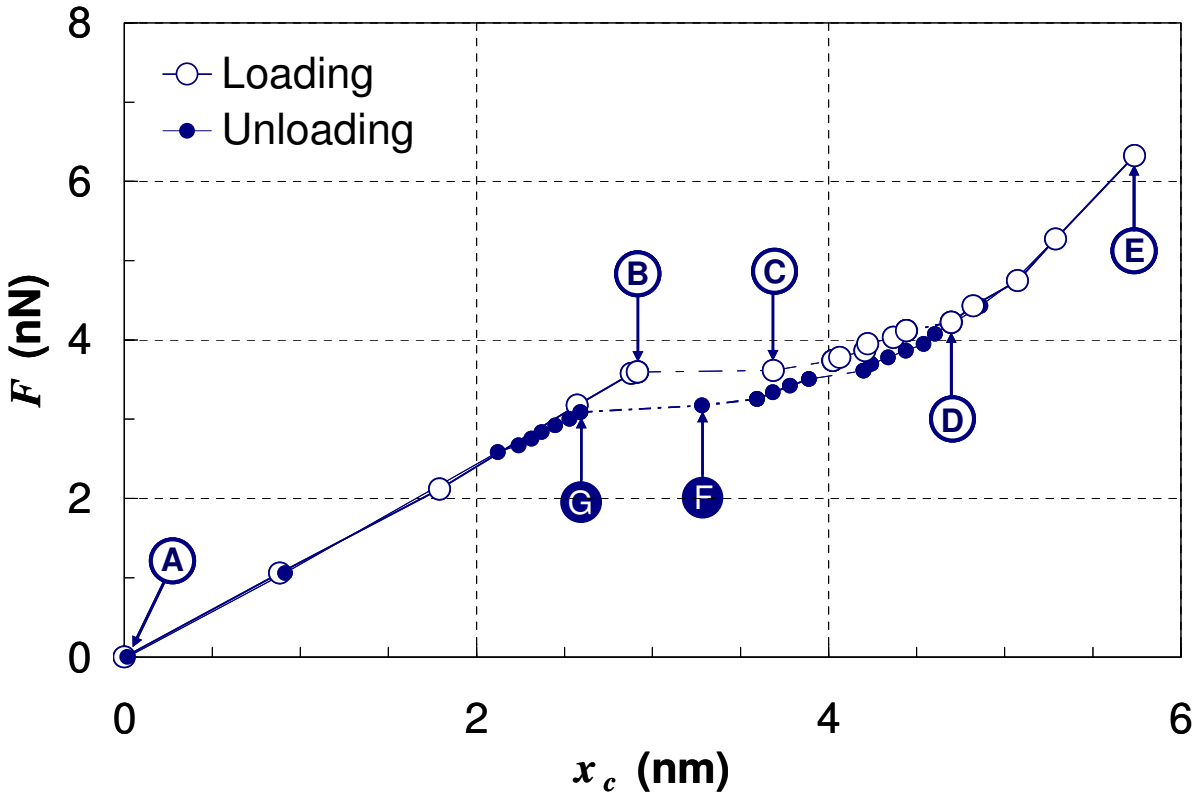

Figure 4.8: Force-displacement response of the coupler bar.

At x_c = 4.02 nm the nPGM develops a third kink and the coupler bar experiences another snap through. A final snap through occurs when the device reaches point D, where the nPGM possesses four kinks and has just entered region II behavior. After point D the device possesses a nonlinear and increasing stiffness. At point E the stiffness value is 2.34 nN/nm, which is almost double the stiffness of region I. One possible explanation for this increase in stiffness is attributed to geometric nonlinearity. For small displacements almost all of the horizontal load goes into bending deformations of the nPGM while at large horizontal displacements the horizontal load has a significant force component that places the SWCNTs in axial tension. Thus the stiffness at point E is a combination of the bending stiffness and tensile stiffness of the buckled SWCNT.

The shaded circles represent the path of the coupler bar centroid as the device is incrementally unloaded. While these paths appear identical from point D to E, the mechanism enters the transition region at a 14.5% lower loading level, 3.61 nN, than during the loading simulations. The coupler centroid transitions from three kinks to two at x_c =3.59 nm, which occurs at a loading level of 3.26 nN, 12.9% less than that required during the incremental loading

simulations. The flexure enters region I behavior when the coupler bar centroid snaps through from point F to point G. Once in region I, the mechanism again acts like a spring with a linear stiffness coefficient of 1.19 nN/nm, which is 3.2% lower than the value found in the loading simulations. This difference in stiffness coefficient should be attributed to experimental error in the simulations, not plastic deformation of the SWCNTs.

The results of these simulations again indicate that the behavior of the SWCNT-based nPGM is direction-dependant. While Yakobson, Brabec, and Bernholc speculated about the existence of this type of behavior [55], the published literature has yet to provide an adequate explanation for it. Before one may answer this question, however, the behavior of the transition region must be completely understood. We know that entering the transition region from region I or region II produces direction dependant behavior, but what happens if the device is incrementally loaded into the transition region and then incrementally unloaded before reaching region II? Figure 4.9 shows the results of such a MM study, while Appendix B contains the corresponding force and displacement data.

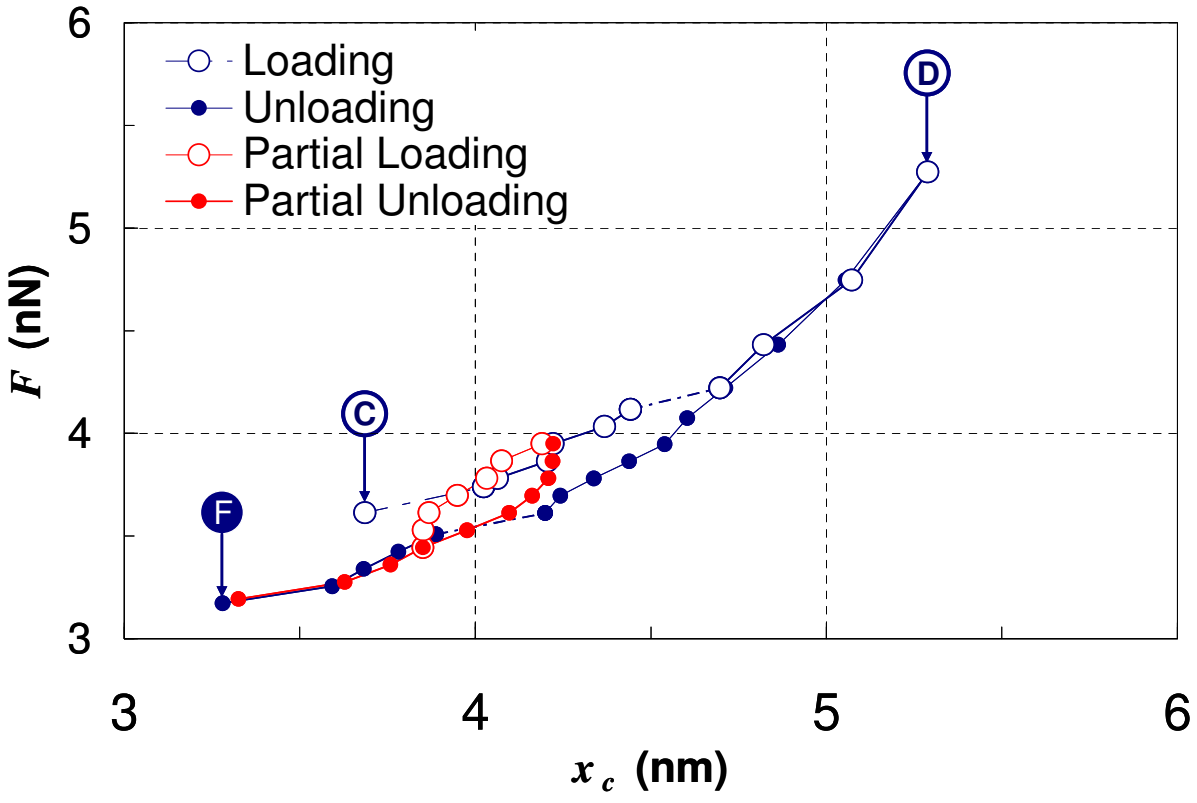

Figure 4.9: Loading/unloading response of the coupler bar in the transition region.

The dark unshaded circles show the path of the coupler bar centroid when the device is loaded incrementally from point C to point D. The dark shaded circles represent the centroid path if the mechanism is incrementally unloaded from point D to point F. In the simulation, the device began to be incrementally loaded from point C until the coupler bar reached a displacement x_c = 4.22 nm and a load of 3.95 nN. In this configuration the nPGM possessed three kinks. The device was then incrementally unloaded until it possessed only two kinks, as shown by the path traced out by the light shaded circles. At x_c = 3.85 nm (corresponding to a load of 3.53 nN) the nPGM was incrementally loaded again until the same load level was reached as at the start of the study, as shown by the path of the light unshaded circles. As the mechanism begins to be incrementally unloaded the coupler bar centroid first seems to "jump" from the loading curve to the unloading curve and then trace the unloading curve. Conversely, as the mechanism is loaded again the centroid seems to "jump" from the unloading curve to the loading curve before following the loading curve again. This is an interesting result because it means the kinematics and elastomechanics of the mechanism in the transition region are not "random" and it may be possible to find a relationship between the elastomechanic behavior of the mechanism and the type of loading/unloading it is experiencing in the transition region.

Since this type of direction-dependant behavior is not present in macro- or micro-scale CMs, one may postulate that its presence here may be attributed to a nano-scale physical phenomenon, the most unique of these being van der Waals forces. Figure 4.10 shows the results of a MM simulation in which the van der Waals interactions were turned off. The data for this simulation is located in Appendix B. The unshaded and shaded circles again represent the original loading and unloading data for the nPGM. The shaded squares represent the force-displacement data for a nPGM that is incrementally loaded without the presence of van der Waals forces. We see that the stiffness in region I is 1.13 nN/nm, which is 8.1% smaller than the value obtained in the loading simulations with van der Waals interactions present. Furthermore, the nPGM transitions from region I to region II occurs at a load of 3.30 nN and a displacement of 2.93 nm. This is a significantly lower loading level, but at a similar strain level, to that at point B, which has a load of 3.60 nN and displacement of 2.92 nm. There is no transition region in the no van der Waals interaction simulations, rather, the device immediately develops four kinks, causing the coupler bar centroid to snap through a distance of 2.85 nm.

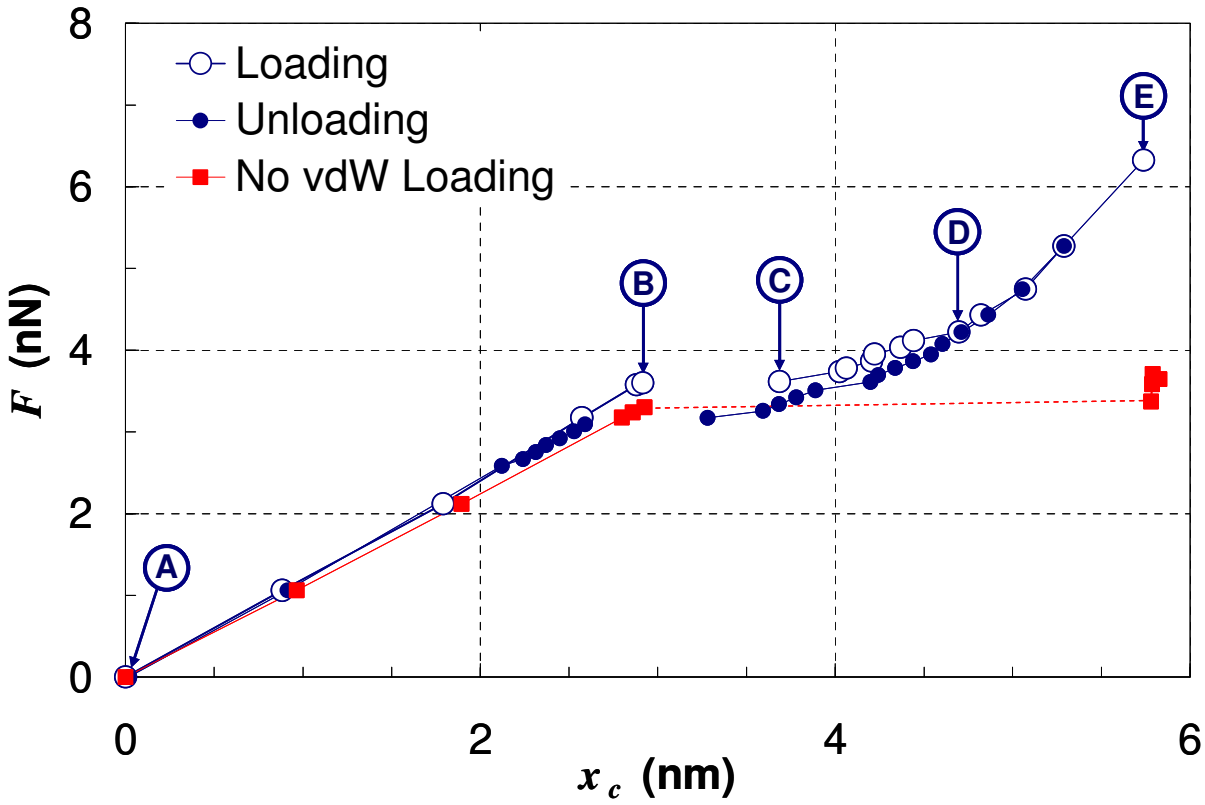

Figure 4.10: Force/displacement of the coupler bar with van der Waals interactions turned off.

Once the snap through occurs the flexure becomes stiff, approximately 23.4 nN/nm. The results of this study have two large implications: 1) that the van der Waals forces effectively stiffen the SWCNT, and 2) the formation of kinks may be associated with a specific strain level, not a particular load level.

4.2.3 Role of van der Waals Forces on Nano-scale Compliant Behavior

It is important to understand why the van der Waals interactions have such a profound impact on the kinematic and elastomechanic performance of the simulated nPGM. As mentioned in section 3.1.4, the equilibrium spacing for two non-bonded aromatic carbon atoms in the MM+ force field is 0.388 nm. This distance is 14.4% larger than the radius of the (5,5) SWCNT used in the simulations. Figure 4.11 shows an undeformed (located at point A), cross-section of the (5,5) SWCNT. The large shaded circles in the figure represent the zone of repulsion for a carbon atom. The radius of this zone of repulsion is 0.194 nm.

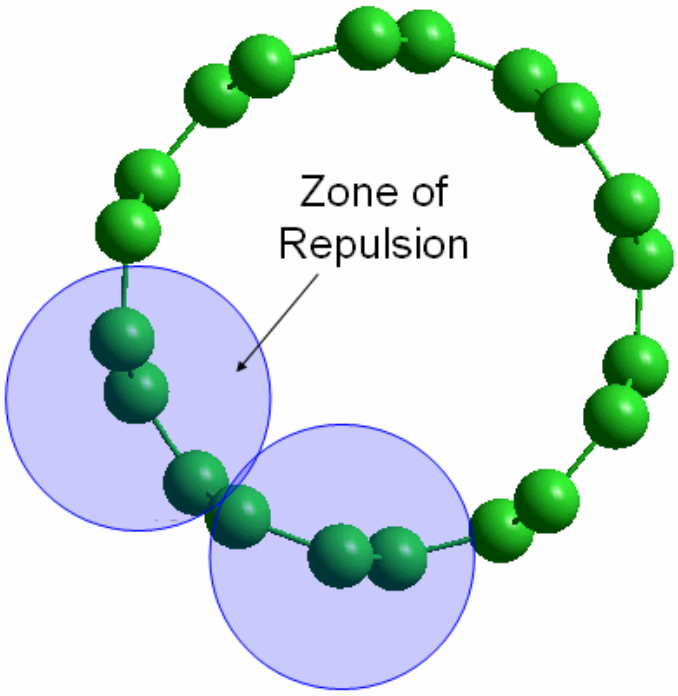

Figure 4.11: Van der Waals interactions in the non-bonded SWCNT cross-section.

If the zone of repulsion for one atom touches the zone of repulsion for another non-bonded atom, then the two atoms feel a repulsive force.

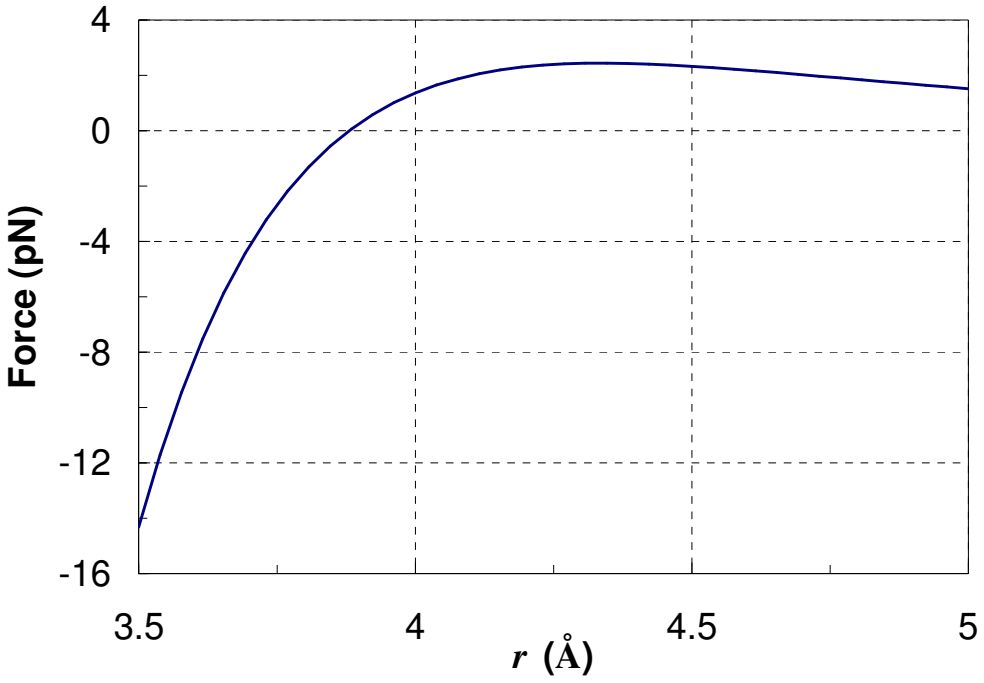

Figure 4.12: Van der Waals force as a function of atomic separation, r.

If the non-bonded atoms' zones of repulsions do not touch, then the atoms feel an attractive force. The magnitude of this force for atoms separated by a distance r is highly nonlinear, as shown in Fig 4.12. The maximum attractive force between carbon atoms is 2.44 pN at a separation distance of 4.3 Å. In contrast, a similar step size (0.4 Å) from the equilibrium position of the two non-bonded atoms in the repulsive region will produce a 29 pN repulsive force, more than an order of magnitude larger than in the attractive force case. It is clear from this analysis that repulsive forces quickly dominate attractive forces in the SWCNT.

As the nPGM is loaded, the cross-section of each SWCNT changes significantly in the areas where a kink forms. Figure 4.13(a) shows the progression of the cross-section deformation at the area where the first kink occurs, the lengths for each point of interest indicating the distance between the walls of the SWCNT along the dotted line. The outlines of the cross-sections indicate that during region I deformation the SWCNT tends to deform from a circle to an oval in the area of the kink, while from point C onward the cross-section assumes a crescent shaped profile. Figure 4.13(b) imposes the zones of repulsion on the resulting cross-section of kink 1 at point C. We find that the corners of the cross-section feel a strong repulsive force from those atoms at the top and bottom of the flattened cross-section.

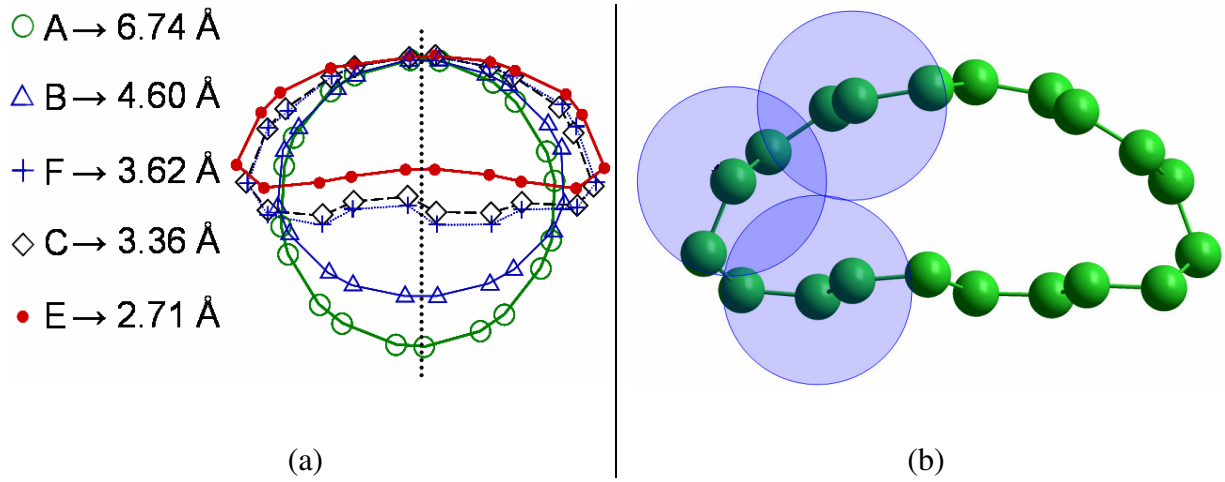

(a) (b)

Figure 4.13: Cross-section deformation during simulation (a)*, and van der Waals interactions for the kinked structure* (b).

Adding up the interactions of each atom in the cross-section of Fig. 4.13(b) one finds that there is a net repulsive force of 7.11 nN from the non-bonded interactions. As the CNT is subjected to higher loads, the cross-section becomes even more flattened, creating a larger net repulsive force as shown in Table 4.3.

Table 4.3: Net cross-sectional force for kink 1 at during loading/unloading of the nPGM.

Point	Net Repulsive Force (nN)
A	3.83
B	4.16
F	5.96
C	7.11
E	15.32

The presence of a net repulsive force at point A indicates that the tube is resisting cross-sectional deformation, which results in the effective stiffening of the tube. This is the reason that the MM simulations run in section 4.2.2 with no van der Waals interactions possessed a lower region I device stiffness.

The cross-sectional deformation really only occurs in the localized area around a kink. Figure 4.14 shows a longitudinal cross-section for each point of interest in the area around kink 1. We see that it takes only a few CNT unit cells in order for the cross-section to return to roughly its undeformed shape.

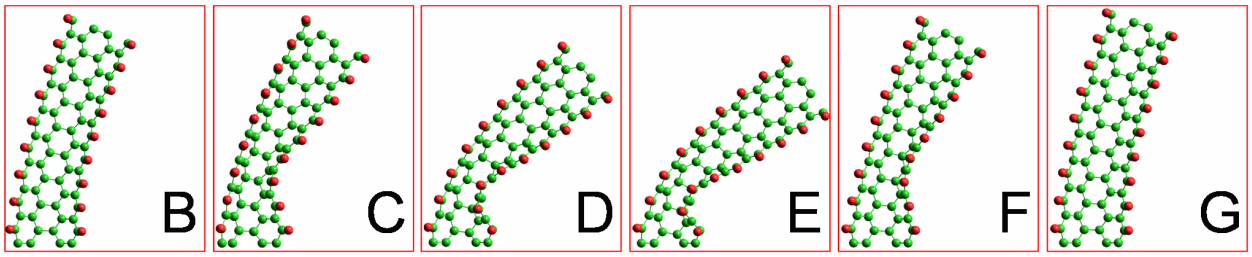

Figure 4.14: Longitudinal cross-sections of the first kink for points of interest.

In a SWCNT subject to no van der Waals interactions one expects that upon reaching the critical buckling point the cross-section of the CNT at the kink will completely collapse causing the front and back walls of the kink to contact one another. Pantano, Parks, and Boyce have documented this barbell type cross-sectional collapse of large diameter SWCNTs [60]. We find in the simulations run with van der Waals interactions that this collapse of the kink does not occur, and in fact, decreasing the distance between the front and back walls of the kink is difficult, as shown in the Fig. 4.14. The SWCNT would rather rotate about the kink than to collapse entirely; a phenomenon that is attributed entirely to the non-linear van der Waals force.

It is also important to consider the role of van der Waals forces in tubes of different diameter. For extremely small diameter tubes (0.3 nm [78]) the entire diameter of the tube is on

the order of the equilibrium van der Waals distance. This indicates that the tube would be difficult, if not impossible, to buckle, thereby letting a nPGM operate entirely in region I mode. If the SWCNT became too large in diameter (approximately 5 nm) than one would expect that the edges of the collapsed tube cross-section would have a large repulsive force while the flattened center of the tube would feel a large net attractive force, thereby keeping the kink intact even with no load applied and making the nPGM operate solely in region II after the initial buckling events had occurred. This result has been documented by Pantano, Parks, and Boyce [60].

4.2.4 Geometric Nonlinearity as a Cause for Direction-dependant Behavior

To this point a clear explanation for the direction-dependant behavior exhibited in the CNT-based nPGM MM simulations has not been given. As the load is reduced from point D, it is energetically preferential for the SWCNT to not revert back to its unkinked state, but to instead rotate about the kink. Due to the geometric nonlinearity that appears during SWCNT deformation, the unloaded SWCNT deforms by an entirely different mechanism than in the loading simulations. As the load is decreased and the tube rotates about the kink, the kink continues to widen. Eventually the elasticity in the curved walls of the CNT dominates and the SWCNT reverts back to its undeformed circular cross-section, which occurs during the transition from point F to point G. This direction-dependant phenomenon has been reported for axial tubes [25], but data has never been presented for a SWCNT in bending.

4.2.5 Energy-displacement Relationship

One may also gain insight into the performance of the nPGM by looking at the relationship between the strain energy, U_{strain}, in the model and the x-displacement of the coupler bar centroid, as shown in Fig. 4.15. We see that in region I behavior the strain energy appears to be parabolic, as predicted by the nearly linear spring constant found in section 4.2.3. The maximum strain energy in the system is 105 eV. This number is reasonable as the energy required to roll a graphene sheet into the SWCNT used in our simulation is approximately 18 eV, as calculated in Eq. 2.3.

Some may look at Fig. 4.8 and assume that the flexure has been subjected to hysteresis. If one compares the strain energy stored in the mechanism during the loading of the flexure to

the strain energy released during the unloading of the mechanism, one finds that they are within 2.7% of each other if the snap-through region is discounted. This is important as the MM simulations are conservative, therefore strain energy stored in the device as it is loaded to point E should be the same as the energy released as the load is removed from the device.

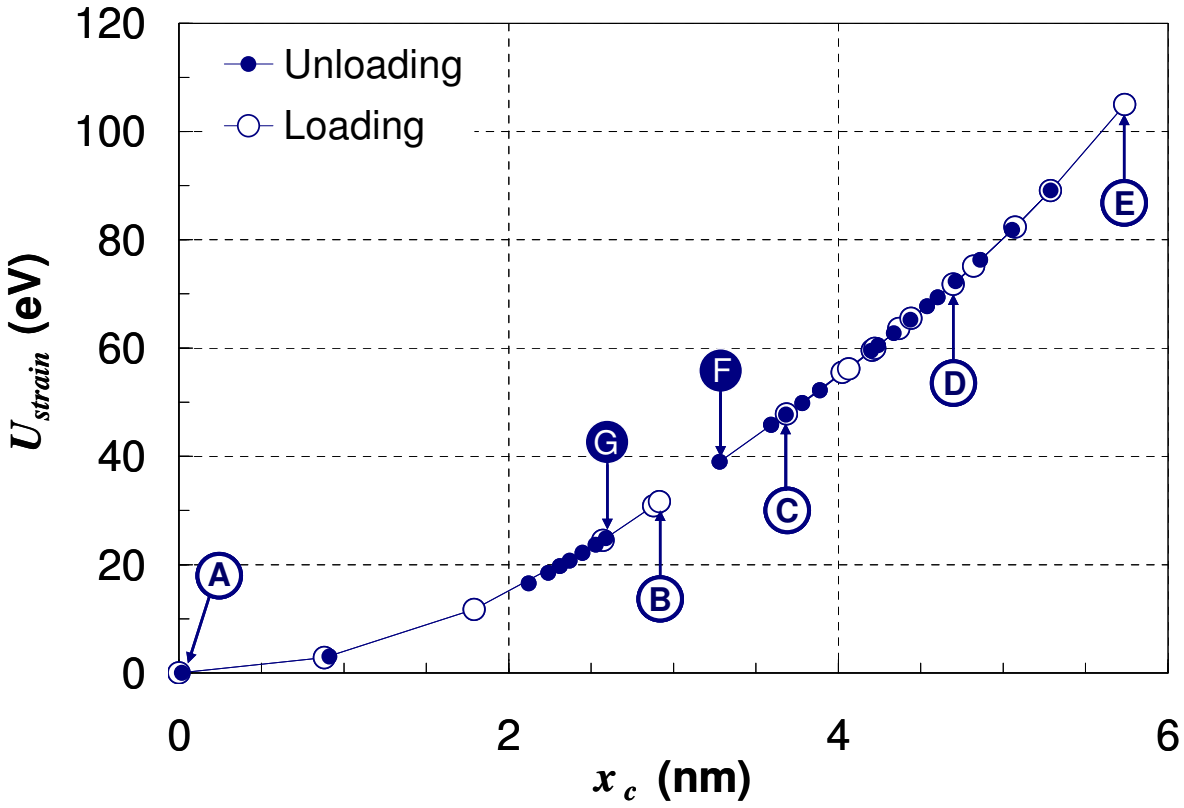

Figure 4.15: Strain energy in the nPGM as a function of horizontal centroid motion.

From the MM simulations it is not appropriate to say that energy is conserved in the system as there is no data present in the snap-through regions. The reason for this lack of data is that the MM simulations are unable to minimize a system that is at an unstable equilibrium, as in the case of a buckling event, because when the MM simulation imparts a displacement pattern on the atoms during an iteration cycle, the system will tend to prematurely jump to the buckled geometry. In order to capture data in this snap-through region the system must be simulated via MD. Figure 4.16 shows the force-displacement results of the MD simulations for the nPGM overlaid onto the MM data points.

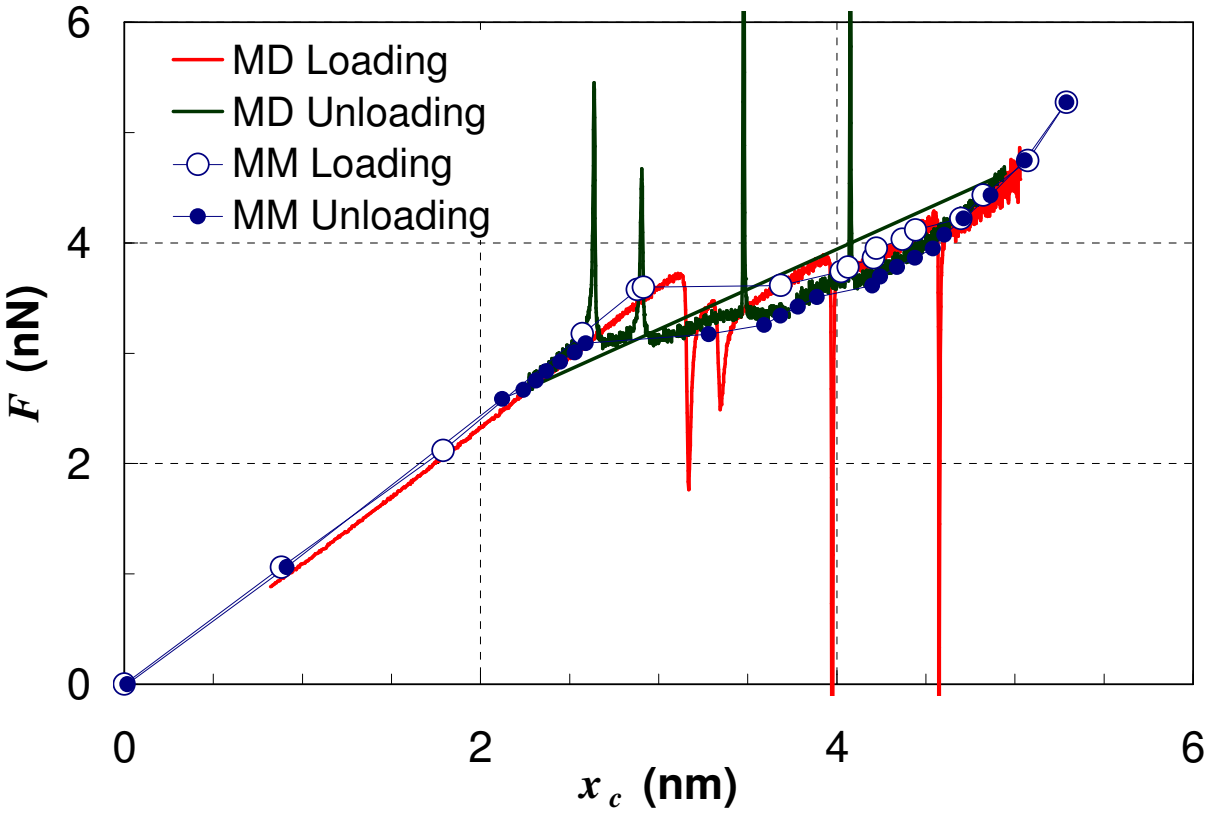

Figure 4.16: MM and MD force-displacement data for the nPGM.

The thick light colored line represents the force-displacement MD data for the nPGM as the load is increased. Note the presence of four sharp valleys in the data. Each of these valleys corresponds to the occurrence of a buckling event. The valleys exist because the system instantaneously loses stiffness when a kink forms thereby requiring less force to hold the system at that position. Thus the rest of the structure must compensate by achieving a different loaded geometry which increases the system stiffness and thereby requires a larger force to hold the system in that configuration.

In contrast the thick dark colored line corresponds to the unloading of the flexure. The data contains four sharp peaks, each indicating the reverting of a kink into a circular cross-section. The reason for the presence of each peak is exactly the opposite as the valley; when a cross-section becomes unkinked the device becomes instantaneously stiffer, thus requiring more force to hold the coupler bar at that position. The system then adjusts to the new system geometry and the load is decreased. Valleys therefore correspond to the storing of system strain energy in a kink, while peaks indicate the release of that same energy back into the structure.

The peaks and valleys provide a way for strain energy to be conserved in the nPGM because the strain energy in the nPGM may be represented by the area under the loading and unloading force-displacement curves. As a result the strain energy obtained by loading and unloading the nPGM is within 0.92%.

Chapter 5

Application of the Psuedo-Rigid-Body Model

The MM and MD simulations that were performed in Chapter 4 in order to characterize the kinematic and elastomechanic behavior of the CNT-based nPGM took almost two months to complete. The computation time required by MM and MD simulations makes both tools impractical as a method of simulating the mechanical response of a nCM because an engineer will routinely pursue multiple design concepts. Furthermore, once a concept is selected an engineer will also run several optimizations on the final design in order to achieve particular performance goals. If an engineer were to rely on MM and MD modeling to predict device performance it would translate into months of design time for devices that could be designed in days at the macro- and micro-scale. If macro-scale CM modeling techniques such as the PRBM could be applied to nano-scale devices it would translate into months of saved development time. This chapter will apply the macro-scale PRBM to the results presented in Chapter 4.

5.1 Psuedo-rigid-body Model Parameters

In order to apply Eq. 3.15, 3.16, and 3.20 to the nPGM model one first has to choose a few geometric and mechanical parameters. Perhaps the most important of the geometric parameters concerns the moment of inertia of the flexure, *I*. The cross-section of a CNT may be chosen as a solid rod or a pipe. As mentioned in section 2.2.1, Harik has set conditions via geometric similitude for modeling a SWCNT as a thin-walled shell, a thick-walled shell, or a solid rod. Table 5.1 shows a comparison of key geometric ratios in our system and the limits needed to model the SWCNT as a thick-walled cylinder as defined in [43].

Table 5.1: Criterion for modeling SWCNT as a hollow cylinder.

Parameter	Harik [43]	Current Model
$G_1 = \frac{L_{cnt}}{d_{cnt}}$	$G_1 > 10$	$G_1 = 11.3$
$G_2 = \frac{L_{cnt}}{a_{guc}}$	$G_2 > 10$	$G_2 = 31.1$
$G_3 = \frac{d_{cnt}}{a_{guc}}$	$24 > G_3 > 1.6$	$G_3 = 2.8$
$G_4 = \frac{d_{cnt}}{t_{cnt}}$	$20 > G_4 > 6$	$G_4 = 9$
$G_5 = \frac{d_{cnt}}{Et_{cnt}}$	$G_5 << 1$	$G_5 = 0.002$

Since the predominant mode of deformation in the nPGM is due to bending of the SWCNT, a value of $E \cdot t_{cnt}$ close to 360 nN/nm must be chosen (as shown in section 2.2.3). For the sections to follow the values obtained from [60], E = 4.84 TPa and t_{cnt} = 0.075 nm, will be assumed as they are in good agreement with other published studies. Table 5.2 lists the parameters for the initial PRBM simulations of the nPGM.

Table 5.2: Initial PRBM parameters for the nPGM.

γ	0.8517
K_θ	2.63 rad^{-1}
d_{cnt}	0.678 nm
t_{cnt}	0.075 nm
L_{cnt}	7.64 nm
E	4.84 TPa
I	0.0046 nm^4
γL_{cnt}	6.51 nm
K_{spring}	14.15 nN·nm/rad

5.2 Psuedo-rigid-body Model Predicted Kinematics

Using Eq. 3.15 and 3.16 the trajectory of the coupler bar centroid (with initial coordinates x_o = 3.82 nm and y_o = 7.64 nm) was predicting using the PRBM. Figure 5.1 shows the PRBM predicted trajectory as a solid line overlaid onto the MM simulated trajectory, shown as circles.

We see that using the traditional characteristic radius factor, γ, of 0.8517 allows the PRBM to accurately reproduce the trajectory of the coupler bar centroid. The maximum error in the prediction is 7.3% at x_c = 0.88 nm. It is important to note that the PRBM is still accurate in predicting the trajectory of the coupler bar centroid even with the presence of kinks in the transition region and region II. The maximum error is less than 3.5% past region I.

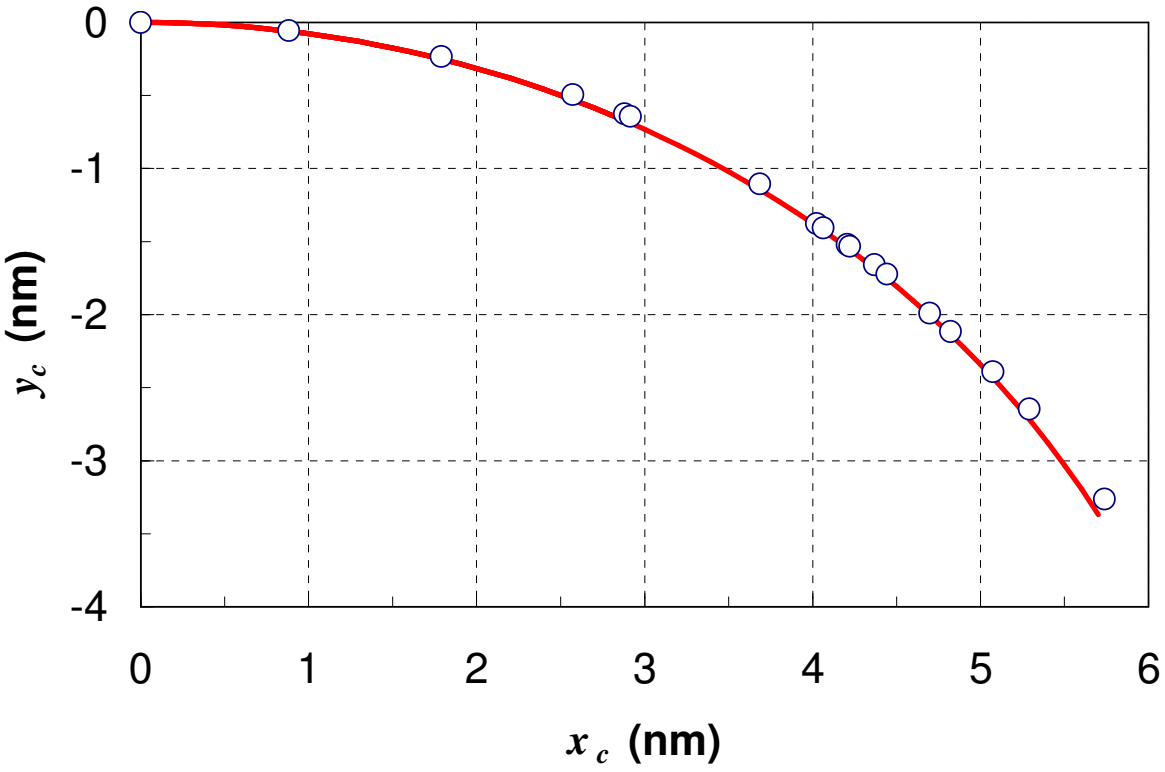

Figure 5.1: PRBM versus MM kinematics for the nPGM.

5.3 Psuedo-rigid-body Model Predicted Elastomechanics

The next step in evaluating the accuracy of the PRBM for predicting the behavior of the CNT-based nPGM is to apply Eq. 3.20 and predict the elastomechanic response of the system. Figure 5.2 shows the predicted PRBM response (solid line) overlaid onto the MM simulated loading data based on γ= 0.8517 and a stiffness coefficient, K_θ of 2.63 rad^{-1}.

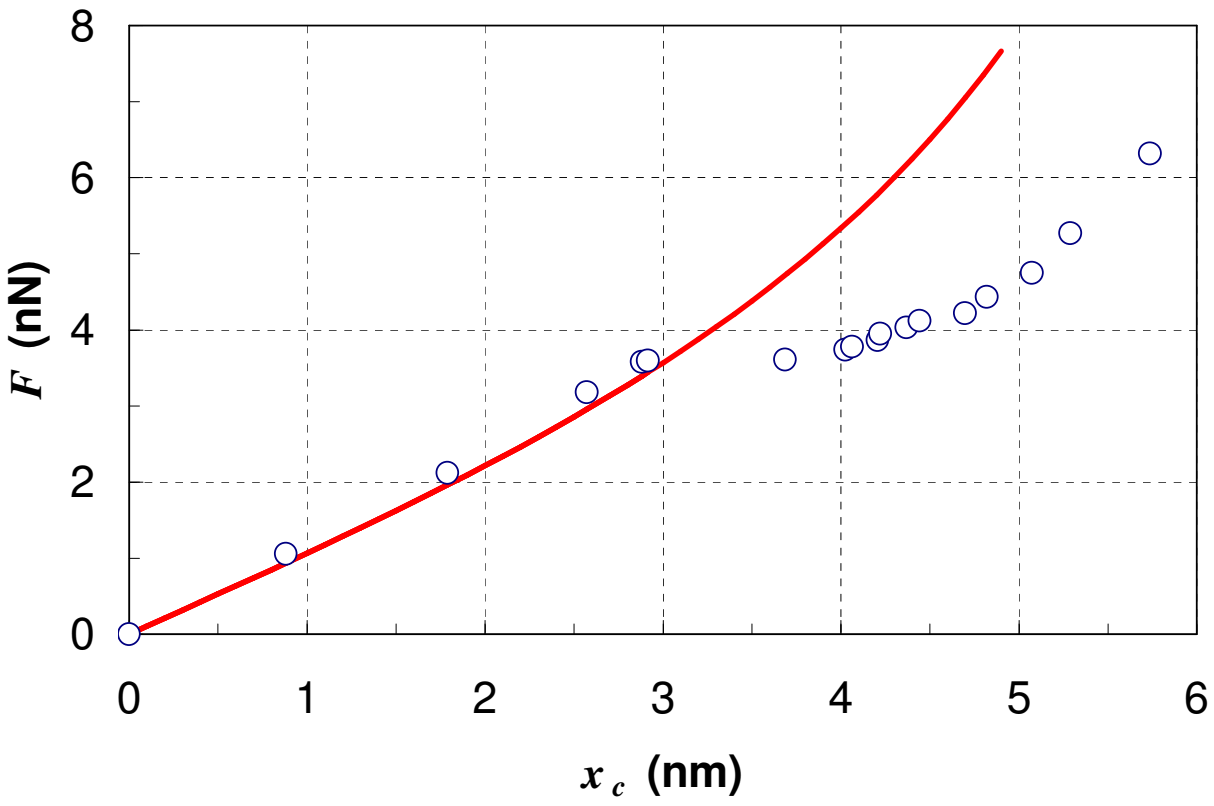

Figure 5.2: PRBM versus MM elastomechanics for the nPGM.

The PRBM elastomechanic response unfortunately does not replicate the MM results as the kinematic predictions did. In region I the PRBM loosely resembles the MM response curve, with a maximum force error of 15.4% at x_c = 0.25 nm. Past region I the two systems wildly diverge, with the PRBM grossly over-predicting the force required to actuate the system. It seems as if the PRBM will need to be defined in a piecewise manner in order to fully describe region I and region II behavior.

5.4 Improving the Psuedo-rigid-body Model Predictions

While the kinematic response of the nPGM was predicted to within 8% via the PRBM, the elastomechanics were poorly predicted. Redefining the PRBM in a piecewise manner for the nPGM is beyond the scope of this thesis; however, it may be possible to increase the accuracy of the PRBM in predicting region I behavior without augmenting the basic equations presented in Chapter 3. The following sections will focus on adjusting the characteristic radius factor as well as the stiffness coefficient in order to more accurately predict region I behavior of the CNT-

based nPGM. Note that while we could achieve this optimization by adjusting the rigidity value instead of the PRBM constants, one should be hesitant to arbitrarily change the rigidity because it is an experimentally determined value in the literature, as shown in Chapter 2.

5.4.1 Optimizing the Characteristic Radius Factor

As shown in section 3.2 the characteristic radius factor affects the elastomechanic and kinematic response of the system. Therefore it is imperative that when this parameter is adjusted that one looks at its affect on each response.

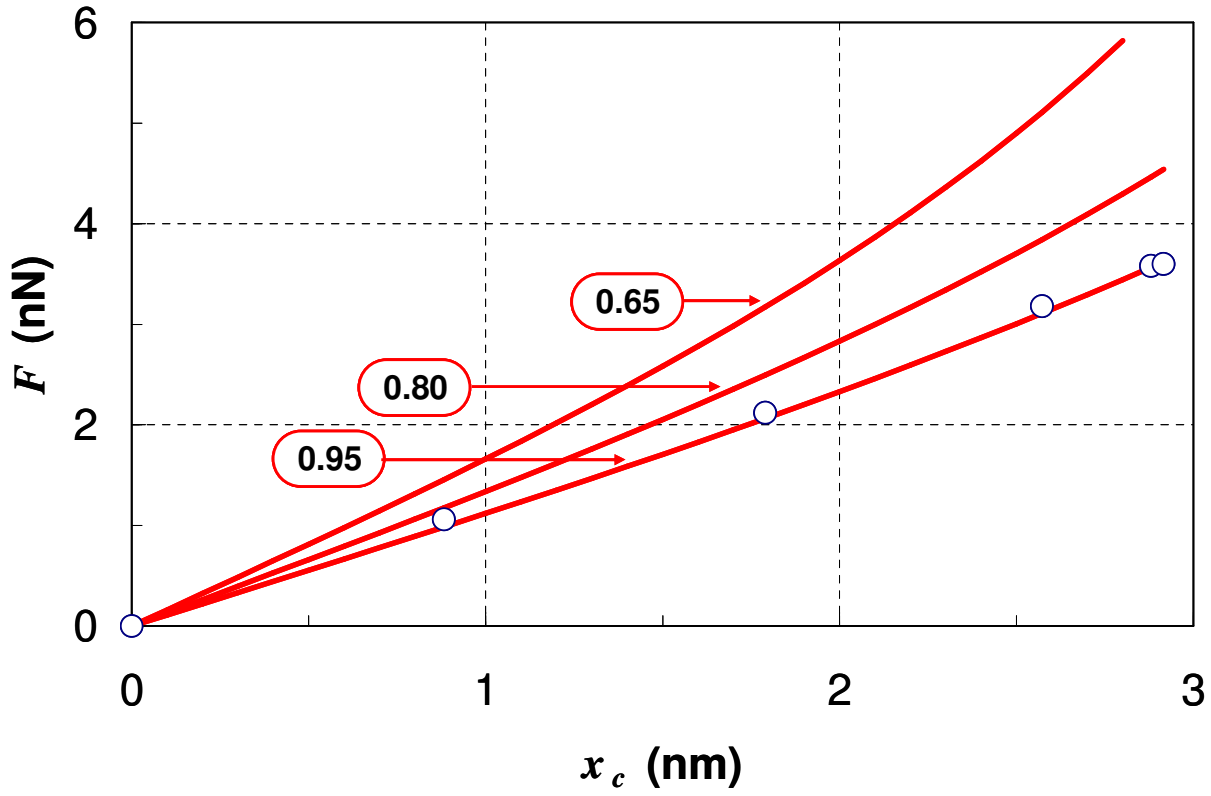

Figure 5.3: Affect of γ on PRBM predicted region I elastomechanics.

Figure 5.3 shows a plot of the region I MM elastomechanic data superimposed on a series of PRBM elastomechanic plots based on different values of γ. One sees that in order to improve the accuracy of the PRBM elastomechanics to less than 5% in region I one would have to increase the value of the characteristic radius factor to 0.94. Changing the value of the characteristic radius factor has an impact on the kinematic accuracy of the system, as shown in Figure 5.4.

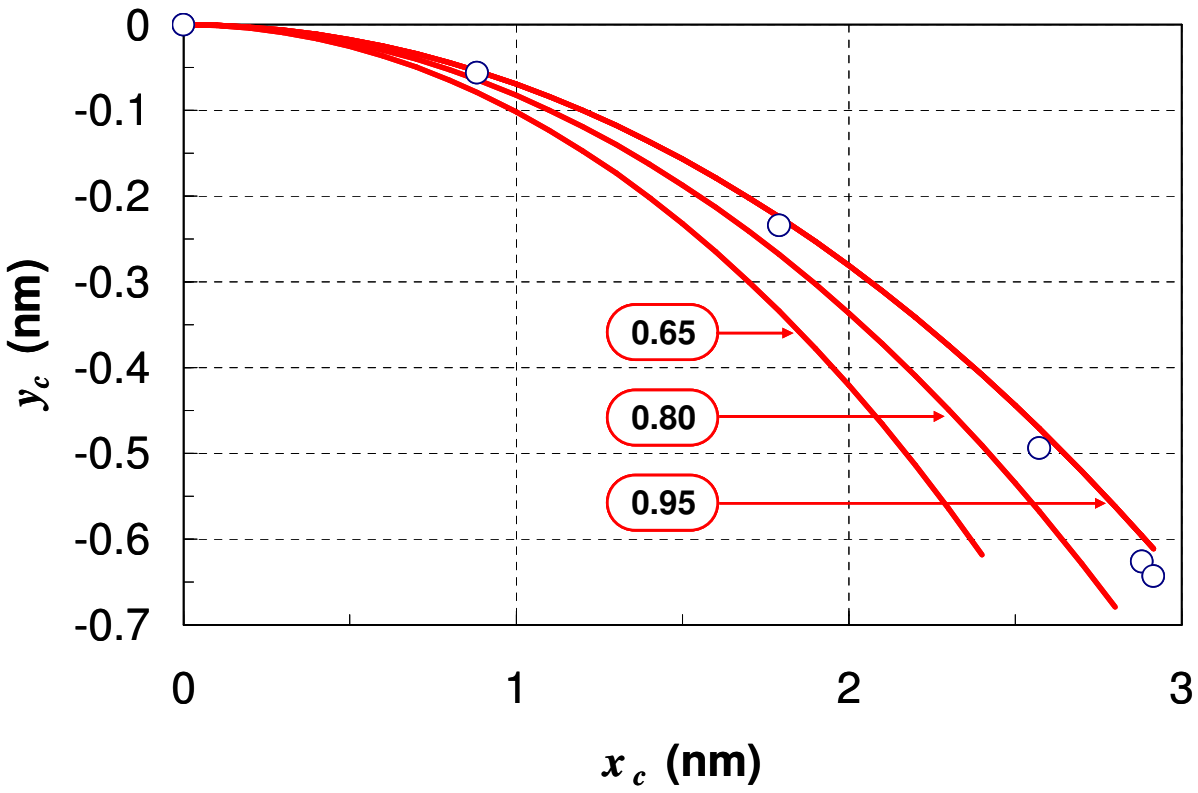

Figure 5.4: Affect of γ on PRBM predicted region I kinematics.

Using a value of 0.94 for γ produces an error of less than 4% in region I of the kinematic response. While we could change the characteristic radius factor to this new value, there is some benefit to leaving it unchanged. By leaving the characteristic radius factor unchanged, we leave the door open for future work involving optimizing the characteristic radius factor so as to capture the parasitic rotation of the coupler bar. The kinematics in region I are currently predicted to with less than 7.3% error, which is well within the accuracy required for evaluating different topologies and early stage optimization of a CM. It is with this future optimization in mind that we conclude that the characteristic radius factor should be left at 0.8517.

5.4.2 Optimizing the Stiffness Coefficient

With the $\gamma = 0.8517$ being set in section 5.4.1, it is now necessary to find the a value of K_θ that better predicts the elastomechanic response of the nPGM. Figure 5.5 shows a series of region I elastomechanic plots for $\gamma = 0.8517$ and different values of K_θ. A higher value of K_θ

leads to a higher value of K_{spring} and therefore larger actuating forces. We see that using a value of $K_\theta = 2.63$ under-predicts the actual force required to actuate the nPGM.

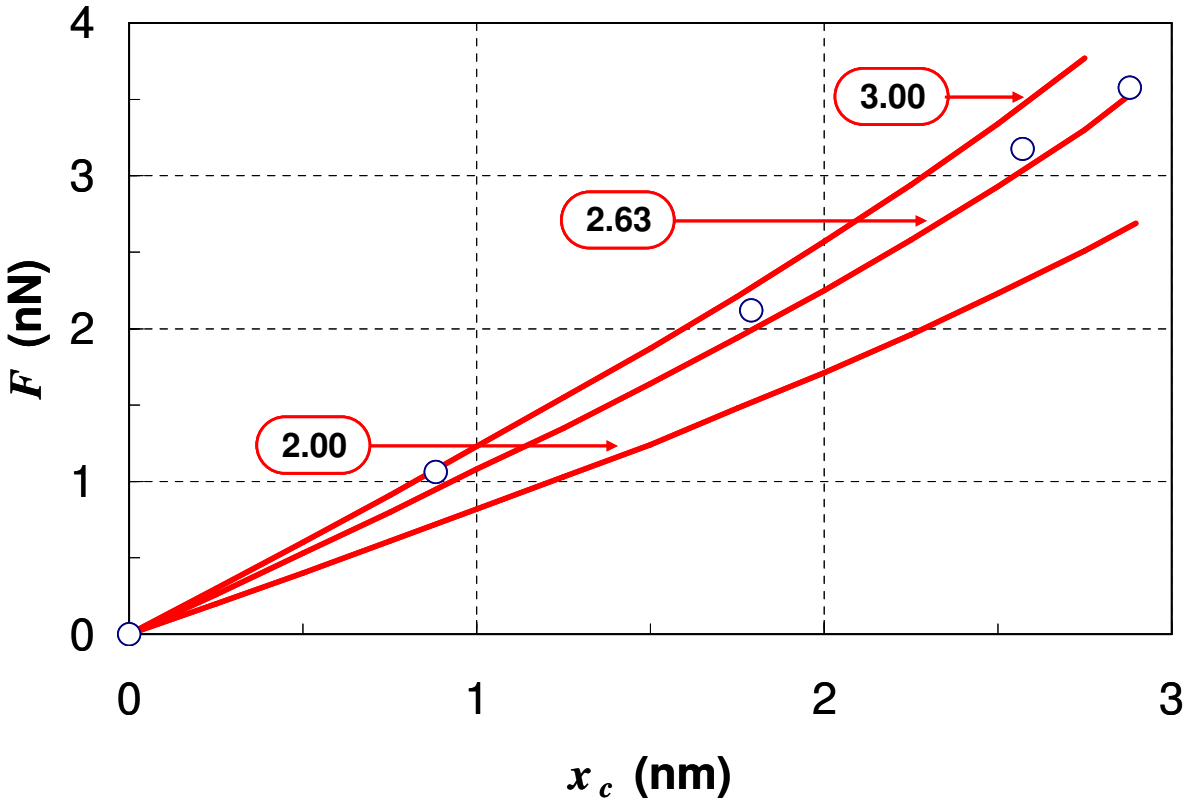

Figure 5.5: Affect of K_θ on PRBM predicted region I elastomechanics.

If we adjust K_θ to equal 2.85, the maximum error in the force prediction is 7.3 percent for $x_c = 0.5$ nm for a curve fit based on a linear spring constant of 1.23 nN/nm. The need for increasing the stiffness coefficient is attributed to the fact that van der Waals forces between the opposing interior surfaces of the tube that lead to a repulsive force that acts to prevent the bending deformation of the CNTs. This stiffening, about 8% of the device stiffness, matches the 8% increase in K_θ. We therefore recommend that the PRBM parameters of γ and K_θ be adjusted to 0.8517 and 2.85, respectively, for predicting region I behavior. The kinematic and elastomechanic data for the PRBM simulation utilizing the optimized coefficients is presented in Appendix D.

Chapter 6

Conclusion

The objective of this research is to generate the knowledge required to adapt macro- and micro-scale compliant mechanism theory to design carbon nanotube-based nano-scale compliant mechanisms. Carbon nanotube-based nano-scale compliant mechanisms are important because they may provide the means to produce nano-scale devices while avoiding (1) the size limitations imposed by current nano-fabrication techniques and (2) the performance limitations from traditional nano-scale materials. The realization of carbon nanotube-based devices would allow scientists and engineers to design smaller (100 times smaller than current micro-scale devices) and faster (over 1000 times faster than current micro-scale devices) compliant mechanisms for small-scale devices. CNTs are potential candidates for integration into nCMs because of (1) their size (on the order of nanometers), (2) their large-strain/deflection capability, and (3) their strength. It has been found that CNT-based nCMs are similar to macro-scale CMs in some regards and that adaptations of conventional CM modeling tools, such as the PRBM, may be used to accurately describe CNT-based nPGMs. This chapter will focus on summarizing the results of the research conducted in this thesis as well as presenting the fundamental issues that remain to be investigated.

6.1 Summary

The work presented in this thesis is a first step toward a better understanding of how to rapidly and accurately engineer CNT-based CMs for nano-electro-mechanical systems. The main observations of the work are as follows:

1. The kinematic behavior of CNT-based nPGMs appear to share some similarities with the kinematic behavior of macro-scale PGMs.

2. CNT-based nPGMs possess three regions of elastomechanic behavior due to the presence of buckling events, a behavior that is not observed in macro-scale PGMs.
3. Van der Waals forces are a significant force in the elastomechanic behavior of CNT-based nCMs.
4. There are three classes of CNT-based nCMs and each class is associated with a specific range of tube diameters.
5. The kinematic and elastomechanic behavior of a CNT-based nPGM are direction dependant.
6. In order to take advantage of the full operating range of a nPGM, the actuator should be displacement based in order to prevent device snap through that is caused by the buckling in the CNT flexural components.
7. The PRBM appears to be adequate for describing region I behavior but not region II behavior.
8. The stiffness coefficient for the PRBM must be increased to compensate for the effective van der Waals stiffening of the CNT.

The preceding observations will be summarized in greater detail in the remainder of this section.

The centroid of the coupler bar of the CNT-based nPGM follows an arcuate path that resembles that of a macro- or micro-scale PGM. The path appears continuous even in the presence of four separate buckling events within the SWCNTs that compose the flexural elements of the structure. A parasitic rotational error was present in the nPGM as predicted by Jones [76], a behavior that is not present in macro-scale PGMs. The first buckling event occurs when the structure has achieved 38.2% deformation (2.92 nm horizontal deflection). The device possessed elastic behavior even when subjected to strains of 75% (5.74 nm horizontal deflection). When a buckling event occurs the centroid snaps through to another position, creating a gap in the centroid trajectory. For continuous device operation the nPGM should be actuated with a displacement based actuator, not a force based actuator as we have presented. An alternative is to operate the device solely in region I, before the formation of any kinks in the structure.

The nPGM operates in three regions of behavior: 1) a region I where the device has no kinks, 2) a region II where the device possesses four kinks, and 3) a transition region that links region I and region II. In region I the device acts like as a linear spring that possesses a spring constant of 1.23 nN/nm. The device required 6.3 nN of force to strain the nPGM to 75% of the device width. In general, the elastomechanic behavior of the nPGM linear region is similar to that of macro-scale PGMs. The behavior within the transition region and region II, however, is unique to the CNT-based nPGM.

The forward and reverse loading of the device is identical in regions I and II, but not in the transition region. This direction dependant behavior, which is not found in macro-scale CMs, is caused by a combination of geometric nonlinearity, which is due to the geometry of the kinks, and van der Waals stiffening. Van der Waals interactions between the walls of the SWCNT increase the spring constant of the system by 8% in the particular case of a (5,5) SWCNT. This means there will be three classes of CNT-based nCMs based upon CNT diameter: 1) small diameter tubes (less than 0.5 nm) which do not buckle because of van der Waals stiffening, 2) large diameter tubes (greater than 5 nm) that remain buckled even after loading has been removed, and 3) intermediate tubes which buckle and still return elastically to their unloaded configuration.

The PRBM may predict the region I kinematics of the device to within 8%, which is acceptable for evaluating concepts and first pass optimizations of nCM topologies. The PRBM model does not capture the parasitic error rotations in the coupler bar in its current form; however, it could be easily adapted to do so in future work. The PRBM is capable of capturing region I behavior, but is not yet equipped to describe the transition region and region II behavior of the nPGM. By increasing the stiffness coefficient in the PRBM model by 8% to compensate for the van der Waals stiffening in the device, the error in the elastomechanic predictions for region I is less than 8%.

6.2 Future Work

The work described in the preceding is for a specific type of nCM and therefore should be viewed as the groundwork for a more comprehensive study on different types of CNT–based mechanisms. This is needed in order to develop a general understanding of how to characterize the performance of these devices as well as engineer these devices using the PRBM. Four items

should be further studied: 1) the affect of nCM topology on performance, 2) the affect of CNT properties on performance, 3) the affect of CNT bonding on device performance, and 4) adjusting the PRBM to take into account more complicated phenomenon such as the parasitic rotational error of the coupler bar.

Many other common CM building blocks exist: rotary guiding mechanisms, living hinges, etc. It is unknown how the kinematic and elastomechanic behavior of the nPGM studied in this work will relate to the behavior found in different topologies. The affect of vertical loading in the nPGM should also be investigated. If the nPGM is also vertically loaded while being horizontally actuated one could make estimates of the load capacity of the device in the different regions of operation and on the affect of "strain stiffening" as the tube is subjected to axial tension as the tube is actuated.

It will also be important to simulate the performance of the nCM in real world conditions. This includes simulating the device at room temperature and atmospheric pressure to ascertain the affect of thermal vibrations on the elastomechanic behavior of the device. Future work should also be conducted on simulating the dynamic response of the nPGM at different temperatures. This includes characterizing the frequency response of the system as well as quantifying the level of damping in the system.

There is also work to be done in investigating the affect of using different types of CNTs. The elastomechanic and kinematic behavior of the nCM may change with chirality, tube length, and the number of nested walls in the CNT. A complete study on the formation of defects in the CNTs must be carried out, with specific focus on how defects relate to the rate of load application to the nPGM. It will also be important to investigate how the presence of a defect in the CNT affects the performance of the nCM.

Another important aspect of the embodiment of a CNT-based nCM is the strength of the CNT to substrate bond. The final model of an nCM will need to incorporate many mechanical properties of this bond, including the stiffness of the interface as well as the maximum shear strength of the bond. The stiffness of the substrate should be incorporated into a model. The thermal response of the substrate, CNT, and CNT to substrate bond also should be investigated.

There are further modifications that need to be made to the PRBM. The model needs to be adjusted in order to allow the PRBM to predict the rotation of the coupler bar. Region II of the nPGM qualitatively resembles a modified version of the PRBM, but more work is needed to

quantify the accuracy of the match. It is unclear if the PRBM will be adequate in describing nCMs in which the device is being subjected to a tensile force in addition to the traditional bending force. Modifications to the rigidity value may have to be made to describe the "strain stiffening" affect that results from the combination of geometric nonlinearities and the nonlinear stiffness coefficient of a C-C bond in tension. Lastly, the direction dependant behavior of the transition region will need to be captured by the PRBM.

Finally, it is imperative that a CNT-based nCM be designed and fabricated in order to compare the simulated work with experimental results. Unfortunately there is work that needs to be accomplished before this realization. First and foremost a way of accurately growing, positioning, and bonding CNTs to a substrate must be found. It will also be important to research ways to actuate and sense these new types of machines.

References

[1] L.L. Howell. Compliant Mechanisms Wiley Interscience (2001).

[2] M. Hoummady, E. Farnault, H. Fujita, H. Kawakatsu, and T. Masuzawa. J. Vac. Sci. and Tech. B **15** (4), 1556 (1997).

[3] S. Iijima. Nature **354** (6348), 56 (1991).

[4] J. Lu and L. Zhang. Comp. Mat. Sci. **35** (4), 432 (2006).

[5] F. Ritort. J. Phys.: Condens. Matter **18**, R531 (2006).

[6] Y. Jiang, C. Juang, D. Keller, C. Bustamante, D. Beach, T. Houseal, and E. Builes. Nanotechnology **3** (1), 16 (1992).

[7] R.J. Fasching, S. Bai, T. Fabian, and F.B. Prinz. Microelectronic Eng. **83**, 1638 (2006).

[8] D.P. DiVincenzo. Science **270** (5234), 255 (1995).

[9] H. Choi and C.D. Montemagno. Nanotechnology **17** (9), 2198 (2006).

[10] X. Niu, L. Liu, W. Wen, and P. Sheng. App. Phys. Lett. **88** (15), 153508 (2006).

[11] M. Meyyappan, ed. Carbon Nanotubes: Science and Applications CRC Press (2005).

[12] S.C. Chen and M.L. Culpepper. Precision Eng. **30** (3), 314 (2006).

[13] K.E. Petersen. Proc. of the IEEE **70** (5), 420 (1982).

[14] J.D. Plummer, M.D. Deal, and P.B. Griffin. Silicon VLSI Technology: Fundamentals, Practice and Modeling Prentice Hall (2000).

[15] S. Chou, P. Krauss, and P. Renstrom. Science **272** (5258), 85 (1996).

[16] F. Hua, Y.G. Sun, A. Gaur, M.A. Meitl, L. Bilhaut, L. Rotkina, J.F. Wang, P. Geil, M. Shim, J.A. Rogers, and A. Shim. Nano. Lett. **4** (12), 2467 (2004).

[17] P. Kim and C. Lieber. Science **286** (5447), 2149 (1999).

[18] S. Akita and Y. Nakayama. Jap. J. of App. Phys. **41** (6B), 4242 (2002).

[19] J. Lee, S. Kim. Sensors and Actuators A **120**, 193 (2005).

[20] S.W. Lee, D.S. Lee, R.E. Morjan, S.H. Jhang, M. Sveningsson, O.A. Nerushev, Y.W. Park, and E.E.B. Campbell. Nano Lett. **4** (10), 2027 (2004).

[21] T. Rueckes, K. Kim, E. Joselevich, G.Y. Tseng, C. Cheung, and C.M. Lieber. Science **289** (5476), 94 (2000).

[22] J.E. Jang, S.N. Cha, Y. Choi, G.A.J. Amaratunga, D.J. Kang, D.G. Hasko, J.E. Jung, and J.M. Kim. App. Phys. Lett. **87**, 163114-1 (2005).

[23] J.C. Meyer, M. Paillet, and S. Roth. Science **309** (5740), 1539 (2005).

[24] S.J. Papadakis, A.R. Hall, P.A. Williams, L. Vicci, M.R. Falvo, R. Superfine, and S. Washburn. Phys. Rev. Lett. **93** (14), 146101–1 (2004).

[25] T. Chang, J. Hou, and X. Guo. App. Phys. Lett. **88**, 211906-1 (2006).

[26] B. Bourlon, D.C. Glattli, C. Miko, L. Forro, and A. Bachtold. Nano Lett. **4** (4), 709 (2004).

[27] S. Zhang, W.K. Liu, and R. Ruoff. Nano Lett. **4** (2), 293 (2004).

[28] W. Han, A.M. Fennimore, T.D. Yuzvinksly, M.S. Fuhrer, J. Cumings, and A. Zettl. Nature **424** (6947), 408 (2003).

[29] J. Cumings, and A. Zettl, Science **289** (5479), 602 (2000).

[30] R. Saito, R. Matsuo, T. Kimura, G. Dresselhaus, and M.S. Dresselhaus. Chem. Phys. Lett. **348** (3), 187 (2001).

[31] M. Yu, B.I. Yakobson, and R.S. Ruoff. J. of Phys. Chem. B **104** (37), 8764 (2000).

[32] W.C. Tang, T.C.H. Nguyen, and R.T. Howe. Sensors and Actuators A **20**, 25 (1989).

[33] R.S. Clay and J. Roy. Micro. Soc. **57**, 1 (1937).

[34] M.L. Culpepper, C.M. DiBiasio, R. Panas, S. Magelby, and L.L. Howell. App. Phys. Lett. **89** (20), 203111 (2006).

[35] C.M. DiBiasio, M.L. Culpepper, S. Magelby, L..L. Howell, and R. Panas. Submitted to J. Mech. Design (2006).

[36] R. Saito, G. Dresselhaus, and M.S. Dresselhaus. Physical Properties of Carbon Nanotubes Imperial College Press (2003).

[37] D.H. Robertson, D.W. Brenner, and J.W. Mintmire. Phys. Rev. B **45** (12), 12592 (1992).

[38] N.W. Winter and F.H. Ree. J. Computer-Aided Mat. Design **5** (2), 279 (1998).

[39] C. Li and T.W. Chou. Int. J. Sol. and Structures **40** (10), 2487 (2003).

[40] C.H. Kiang, M. Endo, P.M. Ajayan, G. Dresselhaus, and M.S. Dresselhaus. Phys. Rev. Lett. **81** (9), 1869 (1998).

[41] Q. Lu and B. Bhattacharya. Eng. Fracture Mech. **72**, 2037 (2005).

[42] M.B. Nardelli, B.I. Yakobson, and J. Bernholc. Phys. Rev. B **57** (8), R4277 (1998).

[43] V.M. Harik. Computational Mat. Sci. **24**, 328 (2002).

[44] N. Yao and V. Lordi. J. App. Phys. **84** (4), 1939 (1998).

[45] E. Hernandez, C. Goze, P. Bernier, and A. Rubio. Phys. Rev. Lett. **80** (20), 4502 (1998).

[46] A.L. Kalamkarov, A.V. Georgiades, S.K. Rokkam, V.P. Veedu, and M.N. Ghasemi-Nejhad. Int. J. Sol. and Structures **43** (22), 6832 (2006).

[47] K.N. Kudin, G.E..Scuseria, and B.I. Yakobson. Phys. Rev. B **64** (23), 235406 (2001).

[48] J.P. Lu. Phys. Rev. Lett. **79** (7), 1297 (1997).

[49] C.W.S. To. Finite Element Analysis and Design **42**, 404 (2006).

[50] D. Sanchez-Portal, E. Artacho, J.M. Soler, A. Rubio, and P. Ordejon. Phys. Rev. B **59** (19), 12678 (1999).

[51] K. Asaka and T. Kizuka. Phys. Rev. B **72** (11), 115431 (2005).

[52] M.F. Yu, B.S. Files, S. Arepalli, and R.S. Ruoff. Phys. Rev. Lett. **84** (24), 5552 (2000).

[53] M.F. Yu, O. Lourie, M.J. Dyer, K. Moloni, T.F. Kelly, and R.S. Ruoff. Science **287** (5453), 637 (2000).

[54] T. Dumitrica, T. Belytscko, and B.I. Yakobson. J. Chem. Phys. **118** (21), 9485 (2003).

[55] B.I. Yakobson, C.J. Brabec, and J. Bernholc. Phys. Rev. Lett. **76** (14), 2511 (1996).

[56] O. Lourie and H.D. Wagner. J. Mat. Res. **13** (9), 2418 (1998).

[57] K.M. Liew, C.H. Wong, X.Q. He, M.J. Tan, and S.A. Meguid. Phys. Rev. B **69** (11), 115429 (2004).

[58] X. Zhou, J.J, Zhou, and Z.C. Ou-Yang. Phys. Rev. B **62** (20), 13692 (2000).

[59] Z. Tu and Z.C. Ou-Yang. Phys. Rev. B **65** (23), 233407 (2002).

[60] A. Pantano, D.M. Parks, and M.C. Boyce. J. Mech. and Phys. Sol. **52** (4), 789 (2004).

[61] T.W. Tombler, C. Zhou, J. Alexseyev, J. Kong, H. Dai, L. Liu, C.S. Jayanthi, M. Tang, and S.Y. Wu. Nature **405** (6788), 769 (2000).

[62] Z.L. Wang, R.P. Gao, P. Poncharal, W.A. de Heer, Z.R. Dai, and Z.W. Pan. Mat. Sci. and Eng. C **16**, 3 (2001).

[63] A. Krishnan, E. Dujardin, T.W. Ebbesen, P.N. Yianilos, and M.M.J. Treacy. Phys. Rev. B **58** (20), 14013 (1998).

[64] J.P. Salvetat, G.A.D. Briggs, J.M. Bonard, R.R. Bacsa, A.J. Kulik, T. Stockli, N.A.

Burnham, and L. Forro. Phys. Rev. Lett. **82** (5), 944 (1999).

[65] K. Enomoto, S. Kitakata, T. Yasuhara, N. Ohtake, T. Kusumaki, and Y. Mitsuda. App. Phys. Lett 88 (15), 153115 (2006).

[66] S. Iijima, C. Brabec, A. Maiti, and J. Bernholc. J. Chem. Phys. **104** (5), 2089 (1996).

[67] Z.L. Wang, R.P. Gao, P. Poncharal, W.A. de Heer, Z.R. Dai, and Z.W. Pan. Mat. Sci. and Eng. C **16**, 3 (2001).

[68] P. Poncharal, Z.L. Wang, D. Ugarte, W.A. de Heer. Science **283** (5407), 1513 (1999).

[69] T. Chang, J. Geng, and X. Guo. App. Phys. Lett. **87** (25), 251929 (2005).

[70] H. Mori, Y. Hirai, S. Ogata, S. Akita, and Y. Nakayama. Jap. J. App. Phys. **44** (42), L1307 (2005).

[71] N.L. Allinger. J. Am. Chem. Soc. **99**, 8127 (1977).

[72] J. Lii, S. Gallion, C. Bender, H. Wikstrom, N.L. Allinger, K.M. Flurchick, and M.M. Teeter. J. Comp. Chem. **10**, 503 (1989).

[73] J.M. Derderian, L.L. Howell, M.D. Murphy, S.M. Lyon, and S.D. Pack. Proceedings of the 1996 ASME Mechanism Conference 96-DETC/Mech 1208 (2006).

[74] S. Reich, C. Thomson, and J. Maultzsch. Carbon Nanotubes: Basic Concepts and Physical Properties Wiley-VCH (2006).

[75] X. Chen and G. Cao. Nanotechnology **17** (4), 1004 (2006).

[76] R.V. Jones. Instruments and Experiences Wiley Interscience (1988).

[77] A.H. Slocum. Precision Machine Design Society of Manufacturing Engineers (1992).

[78] X. Zhao, Y. Liu, S. Inoue, T. Suzuki, R.O. Jones, and Y. Ando. Phys. Rev. Lett. **92** (12), 122502 (2004).

Appendix A: nPGM Kinematic Data

Table A1 contains the coordinates of the centroid of the coupler bar during the loading and unloading of the nPGM in the MM simulations. Note that these centroid coordinates are measured relative to the starting location of the coupler bar centroid (3.82 nm, 7.64 nm). Table A2 lists the parasitic rotation, θ_p, of the coupler bar for each x_c location of the coupler bar in the MM simulation.

Table A1: Coordinates of the coupler bar centroid during MM simulation.

Loading Data		Unloading Data	
x_c (nm)	y_c (nm)	x_c (nm)	y_c (nm)
0.00	0.00	0.02	0.00
0.88	-0.06	0.91	-0.06
1.79	-0.23	2.12	-0.33
2.57	-0.49	2.24	-0.37
2.88	-0.63	2.31	-0.40
2.92	-0.64	2.37	-0.42
3.69	-1.11	2.45	-0.45
4.02	-1.38	2.53	-0.48
4.06	-1.41	2.59	-0.50
4.21	-1.52	3.28	-0.86
4.22	-1.53	3.59	-1.07
4.37	-1.66	3.68	-1.13
4.44	-1.72	3.78	-1.20
4.70	-1.99	3.89	-1.28
4.82	-2.12	4.20	-1.54
5.07	-2.39	4.24	-1.57
5.29	-2.65	4.34	-1.66
5.74	-3.26	4.44	-1.75
-	-	4.54	-1.84

-	-	4.60	-1.90
-	-	4.71	-2.01
-	-	4.86	-2.16
-	-	5.06	-2.37
-	-	5.29	-2.65

Table A2: Rotation of the coupler bar centroid during MM simulation.

Loading Data		Unloading Data	
x_c (nm)	θ_p (deg)	x_c (nm)	θ_p (deg)
0.00	0.00	0.02	-0.00
0.88	-0.11	0.91	-0.11
1.79	-0.25	2.12	-0.32
2.57	-0.43	2.24	-0.34
2.88	-0.53	2.31	-0.36
2.92	-0.54	2.37	-0.37
3.69	-0.96	2.45	-0.39
4.02	-1.61	2.53	-0.42
4.06	-1.63	2.59	-0.43
4.21	-1.82	3.28	-0.74
4.22	-1.84	3.59	-1.15
4.37	-2.03	3.68	-1.25
4.44	-2.13	3.78	-1.34
4.70	-1.81	3.89	-1.47
4.82	-1.97	4.20	-1.39
5.07	-2.36	4.24	-1.40
5.29	-2.76	4.34	-1.48
5.74	-3.97	4.44	-1.55
-	-	4.54	-1.65
-	-	4.60	-1.71
-	-	4.71	-1.84

-	-	4.86	-2.03
-	-	5.06	-2.33
-	-	5.29	-2.76

Appendix B: nPGM Elastomechanic Data

Table B1 contains the horizontal coordinates of the centroid of the coupler bar during the loading and unloading of the nPGM as well as the total applied load to the coupler bar during the MM simulations. Note that these horizontal coordinates are measured relative to the starting location of the coupler bar centroid (3.82 nm). Table B2 contains the loading and centroid displacement data for the MM simulations of the nPGM run without the presence of van der Waals interactions.

Table B1: Horizontal load and displacement of the coupler bar during MM simulation.

Loading Data		Unloading Data	
x_c (nm)	F (nN)	x_c (nm)	F (nN)
0.00	0.00	0.02	0.00
0.88	1.06	0.91	1.06
1.79	2.12	2.12	2.58
2.57	3.18	2.24	2.67
2.88	3.58	2.31	2.75
2.92	3.60	2.37	2.84
3.69	3.61	2.45	2.92
4.02	3.74	2.53	3.01
4.06	3.78	2.59	3.09
4.21	3.87	3.28	3.17
4.22	3.95	3.59	3.26
4.37	4.03	3.68	3.34
4.44	4.12	3.78	3.42
4.70	4.22	3.89	3.51
4.82	4.43	4.20	3.61
5.07	4.75	4.24	3.70
5.29	5.27	4.34	3.78
5.74	6.32	4.44	3.86
-	-	4.54	3.95

-	-	4.60	4.07
-	-	4.71	4.22
-	-	4.86	4.43
-	-	5.06	4.75
-	-	5.29	5.27

Table B2: Force/displacement data for the no van der Waals interaction MM simulation.

x_c (nm)	y_c (nm)	θ_p (deg)	F (nN)
0.00	0.00	0.00	0.00
0.97	-0.09	-0.12	1.06
1.89	-0.29	-0.27	2.12
2.80	-0.62	-0.50	3.17
2.86	-0.64	-0.52	3.24
2.93	-0.68	-0.54	3.30
5.78	-3.89	-6.53	3.37
5.79	-3.87	-6.20	3.58
5.83	-3.95	-6.51	3.65
5.98	-4.32	-8.03	3.77

Appendix C: nPGM Strain Energy Data

Table C1 contains the horizontal coordinates of the centroid of the coupler bar during the loading and unloading of the MM simulations of the nPGM as well as the strain energy in the structure as a result of the applied load. Note that these coordinates are measured relative to the starting location of the coupler bar centroid (3.82 nm). The strain energy is computed by subtracting the unloaded system base energy (3230.26 kcal) from the minimized total system energy for the incremented load.

Table C1: Strain energy and displacement of the nPGM during MM simulation.

Loading Data		Unloading Data	
x_c (nm)	U_{strain} (eV)	x_c (nm)	U_{strain} (eV)
0.00	0.00	0.02	0.00
0.88	2.81	0.91	3.00
1.79	11.72	2.12	16.54
2.57	24.49	2.24	18.49
2.88	30.85	2.31	19.70
2.92	31.62	2.37	20.73
3.69	47.80	2.45	22.14
4.02	55.49	2.53	23.65
4.06	56.18	2.59	24.85
4.21	59.58	3.28	38.98
4.22	59.95	3.59	45.80
4.37	63.60	3.68	47.71
4.44	65.49	3.78	49.82
4.70	71.79	3.89	52.19
4.82	75.13	4.20	59.50
5.07	82.34	4.24	60.51
5.29	89.07	4.34	62.75
5.74	105.00	4.44	65.20
-	-	4.54	67.72

-	-	4.60	69.36
-	-	4.71	72.29
-	-	4.86	76.29
-	-	5.06	81.81
-	-	5.29	89.07

Appendix D: PRBM Data for the nPGM

Table D1 contains the translational coordinates of the centroid of the coupler bar during the PRBM loading of the nPGM as well as the force required to actuate the structure. The data is generated from an elastic modulus of 4.84 TPa, a moment of inertia of 0.0046 nm^4, a characteristic radius of 0.8517, and a stiffness coefficient of 2.85.

Table D1: PRBM kinematic and elastomechanic data

x_c (nm)	y_c (nm)	F (nN)
0.00	0	0
0.88	-0.06	1.02
1.79	-0.25	2.16
2.57	-0.53	3.29
2.88	-0.67	3.80
2.92	-0.69	3.86
3.69	-1.15	5.43
4.02	-1.39	6.31
4.06	-1.42	6.42
4.21	-1.54	6.85
4.22	-1.56	6.90
4.37	-1.68	7.38
4.44	-1.75	7.65
4.70	-2.00	8.67
4.82	-2.14	9.24
5.07	-2.43	10.62
5.29	-2.72	12.12
5.74	-3.44	17.01